

**Liquid-phase electron microscopy:  
toward direct imaging of self-assembly processes  
in low-atomic number colloidal suspensions**

Dissertation

zur Erlangung des Grades

des Doktors der Naturwissenschaften

der Naturwissenschaftlich-Technischen Fakultät

der Universität des Saarlandes

von

Peter Kunas

Saarbrücken

2021

Tag des Kolloquiums: 17.12.2020

Dekan: Prof. Dr. Jörn Walter

Berichterstatter: Prof. Dr. Dr. h.c. Niels de Jonge

Prof. Dr. Uwe Hartmann

Vorsitz: Prof. Dr. Tobias Kraus

Akad. Mitarbeiter: Dr. Thomas John

*" The essence of result is to be free of hope."*

-Jigmé Lingpa

## **Zusammenfassung**

Es ist von großem technologischem Interesse, die Organisation von Nanopartikeln (NPs) in funktionellen Anlagen zu steuern. In diesem Kontext besteht eine große wissenschaftliche Herausforderung darin, die Kräfte zwischen den Partikeln, die die spontanen Selbstorganisationsprozesse (S-A) in flüssigen Suspensionen steuern, weiter aufzuklären. Die Flüssigphasen-Elektronenmikroskopie (LPEM) kann morphologische Details kleiner Objekte in  $\mu\text{m}$ -dicken Flüssigkeitsschichten im nm-Bereich auflösen. Ziel dieser Doktorarbeit war es, LPEM weiter zu entwickeln, um kolloidale S-A in wässrigen Suspensionen direkt sichtbar zu machen. Als Modellsystem verwendeten wir ein kolloidales Binärsystem, in dem positiv geladene 30-nm-Nanopartikel (SiONP) eine Hülle um negativ geladene 100-nm-Polystyrol-Mikrokugeln (PMS) bilden. Analytische Berechnungen und Monte-Carlo-Simulationen wurden durchgeführt, um experimentelle Parameter zu optimieren und die Kontrastbildung in rastertransmissionselektronenmikroskopischen Aufnahmen zu validieren. Das Ausmaß der radiolytischen Schädigung der PMS durch den Elektronenstrahl wurde anhand der Bilddaten analysiert, und ein akzeptabler Dosisbereich wurde definiert. Innerhalb dieses Bereichs wurde die Core-Shell-Struktur des vormontierten Binärsystems direkt visualisiert. Abschließend wurde ein neuartiges Flüssigkeitszellendesign getestet, das es uns ermöglichte, kolloidale S-A in der geschlossenen, nanofluidischen Vorrichtung zu initiieren und visualisieren.

## Summary

It is of great technological interest to control the organization of nanoparticles (NPs) into functional devices that can make use of NP's properties not found in the bulk form of the solid material. To this end, a major scientific challenge is to further elucidate inter-particle forces that govern spontaneous self-assembly processes in liquid suspensions. Liquid-phase electron microscopy (LPEM) can resolve morphological details of small objects in  $\mu\text{m}$ -thick liquid layers with nanometer resolution. The goal of this doctoral thesis has been to develop LPEM towards directly visualizing colloidal self-assembly processes in aqueous suspensions. As a model system, we used a colloidal binary system in which positively charged 30 nm nanoparticles (SiONP) form a shell around 100 nm, negatively charged polystyrene microspheres (PMS). Analytical calculations and Monte-Carlo simulations were performed to optimize experimental parameters and to validate contrast in data obtained with a scanning transmission electron microscope (STEM). The extent of radiolytic damage due to the electron beam (PMS) was directly analyzed from the image data and an acceptable dose range was defined. Within this range, the core-shell structure of the pre-assembled binary system was directly visualized. Finally, a novel liquid cell design was tested which enabled us to initiate colloidal assembly reactions in the confinement of the nanofluidic device.

## **Acknowledgments**

First, I would like to express my gratitude to my supervisor, Professor Niels de Jonge. He offered me an opportunity to work in his group and has guided me through many challenges. In addition, he gave me the freedom and responsibility to find my own way around the problems that I encountered during my scientific work.

Secondly, a warm thank you to Dr. Sercan Keskin and Dr. Navina Dahmke. You guys have been the best colleagues I could have ever hoped for. Thank you also all present and former group members of the IEM, Dr. Elisa Cepeda, Tabea Trampert, Stefanie Smolka, Dr. Eduardo Ortega, Dr. Florian Weinberg, and Patricia Blach. Many thanks also to Dr. Andreas Verch and Jörg Schmauch for guiding me in the practicalities of electron microscopy.

I would certainly like to thank Prof. Nico Sommerdijk, Prof. Joseph Patterson, Dr. Heiner Friedrich, and Dr. Mohammad Moradi for involving me in their research through the MULTIMAT Marie Skłodowska-Curie Actions- Innovative Training Network. Warm thanks also to Dr. Hanglong Wu and Xiaobin Xie, Paula Vena, Deniz Eren, and Dr. Louis Valencia for shared experiments and many inspiring discussions we had during these four years of MULTIMAT. Thank you, Elizabeth McKenzie, for coordinating MULTIMAT and organizing events, workshops, and especially of that inspiring writing retreat in Lake District, UK. Thank you, Ben Bormans, Hugo Perez, Dr. Hongyu Sun, Tijn van Omme, Anne Beker, and Olaf Weller for the important experience I got while visiting DENSsolutions.

Thank you very much to my old colleagues at the University of Turku. Professors Carita Kvarnström and Jukka Lukkari, Dr. Pia Damlin, Dr. Jussi Kauppila, and Dr. Markus Peurla. Warm thanks also to Professor John Erikson and the Turku BiImaging-crew.

Finally, I would like to thank my friends and family for simply being there and sharing the daily joys and sorrows. My mother Katriina, Layla, Rippe and Laura, Miksu, Joana, and little Alma, Jani, Jori, Tibor, Nikke, Erkka, Violeta, Stephanie & Siri, Martin and Daniel, Ville and Mikko.

## Contents

Zusammenfassung .....	2
Summary .....	3
Acknowledgments .....	4
<b>Chapter 1. Introduction.....</b>	<b>9</b>
1.1 The scope of this thesis.....	9
1.2 Electron microscopy of structures and processes of soft matter .....	10
1.3 Instrumentation and sample preparation in LPEM .....	12
1.4 Microscope types.....	15
1.5 Electron scattering from the sample .....	17
1.6 Electron-optical limitations of the microscope .....	19
1.7 Theory of attainable resolution of and contrast of spherical nano-objects in LPEM.....	22
1.8 Attainable resolution for polystyrene, silica, and gold.....	27
1.9 Phase-contrast in LPEM and related systems.....	32
1.10 LPEM: Challenges, methods, and insights .....	38
1.11 Concluding remarks and the intended impact .....	47
1.12 A note about contributions .....	50
<b>Chapter 2. Methods .....</b>	<b>52</b>
2.1 Buffer and saline solutions .....	52
2.2 Colloidal dispersions .....	52
2.3 Monte-Carlo simulations .....	53
2.4 Numerically solved analytical calculations .....	53
2.5 Scanning transmission electron microscopy .....	54
2.6 Transmission electron microscopy .....	55

2.7 Scanning electron microscopy .....	55
2.8 Liquid-phase electron microscopy.....	55
2.9 Elemental analysis with EDX and EELS.....	56
2.10 Measurement of liquid thickness .....	57
2.11 Image analysis.....	57
2.12 Inductively coupled plasma atomic emission spectroscopy (ICP-AES).....	58
<b>Chapter 3. Optimization of STEM parameters <i>in silico</i>.....</b>	<b>61</b>
3.1 Introduction .....	61
3.1.1 Monte-Carlo simulations for STEM .....	61
3.1.2 Physical models used in the Casino-software .....	62
3.1.3 Determination of SNR in image data.....	63
3.2. Results.....	64
3.2.1 Measuring SNR from experimental and simulated image data .....	64
3.2.2 Signal-to-noise-ratio of multi-pixel objects.....	65
3.2.3 SNR and statistical estimation of the experimental resolution .....	68
3.2.4 Investigation of MC-simulated image data .....	69
3.2.5 Appearance of binary structures in LPEM.....	73
3.3 Discussion .....	78
3.4 Conclusions .....	79
<b>Chapter 4. Imaging colloidal assemblies in a liquid cell .....</b>	<b>81</b>
4.1 Introduction .....	81
4.1.1 Beam damage of polystyrene and Silica .....	82
4.1.2 Experimental considerations on optimizing the data acquisition.....	83
4.1.3 Validation of the contrast and post-mortem analysis .....	83

4.2 Results.....	84
4.2.1 Validation of simulated data .....	84
4.2.2 Study on the structural beam sensitivity of PMS .....	87
4.2.3 Imaging pre-formed binary structures .....	89
4.2.4 Comparison of TEM and STEM .....	91
4.2.5 Artifacts and cross-contamination .....	93
4.3 Discussion .....	95
4.4 Conclusions .....	99
<b>Chapter 5. Fresnel-contrast imaging in liquid.....</b>	<b>100</b>
5.1 Introduction .....	100
5.2 Results.....	101
5.2.1 Thinning the liquid layer.....	101
5.2.2 The effect of defocus on the appearance on SiONP-assemblies .....	102
5.2.3 The effect of the objective lens aperture on the appearance of SiONP .....	105
5.2.4 Putting Fresnel-fringes in work: Comparing Fresnel-contrast imaging with BF-STEM.....	107
5.3 Discussion .....	109
5.4 Conclusions .....	111
<b>Chapter 6. Improved cell design for imaging colloidal assembly in a liquid cell.....</b>	<b>112</b>
6.1 Introduction .....	112
6.2 Results.....	113
6.2.1 Colloidal assembly in bulk .....	113
6.2.2 Colloidal assembly in the confinement of a liquid cell.....	115
6.2.4 Why is colloidal assembly hindered in a liquid cell? .....	117

6.2.5 Improved chip design with a microchannel .....	119
6.2.6 Colloidal assembly in a “microchannel” liquid cell .....	121
6.2.7 Binary self-assembly in standard and “microchannel” liquid cell.....	123
6.3 Discussion .....	125
6.4 Conclusions .....	128
<b>Chapter 7. Conclusions and outlook .....</b>	<b>129</b>
7.1 The impact: general workflow for designing an LPEM experiment .....	131
7.2 Outlook .....	134
Bibliography.....	135
Publications.....	146
Oral communications and conferences.....	146
Invited lectures in conferences.....	146
Poster communications in conferences .....	147
Supplementary Information .....	147
<b>Appendix I: Determination of the electron dose .....</b>	<b>148</b>
<b>Appendix II: Measuring liquid thickness by using electron energy-loss spectroscopy ....</b>	<b>152</b>
<b>Appendix III: Image analysis script to measure the shrinking of PMS.....</b>	<b>160</b>

## Chapter 1. Introduction

*“Based on the theory and literature, what are the capabilities of electron microscopy for imaging structures and processes in liquid?”*

### 1.1 The scope of this thesis

The goal of this doctoral thesis is to study and further develop the methodology in liquid-phase electron microscopy (LPEM) to directly image low atomic number (low-Z) soft materials such as colloidal structures and their dynamics in liquid suspensions.

The studied model system consists of positively charged, amino-functionalized, 30 nm diameter, amorphous SiO<sub>2</sub> nanoparticles (SiONP), and a negatively charged species; 100 nm diameter polystyrene microspheres (PMS). In buffers of low pH, they have shown to organize into hierarchical binary structures where smaller SiONPs form a shell around the larger PMS [1]. The principal instrument of investigation has been a probe-corrected scanning transmission electron microscope (JEOL ARM200CF) and a commercial liquid cell holder (Ocean, DENSsolutions).

To directly image the structure and dynamics of this binary system poses some experimental challenges. Notably, the following questions are to be addressed:

- How to achieve sufficient *lateral and temporal resolution* for imaging dynamics of low-atomic number materials?
- How to account for the *electron-beam induced effects* and *contamination-induced* artifacts in the data?
- How to *confine a colloidal self-assembly reaction* in a nanofluidic cell?

To give some background, the essential instrumentation and the theory of image formation in electron microscopy (LPEM) will be presented. Secondly, selected LPEM

literature from the field of soft matter science [2] will be discussed. Specifically, the novel insights and experimental methods promoting reproducibility in LPEM are highlighted.

The experimental part of the thesis will start by *in silico* optimization of imaging parameters of scanning transmission electron microscopy (STEM) for low-Z colloids in water. Optimization is achieved by simulating image data in Casino-software [3, 4] by varying key parameters of both the sample and the microscope. Moreover, the method used to quantify the image quality and to describe the visibility of multi-pixel objects is discussed in detail. For the chosen imaging mode, namely annular dark-field STEM (DF-STEM), simulations are validated against experimental data, and the radiation effects on the sample components (PMS and SiONP) are discussed. After this, the structure of pre-assembled binary structures is studied in liquid.

In the second experimental part of the thesis, two recent improvements to the liquid cell design are tested. In the first case, a pressure controller setup developed by Dr. Sercan Keskin [5] is tested as a method to enable Fresnel-contrast imaging of colloidal assemblies in thin liquid layers using bright-field transmission electron microscopy (BF-TEM). In the final experimental chapter, a novel microchip design patented by Prof. de Jonge [6] is tested in order to gain more control over colloidal reactions inside the liquid cell.

In the conclusions, the impact of findings made in this thesis will be discussed, and a generally applicable workflow for designing an LPEM experiment will be presented. We hope that this will offer valuable insight for the reader to who wants to plan and conduct an LPEM-experiment while avoiding some of the pit holes that may undermine the reproducibility of the obtained results.

## **1.2 Electron microscopy of structures and processes of soft matter**

Soft matter is a broad term describing many materials that can show translational or conformational changes in room temperature. Typical examples include hydrated gels, liquids, polymers, biological membranes, and proteins. Also, colloidal systems such as solvated nanoparticles studied in this thesis can be considered as soft matter [7].

A challenge for studying soft materials with electron microscopy (EM) is the inherent incompatibility of any type of hydrated sample with the high vacuum conditions needed to generate and manipulate an electron beam. The column packed with all the electro-optical elements of an electron microscope is typically maintained in a vacuum in the range of  $10^{-5}$ - $10^{-9}$  Pa [8]. If a biological or other hydrated aqueous sample is inserted into the vacuum, this leads to evaporation and rapid drying, resulting in the collapse of the sample structure due to the high surface tension of water [9]. In biological specimens, the drying of the sample leads to irreversible structural destabilization of secondary protein structures and amphiphilic membranes.

Several methods have been developed to avoid artifacts that are created when water is removed from the sample. For example, to preserve the structural protein network in whole cells, it can be chemically cross-linked (fixing), so that the native water is removed in a controlled way and replaced by resin. This results in a solid sample that can be cut into thin slices suitable for EM studies [10]. Another way to avoid drying of a hydrated or aqueous sample is to plunge-freeze a thin layer of liquid on a supporting film so that the solutes can be imaged embedded in amorphous ice [11]. During the past decades, cryogenic electron microscopy (cryo-EM) has developed into a method that can be used to determine molecular structures of biomolecules on the atomic scale by applying so-called “single-molecule imaging” [12].

Structural studies typically offer snapshots of atoms, nano-objects, or their assemblies. Many questions in biology and technology, however, revolve around transformations that these structures undergo in response to their environment. Some examples of such systems include battery electrodes, solid catalysts, biomolecules, and whole living cells. In time-resolved cryo-EM, special techniques are used to initiate reaction on the sample support and then frozen shortly after [13]. *In situ* (or *operando*) EM utilizes special techniques where the sample can be biased by mechanical, physical, or chemical means to initiate and sustain a specific reaction inside the microscope [14]. If the reaction requires a gaseous or liquid environment, then a technical solution is needed to isolate the reaction volume from the vacuum in the microscope column [15]. The specialized environmental

microscopes use a controlled gas flow to pressurize the whole specimen chamber for the atmosphere [16, 17]. Another option for controlling the specimen environment is to use special holders that confine the gas or liquid environment between electron transparent windows so that a standard microscope column can be used [18, 19].

### **1.3 Instrumentation and sample preparation in LPEM**

#### **1.3.1 Liquid-cell holders with nanofluidic devices.**

The most common liquid cell systems utilize nm-thin, free-standing silicon nitride ( $\text{SiN}_x$ ) membranes to protect the liquid sample from evaporating when inserted in the vacuum of the microscope. As a result, these membranes act as relatively electron-transparent “windows” that allow the electron beam to probe the confined liquid specimen. While some models of these nanofluidic devices can fit the tip of standard sample holder [20], often specialized holders are used where the tip of the holder has a design that allows hermetical sealing of the liquid sample between two membranes by utilizing a lid that is screwed against the body of the holder [21]. Free-standing membranes are supported by separate silicon frames or “chips” that are pressed against each other to form a channel that has pre-defined height determined by the spacer, typically 0.2-10  $\mu\text{m}$  in LPEM experiments. In “direct loading”, the liquid sample is loaded into a nanofluidic device by pipetting a small amount of liquid on one of the chips, and then two chips are pressed together to seal the cell [22]. In some cases, the liquid cell can be assembled “in air” [23], after which the liquid containing the solutes of interest is simply flowed in. The “In air”-approach has been claimed to produce a thinner liquid layer than the direct loading method [24] but has not always been a successful method for loading colloidal samples into the liquid cell [25].

Many holder designs incorporate a tubing that allows changing the liquid medium in the tip area employing a liquid flow induced by a piston-driven syringe pump or pressurized gas. Two principal types of liquid flow cells exist [2]. In “bypass” design, the liquid flows in the sealed volume surrounding the nanofluidic device. The flow in the device is thus determined by the resistances of the nanochannel and bypass channel of the surrounding

volume [26]. The “direct flow” design utilizes a microfluidic design where the whole volume of the liquid flow passes through the imaging area, which enables the direct measurement of the liquid flow through the imaging segment [27, 28]. For analytical applications where optimized sample geometry for energy-dispersive x-ray spectroscopy (EDX) is needed, special lid designs are available that do not prohibit the travel of x-rays from the area of the electron-transparent windows to the detector located above the sample [29].

The standard approach for manufacturing components needed for nanofluidic devices is a multi-step process that requires cleanroom technology and utilizes techniques developed in the semiconductor industry. The free-standing SiN<sub>x</sub>-membrane is manufactured by the following steps [30]:

- 1) A SiN<sub>x</sub>-layer of thickness 10–100 nm is created on both sides of a polished silicon frame (typically 0.3-0.4 mm in thickness) by using low-pressure chemical vapor deposition.
- 2) Photolithography or reactive-ion etching is used to selectively etch an aperture through the silicon frame so that only the one free-standing membrane remains on the other side of the aperture.

Wafer-bonding techniques have been used to create monolithic liquid cells suitable for electron holography [31]. More complex [6] nanofluidic geometries have been realized by using additional etching steps to construct direct flow cells with well better-defined flow characteristics [27].

### **1.3.2 Alternative ways to introduce water into the electron microscope**

In open-cell TEM [15, 32] and environmental scanning electron microscopy (ESEM) [33], the sample is kept in a controlled atmosphere by utilizing differential pumping in the column of the microscope. The condensation of liquid water on the sample can be achieved by adjusting the partial pressure of the water and temperature of the sample. In a dedicated open-cell instrument, the detection via TEM and STEM is possible, including

analytical EM with EDX and EELS. In ESEM, the detection can be achieved via secondary, backscattered, or transmitted electrons [34] and is compatible with EDX.

2D-crystals such as graphene [35], graphene oxide [36], and molybdenum disulfide [37] are ideal candidates for electron transparent windows due to their near-atomic thickness. These materials can confine small spherical liquid pockets [38] that have been used to study nucleation and growth of nanoparticles [35] as well as the structure [39] and dynamics [40] of biomolecules and also the chemical structure of water and ice [41]. Novel nanofabrication methods such as reactive ion etching have been used to tailor graphene liquid cells (GLC) into structures with controlled liquid thickness [42] and flow capabilities [43]. Finally, graphene encapsulation can be used to cover bulky samples, such as whole cells, to protect them from drying [44]. Furthermore, the graphene coating has been combined with immunochemical labelling and correlative light microscopy to enable investigation of membrane receptor distribution of intact cancer cells with nanometer resolution [45].

### **1.3.3 Modification of nanofluidic devices for imaging structures and processes in liquid**

SiN<sub>x</sub>-based nanofluidic devices are often optimized for specific types of samples and experiments. The thickness of the spacer material defines the height of the nanochannel and protects bulky samples from deformation when chips are pressed together. For instance, when whole eukaryotic cells were imaged in a liquid cell, a spacer thickness of 4-6 μm was used with a membrane thickness of 50 nm [46]. The thickness of the window can be reduced if some of its physical rigidity can be traded for potentially higher spatial resolution. For example, 2.7 nm-resolution imaging of unstained acrosomal bundles was achieved by using 0.08 - 0.35 μm spacer heights and 10 nm thick membranes. The spacer is typically prepared using physical vapor deposition (PVD) so that a thin metal layer is deposited on the chip. Chips with additional metal layers can be manufactured, enabling heating and electrochemical biasing for advanced *in situ* experiments [27].

The surface of the exposed SiN<sub>x</sub>-membrane is covered with oxide groups, which renders it hydrophilic and gives it a negative net charge in aqueous solutions. The surface chemistry of the membrane can be tuned by electric plasma-discharge in oxidative (O<sub>2</sub>) or reductive (H<sub>2</sub>), or neutral (Ar) atmospheres [30]. In [47], it was shown that if the membrane was freshly treated with O<sub>2</sub>-plasma, metal-organic framework particles adhered firmly to the surface of the membrane, which allowed to record images of individual particles. If chips were left in contact with ambient air for 1-2 hours after plasma cleaning, translational dynamics and self-assembly into larger structures were observed. Secondly, wet chemistry methods have been used to modify SiN<sub>x</sub> -surface covalently or non-covalently. Aminopropyltriethoxysilane was used to decorate the surface with amino-groups that promoted the immobilization of citrate-capped AuNP's on the solid-liquid interface [48]. In order to improve biocompatibility, the surface can be treated with poly-L-lysine, which adsorbs on the surface spontaneously, and results in a platform suitable for cell culturing [49]. More specific tethering of viral particles has been demonstrated by modifying the surface with a lipid layer conjugated with antibodies against the viral surface proteins [50].

#### **1.4 Microscope types**

A transmission electron microscope (TEM) consists of a vacuum column that, on one end, is the electron source and, on the other end, is a detector. A uniform illumination pattern is projected on the sample surface resulting in a shadow image that is collected by the objective lens. A series of electromagnetic post-specimen lenses are used to magnify the image of the transmitted beam on the camera-type detector.

Scanning transmission electron microscope (STEM) uses electromagnetic condenser lenses to create a sub-nm, convergent electron probe that is scanned across the specimen surface using electric coils. The specimen is thus sampled one location at a time, where the local transmittance of the electron probe is detected [51]. STEM does not require post-specimen optics like TEM, and this provides an advantage when imaging thick samples such as ones encountered in LPEM [52] and electron tomography [53].

Scanning electron microscope (SEM) also uses a scanning, convergent probe like STEM, but now secondary electrons emitted or backscattered from the surface are detected [54]. Detection with BF-STEM and DF-STEM is also possible [55].

Electron microscopes can also be used to study the elemental and elemental composition [56]. The elemental composition can be probed with energy-dispersive x-ray spectrometry (EDX), where an x-ray detector is placed above the specimen surface. X-rays are generated in the sample when the electron beam interacts with the inner shell electrons of an atom. The valence electron configuration of the sample can be probed with electron energy-loss spectrometry (EELS), where the transmitted electron beam is analyzed by a dedicated spectrometer. The applicability of EELS is limited to TEM and STEM instruments, while EDX can also be combined with SEM.

#### **1.4.1 Electron optical system of the electron microscope**

An electromagnetic lens consists of a coil that creates a non-uniform magnetic field with rotational symmetry when direct current is passed through the coil. Analogous to optical lenses, electrons passing the lens are sent to trajectories crossing the optical axis at the focal distance  $f$  from the lens. In contrast to optical lenses, when an electron traverses the magnetic field, it is affected by axial, radial, and tangential forces relative to the cylindrical lens. This results in a spiraling trajectory of passing electrons, which effectively causes image rotation relative to the object [8].

#### **1.4.2 Magnification and multi-stage imaging**

Geometric optics adapted from light microscopy can be used to describe how the object at a distance of  $g$  from the lens is focused on the image plane at a distance of  $b$  on the opposite side of the lens [57].

$$\frac{1}{f} = \frac{1}{g} + \frac{1}{b} \quad (\text{Eq. 1.1})$$

Where  $f$  is the focal length of the lens. Here, the thin lens approximation is made, which assumes that all the rays will be bent precisely in the middle of the lens.

The magnification factor ( $M$ ) of the lens is defined as the ratio of the image size ( $y'$ ) and object size ( $y$ ), which equals the ratio between the distance of the object from the lens.  $M$  can be calculated by solving  $g$  and  $b$  from the Eq. 1.1.

$$M = \left| \frac{y'}{y} \right| = \left| -\frac{b}{g} \right| = \left| \frac{f}{f-g} \right| \quad (\text{Eq. 1.2})$$

In electron microscopes, the vertical positions of all lenses and the detector are fixed. In order to adjust the magnification, the strength of lenses is adjusted instead [8].

Pre-specimen electromagnetic lenses are used to magnify or demagnify an image of the electron source on the specimen. Thus condenser lenses (CL) and condenser lens aperture (CLA) are be adjusted so that an ideally uniform illumination pattern is projected on the specimen surface.

Post-specimen lenses collect the transmitted beam and magnify on the detector. The lens after the specimen is called the objective lens (OL), which is followed by an objective lens aperture (OLA) and, typically, several projector lenses (PL).

The effective focal length for two lenses in a row, separated by a distance  $o$  can be calculated by using Eq. 1.3.

$$\frac{1}{f_{eff}} = \frac{1}{f_1} + \frac{1}{f_2} - \frac{o}{f_1 \cdot f_2} \quad (\text{Eq. 1.3})$$

## 1.5 Electron scattering from the sample

From a physical point of view, electrons can be treated as particles or as waves. For the particle approach, scattering contrast theory describes intensity variations in electron micrographs by considering the local transmittance of electron particles through the specimen [8]. This approximation agrees well for STEM and is also valid for TEM when low and medium magnifications and if small values of defocus are used [58]. The wave nature of electrons can be described by the wave mechanistic approach and observed intensity variations can be related to the amplitudes and phases of the transmitted electron waves. The wave mechanical treatise is not in the scope of this thesis, but the possibility to utilize phase contrast LPEM will be addressed in section 1.9.

When electrons are treated as particles, the interaction between the electron beam and matter is understood to take place as discrete, localized events that have a certain probability ( $p$ ) depending on the material's thickness ( $t$ ), atomic weight ( $W$ ), density ( $\rho$ ), and partial scattering cross-section ( $\sigma(\theta)$ ):

$$p = \frac{1}{l} = \frac{N_A \cdot \sigma(\theta) \cdot \rho \cdot t}{W} \quad (\text{Eq. 1.4})$$

Where  $l$  is the mean-free path, describing the probable distance that the electron will travel in the material between scattering events, and  $N_a$  is the Avogadro's constant.

Images are formed because there are local differences in the transmittance of the electron beam. In thin samples, electrons that are not transmitted through the specimen are typically not absorbed by the specimen but rather scattered to high angles so that they do not land on the detector. The detector has a defined collection semi-angle that is defined by the size of the detector itself ( $\beta$ , STEM) or by an aperture located at the back focal plane of the objective lens ( $\alpha$ , TEM).

Transmittance  $T(\beta)$  of the electron beam reaching the detector can be calculated by using the exponential transmission law [59]:

$$T(\beta) = \frac{N}{N_o} = e^{-t/l(\beta)} \quad (\text{Eq. 1.5})$$

, where  $N_o$  is the number of incident electrons, and  $N$  is the number of transmitted electrons. This law can also be used to evaluate the thickness of the specimen [60].

The  $\sigma(\theta)$  can be divided into two terms: elastic scattering and inelastic scattering.

$$\sigma(\theta) = \sigma_{el}(\theta) + \sigma_{in}(\theta) \quad (\text{Eq. 1.6})$$

When elastically scattered, electrons interact mainly with single nuclei of the specimen, and there is little or no loss of energy. Inelastic scattering, on the other hand, takes place in the electron cloud [8]. From a practical point of view, the elastic scattering is useful in imaging, diffraction, and holographic applications. In contrast, inelastic scattering is mainly used in analytical applications where the elemental composition (EDX and EELS) or

characteristics of chemical bonding is probed (EELS). Also, secondary electrons often used for detection in SEM are created via inelastic interaction. Furthermore, energy deposited in the sample during inelastic scattering is the main cause of electron beam damage [61]. (See also Section 1.10)

The partial elastic scattering cross-section  $\sigma(\beta)$  is related to the probability of an electron scattering up to a certain angle when it passes an atom [8]. The screened, partial Rutherford elastic cross-section ( $\sigma_{el}(\beta)$ ) is given by

$$\sigma_{el}(\beta) = \frac{Z^2 R^2 \lambda^2 (1 + \frac{E}{E_0})^2}{\pi a_H^2} \frac{1}{1 + (\frac{\beta}{\theta_0})^2} \quad (\text{Eq. 1.7})$$

The total elastic cross-section indicating scattering to any given angle is obtained by setting  $\beta = 0$  rad.

At their best, elastic scattering cross-sections are known withing a factor of two [14], which will introduce a degree uncertainty to the calculations of scattering contrast and resolution. Results from more detailed calculations are tabulated [62] and can be used instead [4].

The inelastic scattering  $\sigma_{in}(\beta)$  is given by [58, 59]:

$$\sigma_{in}(\beta) = \frac{Z^2 R^2 \lambda^2 (1 + \frac{E}{E_0})^2}{\pi a_H^2} \left[ \frac{1}{4[1 + (\frac{\beta}{\theta_0})^2]} + \ln \sqrt{1 + (\frac{\beta}{\theta_0})^2} \right] \quad (\text{Eq. 1.8})$$

## 1.6 Electron-optical limitations of the microscope

In TEM, the image is often a 2D-presentation of the projected specimen morphology. An ideal image contains a projection of each point in the specimen and retains the relative orientation of these points. In practice, however, the ideal image is never achieved because 1) the sample itself is not 2-dimensional, 2) the *resolution* of the image is limited by the wavelength of the illumination, and 3) the lenses of the microscope introduce *aberrations* which distort the image. As will be discussed later in this thesis, also the

statistical variation in the detected signal will affect the perception of the image [63] and effectively increase the resolution.

Ernst Abbe first described the limits of magnification for light microscope by considering the minimum distance ( $d_D$ ) at which two point-like objects can be resolved as separate objects (also termed as Rayleigh-criterion of resolution) [57]:

$$d_D = \frac{1.22 \lambda}{n \sin \alpha} \quad (\text{Eq. 1.9})$$

, where  $\lambda$  is the wavelength of the illumination,  $n$  is the refractive index of the medium between the point object and the lens, and  $\alpha$  is the angle at which the lens after the specimen collects the transmitted beam.

Eq. 1.9 is applicable also for electron optics if the De Broglie-wavelength for relativistic electron speeds is considered:

$$\lambda = \frac{c h}{\sqrt{E^2 + 2 E_0 E}} \quad (\text{Eq. 1.10})$$

Where  $c$  is the speed of light,  $h$  is Planck's constant,  $E_0$  is the rest energy of the electron.

$$E_0 = m_0 c^2 \quad (\text{Eq. 1.11})$$

, and  $E$  is the energy of the accelerated electron.

$$E = U e \quad (\text{Eq. 1.12})$$

, where  $U$  is the acceleration voltage of the electron gun, and  $e$  is the elementary charge.

In the vacuum of the microscope, the  $n = 1$ , and the typical aperture size is  $10^{-2}$  rad. For  $U = 200$  kV,  $d_D = 0.16$  nm is obtained.

Electromagnetic lenses are prone to aberrations. Unwanted radial and azimuthal inhomogeneities in the magnetic field lead to spherical aberration ( $C_s$ ) and astigmatism, respectively [8].

$C_s$  is characterized by the size of the disc ( $d_s$ ) that a lens with opening  $\alpha$  produces when it focuses a point-like object on the (Gaussian) object plane (also termed as the disk of least confusion):

$$d_s = C_s \cdot \alpha^3 \quad (\text{Eq. 1.13})$$

, where  $C_s$  is the spherical aberration coefficient. Hence, when the opening angle of the lens is made smaller, better resolution can be attained. This, however, has its limitation as the diameter of the aberration disc will start increasing for small values of  $\alpha$  when the so-called diffraction limit for  $\alpha$  is reached (Eq. 1.9).

The third type of major aberration inherent to electromagnetic lenses is the chromatic aberration ( $C_c$ ), which is due to the fact that electrons with different energies are focused on different planes. If there is a considerable distribution in the electron energies in a point-like electron beam, these will result in a disc of a size  $d_c$  on the image plane. The energy distribution is dependent on the quality of the electron source as well as the thickness of the sample. Due to the fluctuations in the current that is used to drive the lenses, there is temporal incoherence in the magnetic field that focuses the electrons. The size of the aberration disc is given by:

$$d_c = C_c \cdot \frac{\Delta E}{E_0} \cdot \alpha \quad (\text{Eq. 1.14})$$

, where  $\Delta E$  is the energy spread of the electron beam, and  $E_0$  is the incident energy of the beam.

Astigmatism is caused by the azimuthal inhomogeneities in the magnetic field, and it will cause elongation of point objects into elliptical objects. If the sample plane is described by two axes-x and y, there is hence a difference in the focal length ( $\Delta f_a$ ) how these axes are projected on the image plane [57]. The radius longer axis of this ellipse ( $d_a$ ) is given

$$d_a = \frac{1}{2} \cdot \Delta f_a \cdot \alpha \quad (\text{Eq. 1.15})$$

## 1.7 Theory of attainable resolution of and contrast of spherical nano-objects in LPEM

A theoretical framework for evaluating attainable contrast and resolution in LPEM and cryo-EM has been presented in [59].

The spatial resolution of an optical device typically refers to the smallest distance ( $d$ ) between two objects, where they are still resolved as separate objects, also known as Rayleigh-criterion. In sufficiently thin samples, in which objects of interest show good contrast, the resolution of an electron microscope is limited by its optics, but in thicker and more beam sensitive samples, also beam broadening and noise need to be considered.

In STEM, the maximal resolution for an optimal sample is limited by the size of the electron probe. The diameter of a diffraction-limited electron probe that contains 50 % of the original current is

$$d_{\text{diff}} = \frac{0.54 \lambda}{\alpha_p} \quad (\text{Eq. 1.16})$$

In addition, the probe size is limited by the spherical aberration of the condenser lens ( $c_s$ ). The diameter of the electron probe that contains 50 % of the incident electrons is

$$d_{cs} = \frac{\sqrt{2} \alpha_p^3 c_s}{8} \quad (\text{Eq. 1.17})$$

The combined effect of multiple resolution-limiting terms can be combined by summing them in a quadrature manner [8]. Hence, the final resolution due to the limitations of electron optics, namely diffraction and  $C_s$ , is obtained by

$$d_{50} = \sqrt{d_{\text{diff}}^2 + d_{cs}^2} \quad (\text{Eq. 1.18})$$

The diameter of the electron beam becomes broader when it interacts with the sample. The effect of the beam broadening on the disc that contains 50 % of the original current at the depth  $z$  of the sample is given by ([58, 59])

$$d_{blur\_50} = \frac{1.5}{2} \frac{\lambda^2}{2\pi\alpha_H} Z^{1.5} \sqrt{\frac{N_A \rho}{3\pi A}} Z \left(1 + \frac{E}{E_0}\right) \quad (\text{Eq. 1.19})$$

In case a liquid cell is used for imaging, both the effect of SiN<sub>x</sub>-windows of thickness  $t_{SiN}$  and the liquid layer with thickness  $t$  can be considered by adding up their contributions

$$d_{blur\_50} = d_{blur,SiN}(t_{SiN}) + d_{blur,H_2O}(Z) \quad (\text{Eq. 1.20})$$

### 1.7.1 Calculation of the detected signal in STEM

The detection configuration has an effect on the detected intensity of the electron beam and also how much the beam broadening will affect the data. STEM has two different types of detection schemes: bright field (BF) and dark field (DF). In BF-STEM, a circular detector with an opening semi-angle ( $\beta$ ) is placed under the transmitted beam, and the intensity is recorded. In DF-STEM, an annular detector with an inner opening semi-angle ( $\beta$ ) is used.

In order to calculate the intensity ( $M_{bkg}$ ) of the transmitted beam in BF-STEM at a position of only water and SiN<sub>x</sub>-membrane, Eq. 1.5 can be arranged to give

$$M_{bkg} = N_0 e^{-\frac{t}{l_{H_2O}} - \frac{2t_{SiN}}{l_{SiN}}} \quad (\text{Eq. 1.21})$$

At the location of the nano-object, the transmitted intensity ( $M_{signal}$ ) is given by

$$M_{signal} = N_0 e^{-\frac{d-t}{l_{H_2O}} - \frac{2t_{SiN}}{l_{SiN}} - \frac{d}{l_o}} \quad (\text{Eq. 1.22})$$

In DF-STEM, the electron intensity ( $N$ ) at the detector is given by

$$N_{bkg} = N_0 - N_0 e^{-\frac{t}{l_{H_2O}} - \frac{2t_{SiN}}{l_{SiN}}} \quad (\text{Eq. 1.23})$$

$$N_{signal} = N_0 - N_0 e^{-\frac{d-t}{l_{H_2O}} - \frac{2t_{SiN}}{l_{SiN}} - \frac{d}{l_o}} \quad (\text{Eq. 1.24})$$

If there is no correlation between the fluctuations of the pixels in the image, the noise follows Poisson-statistics. Therefore, the level of noise in the observed signal is

proportional to the square root of the number of electrons hitting the detector [64]. In case of the BF-STEM and assuming that  $M_{signal} \sim M_{bkg}$ , the SNR is then

$$SNR = \frac{M_{signal} - M_{bkg}}{\sqrt{M_{bkg}}} \quad (\text{Eq. 1.25})$$

Eq. 1.25 can be used to calculate the SNR of a pixel located in the middle of a nano-object of diameter  $l_o$ . In order for such a pixel to be visible to eyes, the Rose-criterion,  $SNR \geq 3-5$ , should be fulfilled depending on the geometry of the object [63].

The detection configuration will also influence the *effective* beam broadening described by the Eq. 1.19 when  $z > 0$ . In the case of DF-STEM, the effect of beam blurring on the probe diameter containing 50 % of the current is given directly by the Eq. 1.19 so that the effective beam broadening will increase with  $z$  indefinitely. In BF-STEM, the situation is, however, different. In terms of the  $d_{blur\_50}$ , the electron beam broadening is affected only up to the point where the “divergence angle” caused by the beam broadening  $\theta_{50}$  is less or equal to the collection angle of the BF-detector. After  $\theta_{50}$  becomes greater, only the intensity of the detected beam will be affected, which will be omitted here. The  $\theta_{blur\_50}$  can be calculated by first obtaining the  $d_{blur\_50}$  at the middle of the sample ( $z/2$ ) and the surface of the sample:

$$\theta_{blur\_50} = \text{atan}\left(\frac{d_{50}}{z}\right) \quad (\text{Eq. 1.26})$$

Thus, the beam blur limited resolution in BF-STEM is given by two separate cases:

$$d_{blur\_50\_BF} = \begin{cases} \tan(\theta_{blur\_50}) * z & , \text{when } \theta_{blur\_50} < \beta \\ \tan(\beta) * z & , \text{when } \theta_{blur\_50} > \beta \end{cases} \quad (\text{Eq. 1.27})$$

### 1.7.2 SNR-limited resolution in STEM

In [59], an analytical solution was derived for SNR-limited resolution in STEM ( $d_{SNR}$ ). According to the Nyquist-sampling theorem, the sampling frequency, i.e., the reciprocal of the pixel size ( $s$ ), needs to be at least twice the intended resolution of the experiment. In addition, another practical condition will be applied in order to avoid high local electron

doses: the electron probe diameter will be adjusted so that the  $d_{50}$  can just fill the pixel area and thus

$$d_{SNR} = 2d_{50} \quad (\text{Eq. 1.28})$$

The  $N_0$  is given

$$N_0 = D_e * s^2 \quad (\text{Eq. 1.29})$$

, where  $D_e$  is the electron dose in  $e^- m^{-2}$ .

Combining Eq. 1.28 and 1.29 results in

$$D = \frac{4N_0}{d_{SNR}^2} \quad (\text{Eq. 1.30})$$

As shown in [59], an analytical solution reveals that the  $d_{SNR} \propto D_e^{1/4}$  and the  $d_{SNR}$  can also be solved numerically.

The final resolution for DF-STEM is given by

$$d_{STEM\_DF} = \sqrt{(2d_{50})^2 + d_{SNR}^2 + d_{blur\_50}^2} \quad (\text{Eq. 1.31})$$

And for BF-STEM

$$d_{STEM\_BF} = \sqrt{(2d_{50})^2 + d_{SNR}^2 + d_{blur\_50\_BF}^2} \quad (\text{Eq. 1.32})$$

### 1.7.3 SNR-limited resolution in TEM

To calculate the resolution for BF-TEM scattering contrast, also the  $C_s$  and  $C_c$  of the objective lens need to be included in the calculations.

The formula for Scherzer-resolution ( $d_{sch}$ ) gives the  $C_s$ -limited resolution in BF-TEM -mode where the small amount of defocus is applied to compensate the  $C_s$  of the objective lens.

$$d_{sch} = 0.66 c_s^{1/4} \lambda^{3/4} \quad (\text{Eq. 1.33})$$

The effect of the energy spread of the transmitted beam to the achievable resolution ( $d_{cc}$ ) is

$$d_{cc} = 0.5 c_c \alpha (\Delta E(x)/E) \left( \frac{1+E/E_0}{1+E/2E_0} \right) \quad (\text{Eq. 1.34})$$

, where  $\alpha$  is the opening semi-angle of the objective lens aperture, and  $\Delta E(x)$  is the energy broadening of the electron beam when it has penetrated the material with thickness  $x$ .

$$\Delta E(x) = \frac{N_a Z c^2 e^4 \rho x}{2 W \epsilon_0^2 v^2 \pi} \quad (\text{Eq. 1.35})$$

Where  $\epsilon_0$  is the permittivity of the vacuum and  $v$  is the relativistic velocity of the electron

$$v = c \sqrt{1 - \frac{1}{\left(\frac{E}{E_0} + 1\right)^2}} \quad (\text{Eq. 1.36})$$

In order to calculate the total effect of energy spread to the  $C_c$ -limited resolution ( $d_{TEM_{cc}}$ ), both the effect of the window ( $d_{cc_{SiN}}$ ) and water ( $d_{cc_{H2O}}$ ) need to be included, as well as the energy spread of the electron source ( $\Delta E_{source}$ ):

$$d_{TEM_{cc}} = \sqrt{(d_{cc_{H2O}}^2 + d_{cc_{SiN}}^2 + d_{source}^2)} \quad (\text{Eq. 1.37})$$

The effect of beam blurring in BF-TEM can be calculated by using the Eq. 1.19, but it differs from STEM in a significant way: Instead of the probe broadening taking place in STEM, it is the details in the “shadow image” of the transmitted electron beam that become blurred in BF-TEM. For this reason, the  $z = 0$  position for BF-TEM is at the exit side of the sample in BF-TEM.

The final resolution for scattering contrast in BF-TEM is obtained by

$$d_{tem} = \sqrt{d_{SNR,BF}^2 + d_{blur}^2 + d_{cc_{TEM}}^2 + d_{sch}^2} \quad (\text{Eq. 1.38})$$

## 1.8 Attainable resolution for polystyrene, silica, and gold

By applying the presented theory [59] on polystyrene ( $C_8H_8$ ), amorphous silicon oxide ( $SiO_2$ ), and gold (Au), the relative importance of different resolution-limiting factors in liquid-cell EM will be discussed.

### 1.8.1 The effect of $D_e$

The effect of the  $D_e$  and the detector opening angle was compared on the attainable resolution for three materials, as is shown in Fig. 1.1. In addition, resolution limiting terms were plotted, and the optimal detector setting and the corresponding value of resolution is indicated for parameters  $D_e = 100 \text{ e}^-\text{\AA}^{-2}$  and  $t = 300 \text{ nm}$ . For more details about calculations, see Chapter 2: Methods and Supplementary Information.

The first thing to notice is that almost in all the cases, the resolution is limited by the low SNR of the image ( $d_{SNR}$ ), and thus increasing the  $D_e$  does not affect the optimal  $\alpha, \beta$ . The only exception is when the Au nano-object is imaged in BF-TEM, and the  $d_{cc}$  becomes the resolution-limiting term for  $\alpha \gtrsim 15 \text{ mrad}$ . It can be thus concluded that for the low-Z material, such as  $C_8H_8$  and  $SiO_2$ , the attainable resolution is not limited by the optical quality of the microscope but rather the scattering properties of the sample. Furthermore, increasing  $D_e$  by a magnitude will give roughly half of the original resolution, which agrees with the scaling law  $d_{SNR} \propto D_e^{1/4}$  derived in [59].

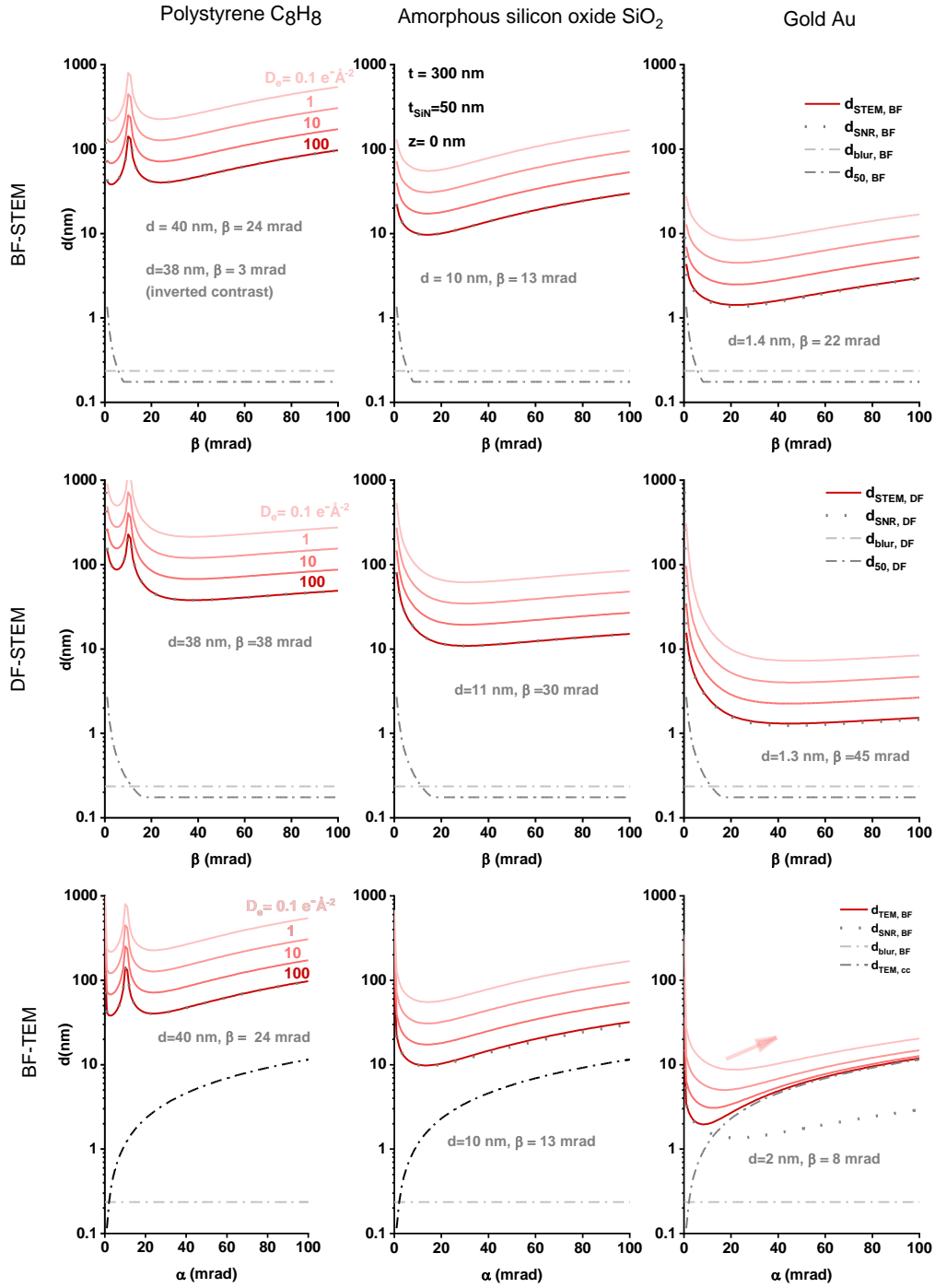


**Figure 1.1** The attainable spatial resolution ( $d$ ) and resolution-limiting terms when the electron scattering theory [59] is applied for LPEM. The  $d$  based on the scattering contrast was calculated for polystyrene, amorphous silicon oxide, and gold (columns) while using imaging modes BF-STEM, DF-STEM, and BF-TEM (rows). The  $d$  was calculated as a function of detector collection angle ( $\beta$ , STEM or  $\alpha$ , TEM) and plotted for electron doses ( $D_e$ ) 0.1, 1, 10, and 100  $\text{e}^- \text{\AA}^{-2}$  in a liquid cell with the liquid thickness ( $t$ ) 300 nm, silicon nitride thickness ( $t_{\text{SiN}}$ ) 50 nm, and distance of nano-object from the window ( $z$ ) set to 0 nm. Resolution-limiting terms from Eq.

1.31, Eq. 1.32, and Eq. 1.38 were plotted to demonstrate their relative importance in the image formation. The arrow at the lower right corner (BF-TEM, gold) illustrates how the optimal  $\alpha$  for Au increases along with the decreasing  $D_e$  due to the similar magnitudes of chromatic aberration limited resolution ( $d_{cc}$ ), and signal-to-noise-limited resolution ( $d_{SNR}$ ).

### 1.8.2 The effects of $t$ and the windowless imaging

The sample thickness has an effect on the attainable resolution in electron microscopy. In LPEM, the sample thickness can be adjusted by changing  $t$  or  $t_{SiN}$ . In Fig. 1.2, the effect of increasing the  $t$  from 300 to 650 and 1000 nm is directly compared with the effect of using an order of magnitude higher or lower value of  $D_e$ . In addition, the effect of removing two SiN<sub>x</sub>-windows is shown for  $t = 300$  nm for  $D_e = 10 \text{ e}^{-\text{\AA}^{-2}}$ .

When the optimal detector setting is used, increasing  $t$  from 300 to 1000 nm has less effect on the attainable resolution than decreasing the  $D_e$  from 10 to  $1 \text{ e}^{-\text{\AA}^{-2}}$ . When a liquid cell with ultra-thin windows, such as one fabricated from graphene [39], is used, it can have a considerable effect on the attainable resolution.

If the maximal attainable resolution for polystyrene and silica is sought for, it should be obtained either with BF-STEM or BF-TEM by carefully adjusting the  $\alpha$ ,  $\beta$  to a value which depends on the  $t$  (Tilted arrows). However, DF-STEM does have an advantage from a practical point of view: at higher values of  $\beta$ , the attainable resolution is relatively constant, and thus nearly-optimal detection independently of the  $t$  can be achieved by simply selecting a large enough value of  $\beta$  (horizontal arrow). For gold, the DF-STEM seems to give the optimal resolution. It could be thus concluded that based on the scattering theory, DF-STEM should give a good all-around performance for a range of materials in liquid.

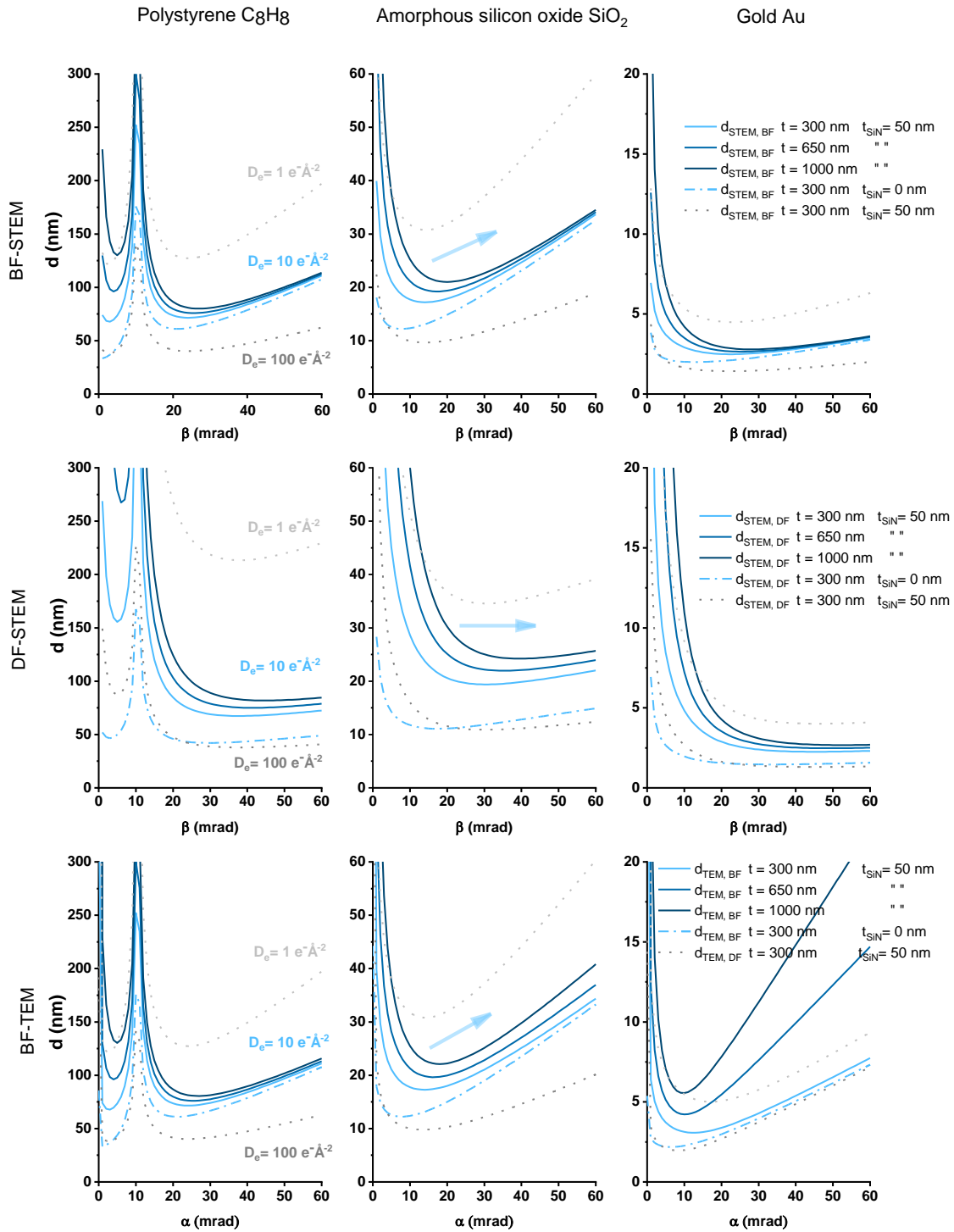


**Figure 1.2.** The effect of  $t$  and  $t_{SiN}$ , on the attainable resolution and optimal detector collection angle ( $\beta$ ,  $\alpha$ ). The  $d$  was plotted as a function of  $\beta$ ,  $\alpha$  using  $D_e = 10 e^{-\text{\AA}^{-2}}$  for  $t = 300, 650, 1000$  nm, and  $t_{SiN} = 50$  nm. To illustrate the relative effect of the SiN-windows on the attainable resolution,  $d$  was plotted also for  $t = 300$  and  $t_{SiN} = 0$  nm. To directly compare the effect of  $t$  and  $t_{SiN}$  with the effect of magnitude higher and lower  $D_e$ , the attainable resolution was also plotted for  $t = 300$ ,  $t_{SiN} = 50$  nm using both  $D_e = 100 e^{-\text{\AA}^{-2}}$  and  $1 e^{-\text{\AA}^{-2}}$ . The horizontal arrow on the middle row

illustrates how the attainable resolution in DF-STEM is relatively insensitive for larger values of  $\beta$  even when the  $t$  is changed. For BF-STEM and BF-STEM, however, there is a clear minimum in the curve indicating that an optimal  $\beta, \alpha$  exists for BF detection.

### 1.8.3 The effect of beam broadening

The beam broadening can have an effect on the attainable resolution and is dependent on the properties of the window and how far the nano-object is located from it ( $z$ ) [65]. The effect of beam broadening was studied in the case of BF-STEM when silica nano-object is imaged in  $t = 300, 650,$  and  $1000$  nm and using  $D_e = 10 \text{ e}^{-\text{\AA}^{-2}}$ , and comparing  $z = 0$  against  $z = t$ . The effect of beam blurring only seems to have a noticeable effect on the attainable resolution when  $z = 650$  or  $1000$  nm, as is shown in Fig. 1.3.

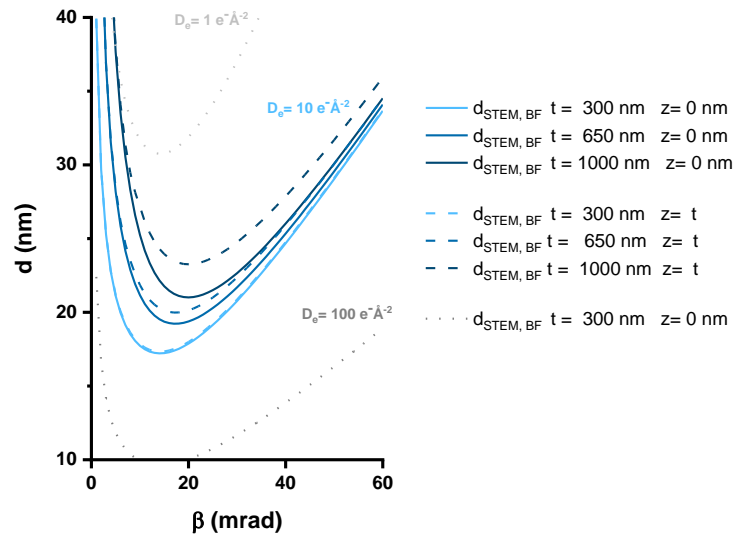


**Figure 1.3** The effect of beam broadening on the attainable spatial resolution of BF-STEM when imaging  $\text{SiO}_2$  nano-objects in a liquid cell with  $t_{\text{SiN}} = 50 \text{ nm}$  and  $D_e = 10 \text{ e}^{-\text{\AA}^{-2}}$ . The increase in resolution is caused by the beam broadening determined by Eq. 1.27.

### 1.8.4 The effect of inelastic scattering

The inelastic scattering does not greatly constitute the total scattering cross-section for high values of  $\beta$ , and hence, in some cases, it has been omitted when estimating the image formation via scattering contrast [4]. In Fig. 1.4, the effect of setting the  $\sigma_{in} = 0$  in Eq. 1.6 is shown as dashed line for DF-STEM, BF-STEM, and SiO<sub>2</sub>. For small values of  $\beta$ , the  $d$  will be underestimated, and thus too optimistic results may be obtained in case the inelastic scattering is omitted. In addition, the optimal  $\beta$  may move to lower values if inelastic scattering is omitted.

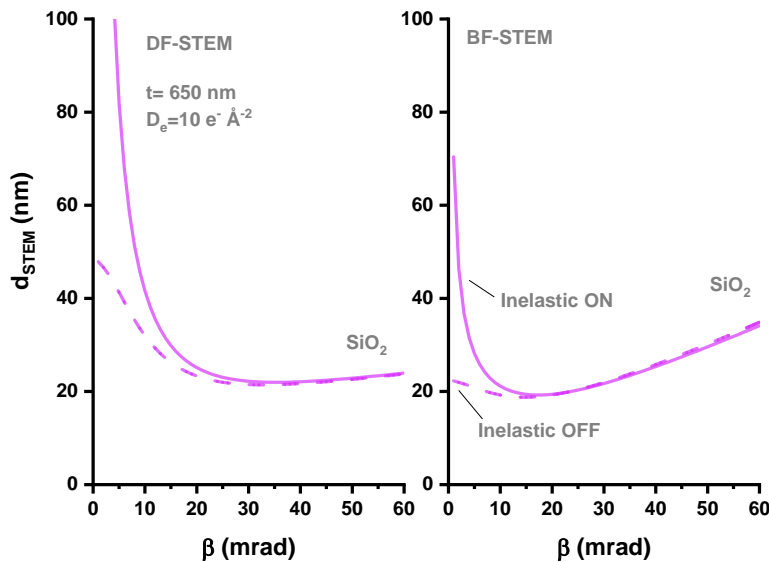


**Figure 1.4** The effect of inelastic scattering when calculating the attainable resolution based on scattering contrast for SiO<sub>2</sub>,  $t = 650$  nm,  $D_e = 10$  e<sup>-</sup>Å<sup>-2</sup>,  $z = 0$ . The theory predicts that  $d$  will be underestimated for small values of  $\beta$  if inelastic scattering is excluded when calculating the total scattering cross-section using Eq. 1.6.

## 1.9 Phase-contrast in LPEM and related systems

### 1.9.1 Theory of phase contrast

The scattering contrast does not account for the wave nature of electrons, and therefore, it does not accurately describe the image formation in BF-TEM when applied to high-resolution imaging or when using large values of defocus ( $\Delta f$ ). For example, when

biomolecules are imaged with high-resolution in cryo-EM, no objective lens aperture is used, and the contrast is created by slightly defocusing the objective lens [66]. This behavior is not predicted by the scattering theory described above.

The wave mechanistic approach considers the electron beam as a coherent electron wave,  $\Psi$ , that experiences a modulation of its amplitude ( $A$ ) and phase ( $\varphi$ ) due to the interaction with the sample [14]:

$$\Psi_{img}(x, y) = A(x, y) e^{i\varphi(x, y)} \quad (\text{Eq. 1.39})$$

When the modulated image wave  $\Psi_{img}$  is detected, the intensity ( $I$ ) at the detector is formally obtained via the multiplication of  $\Psi_{img}$  with its complex conjugate,  $\Psi_{img}^*$ .

$$I(x, y) = \Psi_{img}(x, y) \Psi_{img}^*(x, y) \quad (\text{Eq. 1.40})$$

The *amplitude* of the electron wave is modulated by three main mechanisms [14]: The scattering contrast modulates the intensity by blocking some of the electrons reaching the detector. Secondly, scattered, coherent electron waves can interfere, thus leading to intensity variations on the detector (e.g., diffraction). Third, inelastically scattered electrons modulate the amplitude because inelastic scattering adds only to the incoherent background intensity, but does not interfere with coherent unscattered or elastically scattered components of the transmitted electron wave.

The modulation of phase (i.e., phase -change) is given by

$$\varphi(x, y) = \sigma V_{proj}(x, y) - 2\pi \frac{e}{h} \Phi(x, y) \quad (\text{Eq. 1.41})$$

Where  $V_{proj}$  is the projected electric potential of the sample, and  $\Phi(x, y)$  is the magnetic flux experienced by the electron.  $\sigma$  is the interaction constant

$$\sigma = 2\pi \frac{e}{h v} \quad (\text{Eq. 1.42})$$

, where  $v$  is the relativistic velocity of an electron from Eq. 1.36.

For a sample that is homogenous in the direction of the electron beam, the projected electronic inner potential can be approximated

$$V_{proj}(x, y) = V_{MIP} t \quad (\text{Eq. 1.43})$$

Where  $V_{MIP}$  is the mean inner potential of the sample, and  $t$  is the thickness of the sample. The mean inner potential of liquid water was recently measured by using holographic methods and was found to be  $+4.48 \pm 0.19$  V [31]. For polystyrene, it was measured to be  $+8.5 \pm 0.7$  V [67].

When the amplitude contrast is negligible and the phase change while passing the sample is small, so-called weak phase object approximation can be made, and the detected intensity changes are related only to the phase-contrast by:

$$I(x, y) = 1 + \sigma \hat{V}_{proj}(x, y)t \otimes \widehat{PCTF} \quad (\text{Eq. 1.44})$$

, where  $\hat{V}_{proj}(x, y)$  is the inverse Fourier transform of the  $V_{proj}(x, y)$ ,  $\widehat{PCTF}$  is the inverse Fourier transform of the so-called phase contrast transfer function, and  $\otimes$  stands for convolution operation.

When considering the contrast arising from amorphous material with no crystalline order, the Fourier transform of  $V_{proj}$  relates to the so-called atomic electron scattering factor at zero angle,  $f_{el}(0)$  by

$$\sigma \hat{V}_{proj}(x, y) = \frac{f_{el}(0) \lambda}{V_{avg}} \quad (\text{Eq.1.45})$$

Where  $V_{avg}$  is the average volume of an atom and  $f_{el}(0)$  is the scattering factor for zero-angle. The  $f_{el}(0)$  can be directly calculated [59] by using the formula for screened, Wenzel-model, Rutherford elastic scattering cross-section [68]:

$$\frac{d\sigma_{el}(\theta)}{d\Omega} = |f_{el}(\theta)|^2 = \frac{\lambda^4 (1 + \frac{E}{E_0})^2}{4\pi^4 a_H^2} \frac{Z^2}{(\theta + \theta_0^2)^2} \quad (\text{Eq. 1.46})$$

Alternatively, tabulated values for  $f_{el}(0)$  calculated according to the Born-approximation [69] can be used [53]. For crystalline material, the  $f_{el}(0)$  needs to be substituted with the structure factor  $F(0)$  and  $V_{avg}$  with the volume of the unit cell.

For a given material, the average electron scattering factor is calculated by

$$f_{el}^{ave} = \sum_n f_n f_{el}^n(\theta) \quad (\text{Eq. 1.47})$$

, where  $f_n$  is the elemental fraction of the element  $n$ .

If the smearing caused by the  $\widehat{PCTF}$  is omitted, the phase-contrast for a spherical nano-object at optimal defocus is

$$C_{phase} = (N_o f_{el}^o(0) - N_w f_{el}^w(0)) \frac{2}{3} t_o \lambda \quad (\text{Eq. 1.48})$$

, where  $N$  is the number of atoms in a unit volume and can be calculated by:

$$N_n = \frac{\rho_n}{w_n} N_a \quad (\text{Eq. 1.49})$$

The attainable noise-limited resolution is given by [59]

$$d_{phase} = \frac{3}{2 ((f_{el}^o(0) - N_w f_{el}^w(0)) \lambda)^{1/2} DQE^{1/4} D^{1/4}} \quad (\text{Eq. 1.50})$$

Where DQE is the detection quantum efficiency defined as [70]

$$DQE = \frac{SNR_{out}^2}{SNR_{in}^2} \quad (\text{Eq. 1.51})$$

Where  $SNR_{in}$  and  $SNR_{out}$  are the signal-to-noise ratios of the detected signal and output of the detector, respectively.

Calculations in [59] show that the TEM phase contrast for carbon could outperform the BF-STEM scattering contrast when  $t < 100$  nm.

### 1.9.2 Challenges in the application of phase-contrast in LPEM

In order to achieve the predicted  $C_{phase}$  or  $d_{phase}$  in LPEM a degree of coherence in the transmitted beam is required. As a rule of thumb, it is assumed that Eq. 1.48 and Eq. 1.50

are applicable up to a sample thickness corresponding to half of the elastic mean-free path length. For water, this means approximately 160 nm when windows are excluded. This would suggest that in terms of the sample thickness, the phase-contrast is most useful when using graphene liquid cells [39] or ultrathin membranes [71].

When considering the application of phase-contrast in LPEM in a situation where medium resolution is sought (e.g., imaging nanoparticle dynamics as in this work), the usefulness of phase-contrast may be limited. This can be qualitatively understood by considering the Contrast Transfer Function (CTF). To illustrate this, the CTF was calculated for a partially coherent electron beam using readily available scripts [72, 73] and plotted in Fig. 1.5.

The CTF is an oscillating function that consists of two parts: Amplitude-CTF (ACTF) and Phase-CTF (PCTF), which are the real and imaginary parts of the Wave transfer function, respectively [14]. It is essential to notice that at small spatial frequencies (large objects), the phase contrast is not expected to transmit information to the detector efficiently. The contrast transfer of low-spatial frequencies can be improved by increasing the  $\Delta f$ , but this will be done at the expense of the higher spatial frequencies. The amplitude contrast, on the other hand, has a maximum at small spatial frequencies and is thus expected to transmit the information from large objects with no limitations. By using a phase plate, the PCTF can be effectively modulated from sine to cosine form, which can improve the contrast of larger structures in LPEM without the need to use large values of  $\Delta f$  [66].

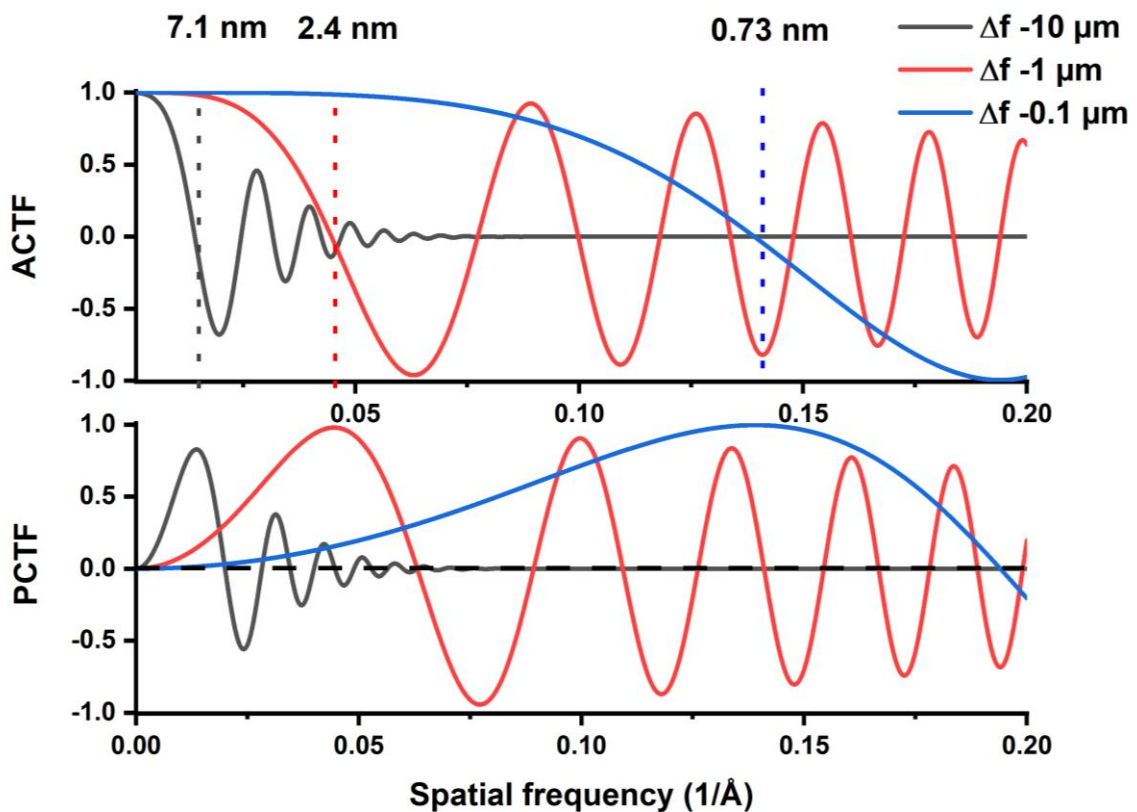


**Figure 1.5 Amplitude (ACTF) and phase contrast transfer functions (PCTF) plotted using the objective lens defocus ( $\Delta f$ ) -0.1, -1, and 10  $\mu\text{m}$ ,  $C_s = 0.5 \text{ mm}$ ,  $U = 200 \text{ keV}$ , and the spread of the illumination angle set to 0.1 mrad. The calculation is based on [74] and was done using the script provided in [72]. Vertical dotted lines indicate the lowest spatial frequency before the ACTF changes its sign, and PCTF reaches its maxima. Numbers are the corresponding lengths in real space in nanometers. For example, when  $\Delta f = -1 \mu\text{m}$ , the first maxima of the PCTF is located at the 2.4 nm indicating that the contrast for features larger than this will not be optimally transferred to the detector.**

An experimental approach for retrieving phase-information from thick, biological samples such as whole cells, has been presented by in [75, 76]. In short, a through focal series is acquired of the specimen, and a three-dimensional Fourier transform is created from the data. The method is interesting in the sense that it also accounts for the amplitude contrast that is found to affect mainly the lower spatial frequencies in images, as is expected, according to the CTF-theory (Fig. 1.5). The phase-related information present in 0.3-0.7 thick biological samples was retrieved. This indicates that even in thick specimens that are in the range of LPEM, there is some be phase-transmitted information present in

the images. However, it remains unclear in precisely which conditions phase contrast can give provide useful information in LPEM.

More detailed modeling of the exit wave function for thick and/or crystalline samples can be done by multi-slice simulations [77].

### **1.9.3 Fresnel-contrast**

Another effect of phase-contrast is the formation of so-called Fresnel-fringes. They appear on images of interfaces where abrupt changes in the projected mean inner potential are present, and the image is acquired out-of-focus. Fresnel-fringes are a result of near-field diffraction taking place in the vicinity of the sample. For the quantitative prediction of the observed fringes, numerical evaluation of the so-called Fresnel-propagator is required as no analytical solution exists to predict its effect on the image contrast of an interface [14, 78]. Computer simulations are used where the geometry of the edge is carefully considered [8]. In LPEM, the Fresnel-contrast has been used to image gas bubbles in a liquid cell [79], and it has also been observed when SiO<sub>2</sub>-nanoparticles were imaged in thinned layers of liquids [5]. An important unanswered question related to Fresnel-contrast remains if it can be useful for imaging low-Z material in LPEM.

### **1.10 LPEM: Challenges, methods, and insights**

LPEM has been used to study a number of systems from nucleation and assembly of nanoparticles [80] to the formation of protein crystals [81] and to the dynamics of colloidal particles[82] and distribution of labeled membrane proteins on whole cells [83]. Furthermore, advanced mixing techniques [23, 28], electrochemical [84], and thermal biasing [27] have been developed to initiate and sustain specific chemical processes in LPEM.

As important as are the novel insights from LPEM, so is the reproducibility of these results [85]. The greatest challenges for the reproducibility in LPEM are 1) the adverse effects of the electron beam and [86] 2) the confinement of structures and chemical reactions into a small volume of the liquid cell [25, 87, 88].

### **1.10.1 Sustaining reactions and processes in a liquid cell**

An exciting possibility of LPEM is to not just to study static structures but also to observe processes where nano-objects translate and interact with the liquid environment as they would in bulk liquid. Chemical or physical processes are driven by gradients such as in differences in concentration, temperature, or in the electrochemical potential. For such processes to be studied directly with LPEM, ideally, the same conditions should also be created inside the liquid cell.

By changing the concentration of chemical species in the liquid cell, several types of reaction conditions have been established. For example, to study the nucleation dynamics of calcium carbonate ( $\text{CaCO}_3$ ) [89], the tubing of the holder was used to mix  $\text{CaCl}_2$  and  $\text{NaCO}_3$  at the tip of the holder in order to initiate the crystallization that took place at the solid-liquid interface of the window. In another study, a three-step mixing method was introduced to induce phase-separation and micelle formation of amphiphilic block-copolymer (BcP) inside a nanofluidic device [24]. In this case, the driving force of the observed micelle formation was the induced concentration gradient of water and acetone: The nanochannel of the liquid cell was initially filled with a solution BcP in acetone. This was followed by the flow of water to fill the volume surrounding the liquid cell resulting in a diffusion gradient of water and acetone, which led to liquid-liquid phase separation of BcP in the imaging, which could be recorded in the TEM mode. Challenges, however, remain in accomplishing controlled mixing of two or more liquids in a nanofluidic device [23] as well as in changing the liquid on-demand in a liquid-filled device.

Chemical reactions can also be started and sustained by using other means than diffusion gradients. Increasing the temperature of the chemical system can lead to increased reaction dynamics [27], translational movements, and conformational changes in the secondary structures of molecules, such as proteins or thermoresponsive polymers [90]. Electrochemical biasing, on the other hand, can be used to study heterogeneous redox reactions taking place in a nanofluidic cell. For instance, this has allowed studying the structure-performance relationship in nanobatteries [84]. Finally, also the electron beam has been used as the driving bias for some specific reactions.

### 1.10.2 Electron beam damage vs. radiolytic biasing

The electron beam leads to the ionization of atoms and molecules in the specimen and can have a degrading effect on almost any type of sample. In addition to the radiolytic damage, the electron beam can lead to specimen heating, charging effects, and removal of atoms from the specimen surface [61]. For some systems, it has been suitable to define an acceptable cumulative electron dose or dose rate before the sample becomes too damaged [2].

The electron beam can be seen as a source of damage [61] but also a way to initiate and sustain chemical reactions by radiolytically biasing the sample [91]. Concentrations of primary radiolysis products from the electron beam-water interaction have been modeled, and [86] are dependent on electron dose rate, dissolved gases, organic molecules [92], and metal ions [93]. Typically, the irradiated liquid environment is reducing for the metallic ions, but the oxidation of organic molecules is expected to take place due to the high reactivity of hydroxyl radical [94]. In neat water, the simulations have shown that pH will reduce [86], but in the presence of, for example, Ce<sup>-</sup> ions, simulations, and experimental data have shown that the pH can also increase [95]. In order to make even qualitative predictions about the changes in the chemical environment of the liquid cell, a detailed simulation of the chemical conditions is thus needed [86].

The electron beam has been used to initiate the *irreversible* formation of structures deposits at the solid-liquid interface [96]. The formation of amphiphilic micelles was hypothesized to have been initiated by homolytic cleavage of the trithiocarbonate group, followed by the addition of a hydrophilic chain resulting in a block copolymer structure that undergoes a phase separation into micelles in water. The formation of micelles was induced by a continuous electron dose of  $0.5 \text{ e}^- \text{Å}^{-2} \text{s}^{-1}$ , and it was assumed that the contribution from radicals created from the radiolysis of water was negligible as long as sufficiently high monomer concentrations are used.

The electron beam can induce the movement of colloidal nanoparticles that have immobilized at the liquid-solid interphase of a liquid cell [87, 97]. The movement was

characterized as sub-diffusive as nanoparticles have strong interaction with the SiN<sub>x</sub>-membrane.

*Reversible* colloidal self-assembly of carboxyl-functionalized Au nanoprisms, spheres, and squares was initiated by using the electron beam at a continuous dose rate of 3.7 – 8.9 e<sup>-</sup>Å<sup>-2</sup>s<sup>-1</sup> in [98]. Optimization of the system required using a concentrated suspension of nanoparticles and optimization of the buffer conditions in order to prevent nanoparticles immobilizing at the liquid-solid interface and, on the other hand, to keep the system susceptible to self-assembly reaction under the beam. It was proposed that the leading cause of *reversible* organization was the increased ionic strength resulting from the charged radiolysis products.

These examples demonstrate the possibility to initiate and even control reactions of soft matter by using the electron beam. However, no complete understanding of the beam-induced chemistry has been offered in any of these cases. Careful control experiments are required to determine acceptable doses or dose rates and ensure that observed reactions are not due to irreversible beam damage, but due to the reversible biasing of the solution chemistry.

It has been demonstrated that the radiolytic effects of organic samples can be directly probed *post mortem* by applying methods such as infrared-spectroscopy [94] and mass-spectroscopy [99].

In the following papers from the field of LPEM will be highlighted to discuss how the main challenges, namely electron beam damage, and confinement have been overcome to gain insight from a specific system. Especially, the following questions will be focused on: 1) What specific insights about their subjects of study the LPEM has produced so far? 2) In the case of dynamic studies., how were reactions initiated and sustained in the liquid cell during the experiment? 3) What electron dose rates and cumulative values of  $D_e$  were used, and how were the effects of electron beam accounted for? Those items discussed here are by no means a complete list of publications from the field, as many of them have been selected from the field of soft matter science and biology [2].

### 1.10.3 Molecular assembly in soft matter systems

Several publications have focused on the self-assembly (S-A) of amphiphilic polymers on the solid-liquid interface of the liquid cells. [24, 96, 97, 99]. During the S-A, complex phenomena such as kinetic trapping can lead to a range of intermediate states which are of scientific and technological interest. Direct imaging of these transient structures could help to better understand and control the S-A process in such systems. In [24], the focus was on the initial stages of an S-A process of an amphiphilic block-co-polymer. The S-A was initiated by changing the solvent from acetone to water inside the liquid cell using a concentration gradient. Based on the image analysis and calculated theoretical phase-diagrams, it was proposed that liquid-liquid phase separation took place and resulted in a continuous membrane. In order to assess the beam-induced effects, a set of control experiments was conducted using a single electron dose rate of  $0.3 \text{ e}^{-}\text{\AA}^{-2}\text{s}^{-1}$ , which was also used for image acquisition. It was shown that when imaged over a time window of 1000s, the electron beam did not induce observable changes in the acetone, aqueous polymer solution, nor the pre-formed vesicles. It was also shown that the vesicles formed in the liquid cell with and without the beam had the same appearance.

The fusion and growth of pre-formed amphiphilic micelles were studied in [97]. Although the fusion process was directly visualized in LPEM, the resolution of the images was not enough to resolve the inner bi-continuous morphology of these micelles, which, however, was observed with cryo-EM. For more insight, molecular simulations were conducted, and they supported the idea that complex structures seen in cryo-EM may have formed as a result of the fusion-relaxation process of micelles. The electron dose rate used in the experiments was in the range of  $1.6\text{-}13.4 \text{ e}^{-}\text{\AA}^{-2}\text{s}^{-1}$  at which no damaging effects were observed. However, it was observed that at higher dose rates, the lateral slip-stick motion of micelles became faster, resulting in fusion events to occur more frequently.

These examples show how LPEM can be used to study molecular S-A to give insight into the structure and dynamics of the system. Latter case also exemplifies that if the spatial resolution in the LPEM experiment is not adequate, complementary techniques such as

cryo-EM [100] and molecular simulations [101] can be used to study some of the grand challenges in soft matter science.

For low-contrast materials, such as low-Z atomic number micelles, labeling may be required. The electron beam can also be used for *in situ* labeling of low atomic number materials in liquid. When bio-related, low-contrast vesicles were imaged in liquid cell TEM containing 100 mM NiCl<sub>2</sub> solution, vesicles obtained strong contrast under continuous illumination of  $D_e$  0.15-0.4 e<sup>-</sup>Å<sup>-2</sup>s<sup>-1</sup> [102]. When the electron beam was turned off and on again, the observed contrast faded, suggesting a reversible process where Ni<sup>2+</sup> deposits form and dissolve on vesicles.

#### **1.10.4 Imaging biomolecules**

The direct imaging of biomolecules, such as proteins and DNA, is of great interest to further elucidate the relationship between their structure and function. It is well known that biomolecules are susceptible to radiation damage, and it is expected that electron doses small as 0.1 e<sup>-</sup>Å<sup>-2</sup> are enough for protein inactivation [103].

The DNA hybridization has been studied indirectly by visualizing the assembly and diffusion of DNA-coated nanoparticles. When aggregates of DNA-coated AuNP's were studied in SiN<sub>x</sub>-cell and in a GLC [104], it was found that that superlattices stayed stable in GLC and graphene-coated SiN cell for several minutes when imaged with electron dose rates of 10-250 e<sup>-</sup>Å<sup>-2</sup>s<sup>-1</sup>. In bare SiN<sub>x</sub> cell, on the other hand, assemblies quickly degraded under the electron beam, and the conclusion was that GLC is able to scavenge highly reactive hydroxyl radical originating from the radiolysis of water. In another study, DNA-functionalized gold nanoparticles formed multimers [105] at the liquid-solid interface of a liquid cell. When the sample was irradiated with a continuous dose rate of 1.1 - 1.4 e<sup>-</sup>Å<sup>-2</sup>s<sup>-1</sup>, It was found that the interparticle distance did not change during minutes of imaging.

By loading complementary strands of short nucleotides into a GLC, it has been possible to directly image their hybridization and recognize some of the error-correction mechanisms that led to well-aligned strands [40]. When DNA oligomers were imaged in a GLC, their apparent hybridization reaction was not affected until a cumulative dose of 100-900 e<sup>-</sup>Å<sup>-2</sup>

was reached using an electron dose rate of  $2\text{-}10\text{ e}^{-}\text{\AA}^{-2}\text{s}^{-1}$ . This is a significant result as it suggests that the functionality of the biomolecule is preserved long enough so that its dynamics (here, hybridization of DNA) can be directly visualized. Also, some factors hindering the broader use of the method were highlighted. Preparing graphene liquid cells requires special skills from the operator, and there is no automated procedure existing. Secondly, the data-analysis is prone to subjective interpretations because the orientation of 3D-structures needs to be extracted from the 2D-projection by the microscopist.

The quaternary protein structures such as acrosomal bundles, microtubules (MT), and crystallization of catalase enzymes have been studied with LPEM. When acrosomal bundles and microtubules were loaded into a liquid cell consisting of 10 nm  $\text{SiN}_x$ -membranes, it was possible to image acrosomal bundles with a spatial resolution of 2.7 nm, which was determined by analyzing the Fast Fourier Transform (FFT) frequency spectrum of the acquired data [71]. Repeating spatial frequencies in FFT-diagrams are visible even if the point-to-point resolution of the image is limited by noise. This offers a convenient way to analyze the structural changes in real-space images without the need to extract the features of interest manually. When microtubules were loaded into the liquid cell, outlines of tubular structures were visible, but the quaternary structure was not resolved. In another study [39], a suspension of microtubules was loaded into a graphene liquid cell, and the quaternary structure was visualized up to the spatial frequency of  $0.2\text{ nm}^{-1}$  corresponding to the distance between protofilaments (5 nm). It was found that signal from protofilaments was preserved until cumulative electron doses of  $720\text{ e}^{-}\text{\AA}^{-2}$  were reached using an electron dose rate of  $11\text{ e}^{-}\text{\AA}^{-2}\text{s}^{-1}$ . In graphene-supported cryo-EM samples, the signal from protofilaments was visible only until  $100\text{ e}^{-}\text{\AA}^{-2}\text{s}^{-1}$  supporting the claim that graphene liquid cell and enclosure may mitigate some degrading effects of the electron beam.

When the nucleation and growth of orthorhombic protein crystals in supersaturated lysozyme solution [81] were studied in a liquid cell, it was possible to elucidate the crystallization process, which seemed to start from spherical particles that transformed into orthorhombic crystals. The nucleation of protein crystals was initiated in a

supersaturated lysozyme solution, and the crystal growth was maintained by a constant flow of solution of less supersaturation. It was found that the electron dose rate of  $3.2 \text{ e}^- \text{Å}^{-2} \text{s}^{-1}$  resulted in a similar growth rate as what was observed with an optical microscope and that no observable changes were found after an exposure of 1 minute. A magnitude of higher dose rate, on the other hand, resulted in the dissolution of the formed crystals.

### **1.10.5 Imaging colloidal dynamics**

The temporal and spatial resolution of LPEM allows the direct visualization of nanoparticle dynamics [106] and assembly [98] in liquid. LPEM could potentially be used to determine interaction potentials [82] between particles to reveal details about non-equilibrium phenomena in nanoscale where the theoretical frameworks such as Derjaguin-Landau-Verwey-Overbeek (DLVO) theory are struggling to give satisfactory predictions [101, 107]. The long-range interaction between individual nanoparticles is dependent on their effective charge, which can be tailored by surface functionalization and tuned, for example, by ionic strength and pH of the liquid medium. Short-range interactions include the attractive van der Waals forces and, for example, solvent effects [108]. Considering the achievable resolution of the LPEM, 10-100 nm inorganic colloidal nanoparticles are expected to be in the range of the SNR-limited resolution (Fig. 1.2) and thus an ideal target for dynamical studies.

Although an ideal candidate for dynamic studies, nanoparticle assembly imposes some experimental challenges for LPEM. First, it has been found that the movement of nanoparticles is slowed down in the vicinity of the membrane by several orders of magnitude compared to the Brownian-motion [106, 109]. Suggested causes for this observation are slip-stick motion induced by the beam-induced charging of the membrane [109], and an ordered water layer of high viscosity [106]. In addition, surface roughness and hydrodynamic drag near the membrane could also affect the observed motion. In any case, it can be difficult to translate findings into bulk conditions if observations of self-assembly are made under circumstances where the Brownian motion is strongly affected by the vicinity of the membrane [87]. On the other hand, freely diffusing nanoparticles are moving fast, and thus data can be affected by the motion blur [110].

When poly-ethylene glycol (PEG) functionalized, 30 nm diameter AuNP's were loaded into a liquid cell, it was found that many of them had adhered to the membrane. The electron beam, which was used for the imaging, facilitated the movement of the AuNP, and higher beam current lead to faster movement [109]. It was proposed that the movement of AuNP's resembled surface diffusion as opposed to free, Brownian motion. It was also proposed that beam-induced degradation of the PEG layer was the likely cause of the observed aggregation of particles, which led to the formation of chain-like and branched aggregates by monomer-chain addition and chain-chain addition after extended irradiation.

The interpretation of these results leads to important questions: Is it possible to observe nanoparticle motion in liquid without the effects of the membrane? Secondly, in which way the electron beam facilitates the movement of nanoparticles? And finally, how the electron beam damage on surface functionalization of NP's can be characterized?

When citrate-capped 150 nm diameter AuNP were studied in a  $\mu\text{m}$ -thick liquid cell filled with an aqueous solution, it was possible to record Brownian motion at that was found to be faster than observed in the optical microscope and predicted by the theory [110]. When the electron dose rate was increased from 0.25 to 3.7  $\text{e}^{-}\text{\AA}^{-2}\text{s}^{-1}$ , also the diffusion coefficient increased, suggesting that that electron beam facilitated the movement of freely diffusing AuNP's. The authors discussed several possible causes for this observation and concluded that the beam-induced generation of, e.g.,  $\text{H}^{+}$ , could create concentration gradients that lead to diffusiophoresis of freely diffusing colloidal particles.

It should be noted that increasing the electron does not always lead to faster motion of nanoparticles in LPEM. This has been observed for both for suppressed diffusion close to the membrane [106, 111] and for nanoparticles that are diffusing at rates predicted by the theory [112].

Finally, the interaction between colloidal particles depends significantly on their surface functionalization [7]. If the electron beam irreversibly changes the functionalization, self-assembled structures can disintegrate or merge together under the beam. The surface

functionalization has not been visualized directly in liquid due to its low contrast, which is due to the low thickness and high degree of hydration of the polymer coating. In order to evaluate the integrity of colloidal functionalization indirectly, the behavior of formed aggregates has been observed instead. The dose tolerance of functionalized Au nanoprisms was determined by assembling them first into stacks and then imaging the interplanar spacing using a range of electron dose rates [113]. Obtained data were compared with small-angle x-ray scattering (SAXS), where no electron beam-effects were present. It was proposed that the ligands covalently attached to Au-surface by thiol bonds withstand electron dose rates up to several hundred  $\text{e}^{-}\text{\AA}^{-2}\text{s}^{-1}$  before permanent damage took place. Based on their literature survey, the recommended experimental conditions for chemically biasing a colloidal system was in the range of 1-30  $\text{e}^{-}\text{\AA}^{-2}\text{s}^{-1}$ . It must be noted that the cumulative effect of reactive radiolysis products on the sample was neglected, and it was assumed that the observed shrinking of superstructures was completely due to the changes in the ionic strength, which was biased by the electron dose rate. This contradicts the understanding of the propagation of beam damage in organic material in ice and in vacuum [114]. Furthermore, no evidence was presented where *reversible* modulation of the lattice would have taken place.

### **1.11 Concluding remarks and the intended impact**

Based on the adapted theory of spatial resolution, some conclusions can be drawn from the expected capabilities of LPEM when imaging SiONP and PMS in a liquid cell. In Fig. 1.6A and B, the attainable resolution for DF-STEM for three materials is plotted as a function of  $D_e$  and  $t$ , respectively. Based on the theory, nanometer-resolution is expected only for the Au nano-objects if typical liquid cell thickness with  $t = 300$  nm is applied [5]. For amorphous  $\text{SiO}_2$ , a resolution of few tens of nanometers can be expected in similar conditions. Resolving between two adjacent 30 nm  $\text{SiO}_2$  nanoparticles (Rayleigh-criterion) thus seems feasible with electron doses of  $D_e = 1\text{-}10 \text{ e}^{-}\text{\AA}^{-2}$ . For  $\text{C}_8\text{H}_8$ , it is as well reasonable to expect that the nano-object of 100 nm can be resolved using  $D_e = 1\text{-}10 \text{ e}^{-}\text{\AA}^{-2}$ . As shown in Fig. 1.6B, the liquid thickness seems to have quite a limited effect on the attainable

resolution. Removal of the windows, on the other hand, may improve the resolution considerably more.

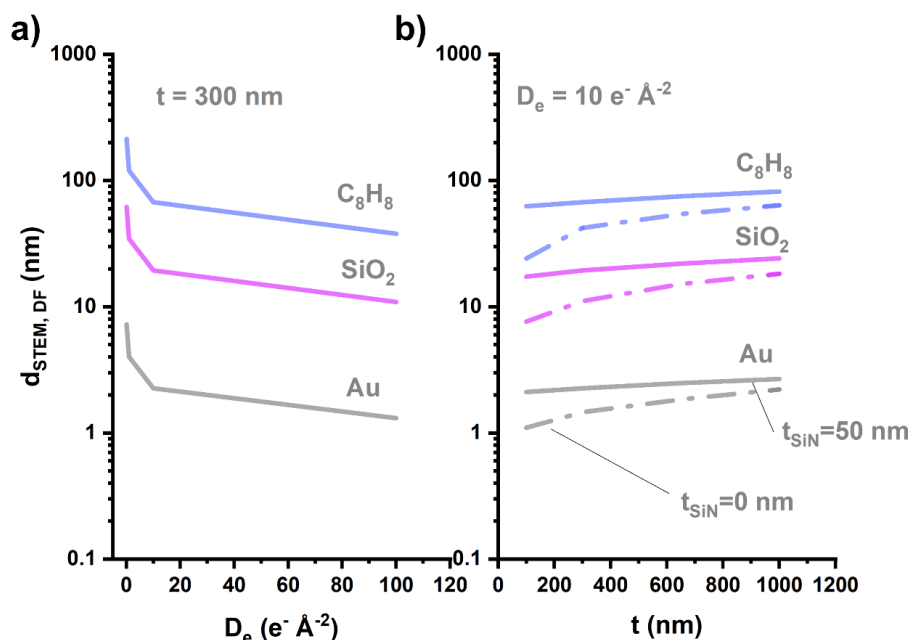


**Figure 1.6** The attainable resolution for DF-STEM when using optimized  $\beta$ . In A), the  $d$  vs.  $D_e$  is plotted for  $\text{C}_8\text{H}_8$ ,  $\text{SiO}_2$ , and Au to evaluate the performance of LPEM while using a liquid cell with  $t = 300 \text{ nm}$  B)  $d$  vs.  $t$  with  $t_{\text{SiN}} = 50$  or  $0 \text{ nm}$ ,  $D_e = 10 e^- \text{Å}^{-2}$ , and  $z = 0 \text{ nm}$ .

### 1.11.1 The scope and the intended impact of this thesis

Although several publications in the past have focused on imaging formation [85, 115], structure, and dynamics [106, 116, 117] of colloidal particles in a liquid cell, only in a few the formation of hierarchical, self-assembled structures have been studied [118, 119]. The scope of this thesis is to use LPEM to study the structure and dynamics of colloidal binary assemblies that form when 30 nm SiONP are mixed 100 PMS in suitable bulk conditions. It is expected that these hierarchical “binary particles” exhibit a raspberry-resembling structure in liquid [1]. The first goal is to attempt to visualize the morphology of these binary particles directly in a liquid (Chapter 4). The second goal is to use the flow capability of the liquid cell holder to initiate and record the self-assembly *in situ*.

Evidence has been presented in the literature that the “bypass” liquid cell design is not optimal for introducing colloidal samples in the imaging area when low spacer thicknesses are used [25]. Furthermore, the confinement may hinder the Brownian-motion of colloidal particles [87]. The effects of confinement on the dynamics and loading of colloids are, however, not fully understood, and thus of the mass-transport SiONP inside the liquid cell will be studied in Chapter 6 by directly comparing the formation of colloidal self-assembled monolayers in bulk and in confinement.

It would be important to find optimal imaging parameters and conditions that maximize the SNR in the obtained data. This is important for two reasons. When optimal parameters are used, the highest temporal resolution will be obtained as shorter exposure times (TEM) or pixel dwell times (STEM) can be used. Fast image acquisition will also minimize potential motion blur effects. Secondly, optimal imaging parameters may help to mitigate some of the electron beam-induced damage and effects. Organic and inorganic materials undergo irreversible changes due to the direct ionizing effects of the electron beam, and thus optimal imaging parameters will ideally minimize the required electron dose that is needed for image acquisition. Thus, it is necessary to first define an acceptable dose range and then establish a low-dose imaging protocol for imaging PMS, SiONP, and binary particles in the liquid (Chapter 4).

Analytical calculations presented in Chapter 1 are a straightforward way to evaluate the attainable resolution and optimal imaging parameters, such as the detector collection angle for nano-objects in liquid. Also, MC-simulations have been used to optimize imaging parameters and also to validate contrast in the experimental data [49, 112, 120]. However, *in silico* methods are expected to give results within a factor of two *at their best*, so validation is required against experimental data for this particular system.

The phase contrast enables a dose efficient way to create contrast in BF-TEM images for low-Z materials, but its use for imaging nanoparticles in a liquid cell is likely limited by the thickness of the sample and by the inefficient contrast transfer at low spatial frequencies corresponding to sizes of SiONP and PMS. Fresnel-contrast is another type of phase

contrast phenomenon which was shown to be present in thin liquid layers created by a novel pressure control system [5]. In this work, we would like to investigate if Fresnel-fringes can improve the low-dose performance of BF-TEM when imaging colloidal particles and their assemblies in a liquid cell (Chapter 5).

The intended impact of this thesis is thus two-fold: On the one hand, we are interested in directly visualizing the structure and dynamics of the colloidal self-assembly. In addition, the goal to develop LPEM as a method by finding ways to control several experimental variables that potentially undermine the reproducibility of obtained results.

To summarize, the following questions needed to be addressed to effectively apply LPEM for directly observing colloidal self-assembly into hierarchical structures:

- Can the hierarchical structure and dynamics of colloidal low-Z assemblies be visualized using liquid-phase STEM before the electron beam irreversibly damages the sample?
- How to define an acceptable electron dose for structural and dynamic studies in liquid?
- How well *in silico* methods agree with experimental data for PMS, SIONP, and binary particles?
- How can phase-contrast effects be utilized to improve the low-dose performance of BF-STEM when imaging colloidal particles and assemblies?
- How to initiate a colloidal assembly reaction in a liquid cell?
- In which way does the confinement of liquid cell hinder colloidal assembly compared to bulk?

### **1.12 A note about contributions**

**Professor Niels de Jonge has helped in planning and conducting the experimental work presented in this thesis. He has also helped in the writing process, and notably, Chapters**

**2-4 of the thesis are based on a joint manuscript that is planned for submission in the future.**

**Dr. Navina Dahmke helped with the German translation of the Summary on page 2.**

**The SiONPs were synthesized by Sebastian Rzakiewicz at the Eindhoven University of Technology (TU/e).**

**Pre-assembled binary particles were synthesized by Dr. Mohammad Moradi (TU/e).**

**The pressure control system used to control the thickness of the liquid cell in Chapter 5. has been developed by Dr. Sercan Keskin. Fig. 5.1 is by Dr. Sercan Keskin and has been reproduced with permission from [39].**

**The novel chip design tested in Chapter 6. is based on a patent of Prof. Niels de Jonge [6].**

## Chapter 2. Methods

### 2.1 Buffer and saline solutions

Phosphate buffered saline (PBS) with varying pH was prepared by mixing 1 M stock solutions, as reported in Table 2.1., then diluting to the final volume of 10 mL. The pH was determined with a digital pH meter (UltraBASIC, Denver Instruments, US). The 1 M stock solutions of NaCl (CELLPURE®, Carl ROTH, Germany) and NaH<sub>2</sub>PO<sub>4</sub> were prepared by dissolving each salt in high-performance liquid chromatography (HPLC) -grade water (ROTISOLV®, Carl ROTH, Germany). 1 M stock solutions of NaOH (Fluka, Germany) and HCl (AppliChem, Germany) were used as acquired. Saline was prepared by diluting 440 µL of 1 M NaCl stock solution with HPLC-water to a total volume of 10 mL.

### 2.2 Colloidal dispersions

Polystyrene microspheres (PMS) in aqueous solution were purchased from Sigma-Aldrich (LB1); their diameter was reported to be 110 nm with a standard deviation of 1.4 nm. The total solid content was reported to be 10%, containing 0.1% sodium azide functioning as a preservative and surfactant. Prior to use, PMS was diluted to a volume ratio of 1:100 with PBS buffer of pH 2 and shaken before use.

As outlined by Yokoi et al., silica nanoparticles were synthesized by dissolving 0.01 g of L-Lysine (Fluka, Germany) in 100 mL of distilled water and stirred with speed of 270 rounds per minute (RPM) under reflux at 60 °C [121]. To start the reaction, 6 mL of Tetraethylorthosilicate (TEOS) (VWR, US) was added and the mixture was left to react for 24 hours at 60 °C. Assuming all the TEOS reacted, the final concentration yield was 16.1 g/L for silica nanoparticles.

The surface of silica nanoparticles was amino-functionalized based on the protocol from [122]. The functionalization was accomplished with a 1:100 weight ratio of (3-aminopropyl)triethoxysilane (APTES) to the original amount of silica precursor (TEOS) used in the synthesis. The APTES was diluted to 4% (V/V) with tetrahydrofuran (THF), then the desired amount was pipetted into a stirring sample of silica dispersion, which continued for 30 minutes.

Amino-functionalized nanoparticles (SiONP) were diluted to a 1:5 volume ratio with PBS pH 2 and shaken before use. The  $\zeta$ -potential of 1:5 diluted SiONP was determined at pH values of 2, 7 and 12 and fixed ionic strength of 0.064 M. The measurement was done with Malvern Zetasizer instrument and three measurements on each sample were conducted. Average measured  $\zeta$ -potential values were 13 mV, -21 mV and -38 mV for pH 2, 7 and 12, respectively.

To prepare pre-assembled binary structures *ex-situ* in bulk solution, 0.16 mL of SiONP suspension and 0.02 mL PMS suspension (diluted 1:5 with HPLC-grade water) were added into 0.4 mL of 0.1 M KCL-HCL buffer of pH 1.6. The buffer was prepared by mixing 50 mL of 0.1 M KCl and 13 mL 0.1 M HCL, resulting in a final pH of 1.6.

### 2.3 Monte-Carlo simulations

Monte-Carlo (MC) simulations for both SiONP and PMS were performed with the Casino software [4]. A three-dimensional (3D) model of the liquid sample enclosed between silicon nitride (SiN) membranes was constructed (see Fig. 3.2). The sample parameters and the microscope settings used for the simulations are listed in Table 2.2. and Table 2.3 , respectively. The simulated data were exported from the software as 32-bit Tagged Image File Format (TIFF) and analyzed in ImageJ. Casino-files, including the sample geometry and simulation parameters, can be found in the Supplementary Information.

### 2.4 Numerically solved analytical calculations

Attainable resolutions were calculated using the theory adapted from [59]. Numerical calculation for Polystyrene (C<sub>8</sub>H<sub>8</sub>), amorphous silica (SiO<sub>2</sub>), and gold (Au) were performed in the Matlab-software in a similar manner as was done earlier for carbon and gold [59]. The sample parameters stated in the Table 2.2 were used.

Eq. 1.25 was solved numerically for the minimum  $d_{\text{SNR}}$  that satisfies the Rose-criterion for  $\text{SNR} \geq 3$ . The numerical solution was obtained by using the `vpasolve`-function in Matlab. The convergence angle for the electron beam in BF-TEM was set to 0.1 mrad. For BF- and DF-STEM-modes, the  $\alpha_p$  was adjusted along with the value  $\beta$ . For DF-STEM, the  $\alpha_p = 8$  mrad if  $\beta > 8$  mrad, and  $\alpha_p = \beta/2$  when  $\beta \leq 8$  mrad . For BF-STEM, the  $\alpha_p = 8$  mrad when  $\beta < 8$

mrad and  $\alpha_p = \beta$  when  $\beta \leq 8$  mrad. The inelastic scattering was included in calculations unless otherwise stated. For polystyrene, the numerically solved value of  $d_{snr}$  was negative for  $\alpha, \beta \gtrsim 10$  mrad due to the inversion of the contrast between the nano-object and the liquid background. For these values, the  $|d_{snr}|$  was plotted instead.

The SNR vs.  $D_e$  for PMS and SiONP in a liquid cell was calculated in separate scripts using calculated mean-free path lengths and then using Eq. 1.23-Eq. 1.25 and Eq. 1.29.

The Matlab-scripts can be found in the Supplementary Information.

## 2.5 Scanning transmission electron microscopy

Scanning transmission electron microscopy (STEM) was conducted using a probe corrected transmission electron microscope (ARM200CF, JEOL, Japan) at 200 keV beam energy. For STEM, the pixel dwell time was in the range of  $\tau = 1\text{-}20 \mu\text{s}$ , and pixel size was in the range of  $l = 3.3\text{-}3.8$  nm, corresponding to the nominal magnification of the microscope of 60 kx and 50 kx, respectively. The annular darkfield detector collection angle was set either to  $\beta_{in} - \beta_{out} = 27\text{-}110, 54\text{-}220$  or  $68\text{-}280$  mrad. The probe convergence angle amounted to 13.4 mrad when a 20  $\mu\text{m}$  condenser lens aperture was used. A spot size of 4C was selected so that the probe current ( $I_p$ ) was 81 pA. The probe current,  $I_p$ , was measured by directly imaging the probe with the camera (Ultrascan 1000XP, Gatan, Ca, USA) for which the conversion factor (9.9 counts/ $e^-$ ) was determined with the built-in picoamperometer of the fluorescent screen. (See appendix I for more details) The error of the beam current measurement was estimated to be  $\pm 10\%$ . To calculate the total electron dose,  $D_e$ , deposited per areal unit (A) per frame, the following equation was used:

$$D_e = \frac{I_p * 6.24 * 10^{18} e^-}{s^2 * \tau} \quad (\text{Eq. 2.1})$$

The typical  $D_e$  used for STEM imaging in the liquid was in the range of 0.5 and 5.0  $e^- \text{\AA}^{-2}$  per frame, and typically a sequence of 20-100 frames was acquired from the same area.

## 2.6 Transmission electron microscopy

Transmission electron microscopy was done with a JEOL ARM200CF microscope (JEOL, Japan). The camera (Ultrascan 1000XP) was operated with a binning of 1 and an image size of  $2048 \times 2048$  pixels. In the case of PMS immobilized on the window under atmospheric conditions, the sample was imaged with a spot size of 4, and a  $50 \mu\text{m}$  condenser lens aperture (CLA). This results in an electron flux of  $0.67 \text{ e}^{-}\text{\AA}^{-2}\text{s}^{-1}$ , with an  $l$  of  $1.7 \text{ nm}$ . A pre-specimen shutter was used to acquire a stack of 40 images with an effective exposure of time  $0.94 \text{ s}$  per frame. To image SiONP immobilized on the window, a spot size of 4C and a  $50 \mu\text{m}$  CLA with an objective lens aperture (OLA) of  $60 \mu\text{m}$  were used. The  $s$  was  $0.48 \text{ nm}$ , resulting in an electron flux of  $6.3 \text{ e}^{-}\text{\AA}^{-2}\text{s}^{-1}$ . For imaging pre-formed binary particles in the liquid, a spot size of 1 C with  $50 \mu\text{m}$  CLA, and  $s = 1.61 \text{ nm}$  were used, resulting in an electron flux of  $2.8 \text{ e}^{-}\text{\AA}^{-2}\text{s}^{-1}$ . Also, the  $60 \mu\text{m}$  ( $32 \text{ mrad}$ ) OLA was inserted, and a stack of 10 images was acquired using an effective exposure time of  $1.00 \text{ s}$  per frame.

## 2.7 Scanning electron microscopy

Scanning electron microscopy was conducted with FEI Quanta 250 FEG -microscope (Thermo Fischer, USA) operated at  $20 \text{ keV}$  and in High Vacuum-mode. Images were captured at magnifications of  $400\text{-}80\,000$ , the working distance of  $3\text{-}5 \text{ mm}$ , a pixel dwell time of  $5\text{-}20 \mu\text{s}$ , a condenser lens aperture size of  $30 \mu\text{m}$ , and a beam current of  $0.1 \text{ nA}$ .

## 2.8 Liquid-phase electron microscopy

LPEM- experiments were performed with a dedicated liquid cell specimen holder (Ocean, DENSSolutions, Netherlands). Prior to experiments, the system was cleaned by flushing it with  $200\text{-}400 \mu\text{L}$  of HPLC-grade ethanol, followed by HPLC-water and an injection of air to remove most of the liquid. O-rings were removed, and the holder tip was scrubbed with an HPLC-grade ethanol-soaked, lint-free tissue using pointy tweezers. The O-rings and the holder tip were sonicated for 2 minutes in  $50 \text{ mL}$  of HPLC-grade ethanol- and HPLC-grade water. The tip was blow-dried with a stream of argon, and vacuum grease was applied on the O-rings to secure the tightness of the cell. In order to remove the photoresist from the silicon nitride ( $\text{Si}_3\text{N}_4$ )-windows (DENSSolutions, Netherlands) the windows were cleaned by

gently swirling in 50 mL of HPLC-grade acetone and HPLC-grade ethanol, respectively. After this, the chips were plasma-cleaned for 5 minutes with a power of 50 W in Ar/O<sub>2</sub>-mixture (75%/25%) in a chamber that was first evacuated to a vacuum of 70 mTorr. (Solaris, GATAN, US). In order to maintain control over the liquid thickness,  $t$ , and protect the sample from compression during the loading, a 200 nm –spacer was used on the bottom chip.

A monolayer of SiONP was deposited on the top window (no spacer) by first firmly pressing the vacuum-facing side of the chip against the surface of a gel box and pipetting 0.5  $\mu$ L of dispersion SiONP on it. After 1-2 minutes of incubation time, the chip was washed 3-5 times with 500  $\mu$ L of water and blotted dry on a lint-free tissue.

A monolayer of PMS was prepared in a similar way, but only a small  $\sim$  0.1  $\mu$ L droplet was applied on the window area, and after 30-60 s, the whole chip was rinsed in a 50 mL bath of HPLC-water. After blotting the vacuum side of the chip, a small droplet of water resided on the window area, and the liquid cell was assembled and sealed immediately to prevent the PMS from drying. In order to observe air-dried PMS, the small drop of residual water dried for 2-3 minutes before cell assembly.

## **2.9 Elemental analysis with EDX and EELS**

JEOL ARM200F equipped with an EDX detector (JEOL) and an energy filter (GATAN) was used for the elemental analysis. For EDX, a spectrum image with a size of 64 by 64 pixels was collected using a probe current of 1.2 nA and a pixel dwell time of 200  $\mu$ s. For the collection of EELS spectrum image of size 26 by 32 pixels was recorded using a pixel size of 3.7 nm pixel, and  $\tau = 0.1$ s. The energy dispersion of the spectrometer was set to 0.25 eV/channel, and the elemental maps were collected in the energy-loss range of 881-1293 eV. The data processing and analysis for EDX mapping were conducted with JEOL Analysis Station v.3.8.0.34. Elemental peaks were identified, and their areas integrated in an automatic manner to produce the elemental maps presented here. For the EELS-mapping, Gatan Digital Micrograph v2.1.1- software equipped with EELS Analysis-plugin v2.1.1 was used for the background subtraction and the production of elemental maps. In short, the

appropriate pre-edge area was manually chosen so that the real-time fit of the Power-law background model fitted well the pre-edge background based on the visual inspection.

## 2.10 Measurement of liquid thickness

To determine the presence of the liquid and measure its thickness, electron energy loss spectroscopy (EELS) was used (See also Appendix II). In the case where the total relative sample thickness ( $t/\lambda$ ) was less than 5 times the inelastic mean free path length (IMFP), the absolute sample thickness ( $t$ ) was determined by the EELS log-ratio technique. To calculate the absolute  $t$ , the “effective atomic number”-method [123] was used to determine  $\lambda$  for  $\text{Si}_3\text{N}_4$  ( $\lambda_{\text{Si}_3\text{N}_4} = 136 \text{ nm}$ ) and water ( $\lambda_{\text{water}} = 175 \text{ nm}$ ). Settings used for the acquisition of the EEL spectra were  $\alpha = 13.4 \text{ mrad}$ , EELS acceptance semi-angle of  $20.8 \text{ mrad}$ , and a spectrometer dispersion of  $0.5 \text{ eV/channel}$ . This allows electrons to be effectively collected up to the electron energy loss of  $860 \text{ eV}$ . Using the line scan tool of the scan-control software (Digital Micrograph-3, Gatan, CA, USA), EELS spectra were collected across the field of view. The built-in function of the software was used to calculate  $t/\lambda$ . To finally obtain  $t$  of the liquid ( $t_{\text{water}}$ ), the contribution of windows was subtracted as was done in [124]:

$$t_{\text{water}} = \left( \frac{t}{\lambda_{\text{EELS}}} - \frac{t_{\text{Si}_3\text{N}_4}}{\lambda_{\text{Si}_3\text{N}_4}} \right) \times \lambda_{\text{water}} \quad (\text{Eq. 2.2})$$

The accuracy of this calculation is estimated to be  $\pm 20\%$ [123], whereby the main source of error is the estimation of  $\lambda$ . It should be noted that recently the inelastic mean free pathlength of liquid water was measured by using electron holography in a liquid cell for  $120 \text{ kV}$  and  $300 \text{ kV}$  acceleration voltage and was found to be nearly  $40 \%$  higher [125] than what was predicted by the model used in this work.

## 2.11 Image analysis

The Fiji distribution of ImageJ-software (v. 1.52i), National Institute of Health, USA) was used for image analysis in combination with graph plotting and statistical analysis software (Prism v. 7.03, GraphPad, San Diego, US). Simulated image data was analyzed by measuring the intensity and standard deviation values of the image signal from the

different parts of images (PMS, SiONP, and background), as indicated in Fig. 3.1A,B and Fig. 3.2C. The drift present in the experimental data was removed by using CVmatch Template ImageJ-plugin. In more detail, a 100-300 pixel diameter square was drawn around a bright feature (eg. Salt deposit in the window), and subsequent frames were aligned relative to each other. The “Rigid”-model was used in order to avoid aliasing effects as it translates frames only in x- and y- direction and uses one-pixel steps. In some cases, no suitable high-contrast features were present in the field of view, and low contrast features of interest were not correctly recognized by the automatic alignment algorithm. A manual alignment tool included in the TrackEM2-plugin of ImageJ was used to solve this issue. In order to align a stack, landmarks were manually placed on a feature (eg. SiONP on the window) that was intended to stay stationary in the image sequence. Next, the algorithm aligned the stack based on the location of landmarks using the “Rigid”-model and one-pixel step length.

To improve the SNR in a sequence of images, a running average was created from the aligned stack of images. For this, we used a custom-made script for ImageJ that averaged a given number of successive images in a stack.

## **2.12 Inductively coupled plasma atomic emission spectroscopy (ICP-AES)**

The use of an ICP-AE spectrometer (Horiba Jobin Yvon Ultima, Japan) allowed for the screening of the PBS and SiONP suspension for copper contamination. The liquid was fed to the nozzle at a pressure of 2.5 bar, resulting in a flow rate of 0.82 l/min. The reported detection limit for copper is 0.00162 mg/L.

Solution	NaH <sub>2</sub> PO <sub>4</sub> μl	NaOH μl	HCl μl	NaCl μl
Saline	-	-	-	440
PBS pH=2	100	-	120	470
PBS pH=7	100	50	-	440
PBS pH=12	100	320	-	-

**Table 2.1** Amounts of 1M stock solutions mixed to prepare 0.01 M phosphate-buffered saline (PBS) with a total volume of 10 ml.

Component in liquid cell	Elemental composition	<i>d</i> [nm]	<i>ρ</i> [kg/m <sup>3</sup> ]	<i>t</i> (nm)
Water	H <sub>2</sub> O	-	1.0	110, 300, 500, 800
Window	Si <sub>3</sub> N <sub>4</sub>	-	3.17	50
SiONP	SiO <sub>2</sub>	30	1.64	-
PMS	C <sub>8</sub> H <sub>8</sub>	100	1.05	-

**Table 2.2** Physical-chemical parameters of the simulated liquid cell, where *d* is the particle diameter, *ρ* is the density, and *t* is the thickness. The density of the polystyrene microsphere (PMS) was acquired from the supplier (Sigma Aldrich), and the estimated density of SiONPs was based on analytical ultracentrifugation [126].

Parameter	Values
$\alpha_p$ (mrad)	7.1 13.4
$\theta_{in} - \theta_{out}$ (mrad)	0-9 0-15 0-27 27-110 54 - 220 68 - 280
$d$	0.1 nm
$s$	3.7 nm
$N$	961 2883 8649 25947

**Table 2.3 Microscope settings used for the Monte Carlo (MC) simulations**, where  $\alpha$  is the convergence angle of the electron probe,  $\theta_{in}$  and  $\theta_{out}$  are the inner and outer collection angles of the annular darkfield detector, respectively,  $d$  is the probe size,  $s$  is the pixel size, and  $N$  is the number of electrons per pixel used to simulate the image. Total- and partial elastic electron scattering cross-sections were based on the values calculated with the ELSEPA-method as provided by the National Institute of Standards and Technology (NIST) database[127].

## Chapter 3. Optimization of STEM parameters *in silico*

*“How to optimize the image quality in liquid-phase STEM by using Monte Carlo-simulations?”*

### 3.1 Introduction

In order to maximize the amount of data obtained from an experiment involving beam-sensitive material, it is helpful to optimize the imaging parameters of the microscope [120]. Optimal imaging settings for imaging low-atomic number material in liquid, ice, and related systems have been discussed in [32, 53, 59, 120, 128].

Our goal is to use Casino-software for estimating the image formation in liquid samples and to optimize a liquid-phase electron microscopic system to visualize self-assembled structures. These structures consist of oppositely charged, 30 nm diameter, amino-functionalized silica nanoparticles (SiONP) that spontaneously form a shell around 100 nm diameter, negatively charged polystyrene microspheres (PMS) [1]. PMS is a polymeric material whose structure is affected by the electron beam [114, 129]. SiO<sub>2</sub>-nanoparticles have been found to change shape [130] and agglomerate [131] under the electron beam.

The Monte-Carlo method will be used in this work to simulate the image data of SiONP, PMS, and binary structures in liquid. The computational procedure for modeling the interaction of the sample with the beam is different than what was presented in Chapter 1.

#### 3.1.1 Monte-Carlo simulations for STEM

In this work, the optimization for STEM was accomplished *in silico* by using the Monte Carlo method (MC) built in the CASINO -software that is freely available for download and use. MC-simulations are suitable for modeling the interaction between the electron beam and the sample. Monte Carlo-approach models the interaction as a “true single-scattering”- approach where the incident electrons are elastically scattered along the

trajectory penetrating the sample [132]. First applications of the MC-approach were used to study the propagation and production of neutrons in fissile material in Los Alamos lab, USA [133].

The Casino- software can simulate the formation of STEM images in samples of any composition and geometry. The simulation of the scanning is done by adjusting the position of the conical electron probe in three dimensions (x,y,z) hence also allows the effects of defocus ( $\Delta f$ ) to be investigated. The detector settings can be adjusted to emulate the effects of BF / DF-detector characterized by the inner and outer acceptance angles  $\beta_{in}$  and  $\beta_{out}$ , respectively. The software can also simulate the noise characteristics of the electron source and the convergence angle ( $\alpha_p$ ) of the electron probe. This enables realistic simulation of image formation in STEM.

### 3.1.2 Physical models used in the Casino-software

In the Casino-software, the MC-method is used in several stages to model the collision behavior of the incident electrons with the sample material [3]. For example, the distance that the incident electrons travel between two successive elastic collisions ( $L$ ) is given by Eq. 3.1:

$$L = -l_{el} \cdot \log(R) \quad (\text{Eq. 3.1})$$

Where  $R$  is a random number between 0-1 and  $l_{el}$  is the elastic mean-free path length for a compound consisting of  $n$  elements:

$$l_{el} = \frac{1}{\rho \cdot N_0 \cdot \sum_{i=1}^n \frac{C_i \cdot \sigma_{el}^i}{A_i}} \quad (\text{Eq. 3.2})$$

Where  $N_0$  is Avogadro's number,  $\rho$  is the mass density of the compound and  $C_i$ ,  $\sigma_{el}^i$ ,  $A_i$  are mass-fraction, total elastic cross-section, and atomic mass of the element  $i$ , respectively. The physical model used in this work for calculating the  $\sigma_{el}$  is based on the ELSEPA-method presented in [62] and values for all chemical elements in the electron energy range of 100 -300 keV were tabulated in the Casino-software.

After each elastic collision, the electron trajectory changes relative to the original trajectory and is defined by the azimuthal angle  $\varphi$  and the polar angle  $\theta$ . As  $\varphi$  is distributed uniformly, it is defined by

$$\varphi = R \cdot 2\pi \quad (\text{Eq. 3.3})$$

In order to solve the polar angle  $\theta$  for a given R, the following equation is used

$$R = \frac{\int_0^\theta \frac{d\sigma}{d\theta} \sin(\theta) d\theta}{\int_0^\pi \frac{d\sigma}{d\theta} \sin(\theta) d\theta} \quad (\text{Eq. 3.4})$$

, and tabulated values for  $\theta$  vs. R are provided by the software.

The inelastic interaction causes only small deviations in the scattering angle and was omitted in this model [134]. However, as is illustrated in Fig. 1.4 omitting inelastic scattering may affect the evaluation of SNR-limited resolution for small values of  $\theta$ .

The energy loss of each electron ( $\Delta E$ ) is calculated by the following equation

$$\Delta E = \frac{dE}{ds} \cdot L \quad (\text{Eq. 3.5})$$

Where  $\frac{dE}{ds}$  is the rate of energy loss calculated as a continuous electron energy loss function [135].

### 3.1.3 Determination of SNR in image data

In this work, we are interested in studying the structure of colloidal binary particles with optimized imaging parameters. To reliably determine the effects of imaging parameters and sample properties to the resulting image quality, a well-defined yet straightforward method was required to directly determine the signal-to-noise-ratio (SNR) of nano-objects in simulated and experimental STEM images. Demers et al. used a method based on a line-scan over an object in an image to evaluate the strength of the signal compared to the background intensity and noise level [136]. Ideally, this approach would be extended to be more suitable for evaluating several particles in an image without the need to manually plot and manipulate the profile plot.

After the method to quantify the SNR from the images has been accomplished, two main goals exist. The first is to use the MC-simulations to predict the appearance and SNR of SiONP, PMS, and binary structure in the image data. Secondly, optimal imaging parameters will be estimated and then compared with the theoretical model adapted from [59]. The results for the selected parameter will be compared to experimental data in Chapter 4.

## **3.2.Results**

### **3.2.1 Measuring SNR from experimental and simulated image data**

In order to compare the effects of electron dose on the SNR of particles, the particles were deliberately immobilized on the window to remove the blurring effect caused by their movement. Representative datasets encountered in this work, see Fig. 3.1A and B, where layers of PMS and SiONP have been immobilized on the top windows, respectively. The liquid cell was sealed and inserted into the microscope. After confirming the presence of particles on the top window, the liquid was flowed in, and the images were acquired, and the liquid thickness was determined using by using EELS. For SiONP, the liquid thickness amounted to 350 nm. In order to define the spatial width of the signal for both PMS and SiONP, profile plots were first extracted from the data, and then the full width at half maximum (FWHM) was manually measured, as shown in Fig. 3.1C and D. For PMS, the FWHM was measured to be 60 nm and for SiONP 15 nm.

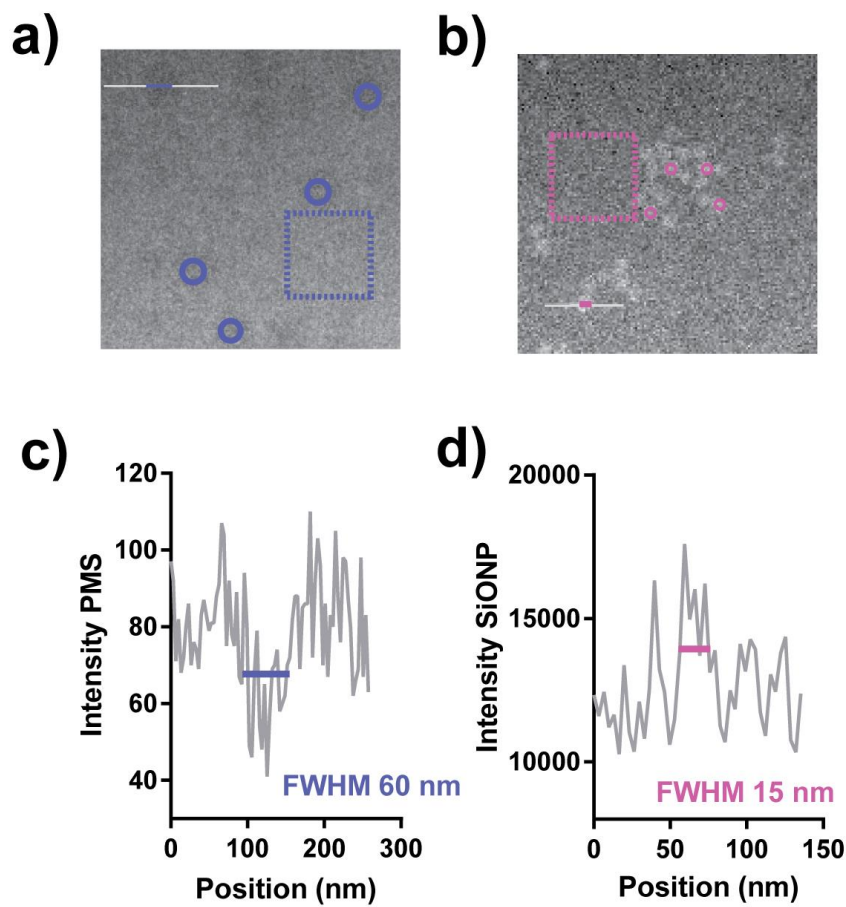


**Figure 3.1 Defining the signal in experimental image data.** In A), polystyrene microspheres (PMS) immobilized on the upper window were imaged using  $D_e = 21 \text{ e} \text{ \AA}^{-2}$ . The average relative thickness ( $t/\lambda$ ) across the field of view was measured to amount to 4.43, corresponding to  $t = 650 \text{ nm}$  after subtracting the contribution of windows (Eq. 2.2). In B), some silica nanoparticles (SiONP) are imaged in a 350 nm thick liquid layer using  $D_e = 23 \text{ e} \text{ \AA}^{-2}$ . Profile plots in C) and D) over single particles indicate that the full width at half maximum (FWHM) of signal ( $S_L$ ) is 60 nm and 15 nm for PMS and SiONP, respectively. Areas of corresponding circular ROIs for  $s = 3.3$  nm are 256 px and 21 px, respectively. In order to measure the mean intensity ( $S_B$ ) and standard deviation ( $\sigma_B$ ) of the background, irregular area(s) between nano-objects were selected.

### 3.2.2 Signal-to-noise-ratio of multi-pixel objects

A key question to address is how the SNR can be used to quantitatively determine how well a multi-pixel object was visible, from which the experimental resolution in the image would be evaluated. The signal-to-noise-ratio for an arbitrary signal is defined as:

$$SNR = \frac{S}{\sigma} \quad (\text{Eq. 3.6})$$

, where  $S$  is the signal, and  $\sigma$  is the standard deviation representing the level of noise in the signal.

Images are 2D arrays of pixels, where each pixel represents the strength of the signal on a lateral scale. Considering an image containing a single-pixel object, the signal  $S_O$  is surrounded by a noisy background of mean intensity of  $\bar{S}_B$ . The SNR is given by:

$$SNR_O = \frac{S_O - \bar{S}_B}{\sigma_B}, \quad (\text{Eq. 3.7})$$

, where the  $\sigma_B$  is the standard deviation of the background signal.

In practical imaging, objects occupy multiple pixels and are often called “*lesions*” [137] in biomedical applications. The average SNR of a pixel in a lesion consisting of  $n$  pixels is

$$\overline{SNR}_L = \frac{\bar{S}_L - \bar{S}_B}{\sqrt{\sigma_L^2 + \sigma_B^2}} \quad (\text{Eq. 3.8})$$

In case of a high background level comparable to the signal level, which is typically the case in liquid-phase electron microscopy, it can be assumed that  $\sigma_L = \sigma_B$ , so that

$$\overline{SNR}_L = \frac{\bar{S}_L - \bar{S}_B}{\sigma_B \sqrt{2}} \quad (\text{Eq. 3.9})$$

In order to measure  $\bar{S}_L$ , directly from the image data, we used circular regions of interest (ROI) that had the diameter of the FWHM determined above. (Figure 3.1A and B) The FWHM has been experimentally shown to depend on the noise level of the image [138]. Hence our decision to define the width of the signal using these images is more or less arbitrary.

$\bar{S}_B$ , and  $\sigma_B$  were measured from irregular areas where no particles are present, and that represents approximately the same  $t$  where the  $\bar{S}_L$  was measured (dashed line in Figure 1A and B).

As we are working with images, it is useful to distinguish between the case of a single-pixel object or a multiple-pixel object, also termed lesion, being visible in an image. The Rose criterion [63] states that for a single pixel object to be visible from the background, its minimum SNR should be 3-5. For a lesion to be visible, the average  $\overline{SNR}_L$  can be smaller; this is because the statistical chance to observe a number of adjacent pixels with a slightly different signal than the background makes the lesion observable, even though the SNR of an individual pixel would be too low to recognize. So, an effective  $SNR$  for an object that will express the visibility of a multi-pixel object similar to the Rose criterion must be defined.

$$SNR_L^* = \frac{\bar{S}_L - \bar{S}_B}{\bar{\sigma}_B \sqrt{2}} \quad (\text{Eq. 3.10})$$

To derive the relation between  $SNR_L^*$  and  $\overline{SNR}_L$ , a binning operation is used to transform the multi-pixel object into a single-pixel object as described in the following. During the operation,  $\bar{S}_L$  and  $\bar{S}_B$  will stay constant, but  $\bar{\sigma}_B$  will decrease as the whole image is averaged over  $n$  pixels. Note that variance is the square of the standard deviation:

$$Var(S_B) = \sigma_B^2 \quad (\text{Eq. 3.11})$$

During the binning operation, the average over the several pixels and the mean-variance of  $S_B$  is:

$$Var(S_B)^{mean} = Var\left(\frac{1}{n} \sum_{i=1}^n S_{B,i}\right) \quad (\text{Eq. 3.12})$$

If it is assumed that each  $S_{B,i}$  is a truly random variable (random noise) such that the covariance of any two pixels equals zero and that the variance between each pixel is equal (Bienaymé-formula), the following holds true:

$$\sqrt{Var(S_B)^{mean}} = \sqrt{\frac{1}{n} Var(S_B)} \quad (\text{Eq. 3.13})$$

which equals:

$$\bar{\sigma}_B = \frac{1}{\sqrt{n}} \sigma_B \quad (\text{Eq. 3.14})$$

Substitution into Eq. 3.7 yields:

$$SNR_L^* = \frac{\bar{S}_L - \bar{S}_B}{\sigma_B \sqrt{2}} \sqrt{n} = \overline{SNR}_L \sqrt{n} \quad (\text{Eq. 3.15})$$

In terms of visibility of an object according to the Rose criterion, the following stands:

$$SNR_L^* \geq 3 \quad (\text{Eq. 3.16})$$

### 3.2.3 SNR and statistical estimation of the experimental resolution

Eq. 3.15 is not only useful for describing the visibility of a multi-pixel object by referring to the Rose criterion, but it can also be used to estimate the experimental resolution,  $d$ , defined as the smallest object that can be observed in the image [59, 136]. This resolution differs from the usual definition of resolution based on electron optics, which is typically limited by lens aberrations [8]. The experimental resolution calculated here is limited by the achieved SNR, which is determined by the  $D_e$  and the scattering properties of the sample. In case of optimal conditions, when a maximal dose is available, a pixel of size  $s$  relates to the resolution as  $2s = d$ . This follows the Nyquist sampling criterion stating that the sampling should be at least twice the spatial frequency; therefore, 2 pixels are needed to resolve a spatial feature of size,  $d$ . However, in practice, the available  $D_e$  before radiation damage occurs limits the  $SNR$ . Thus, there may be a situation where an object spanning multiple pixels is barely visible within the fluctuations of the background. This leads to the question of what size object can still be resolved with sufficient SNR. For this calculation, assume the area  $A$  of the lesion  $L$  to be of round shape so that  $A = \pi(d/2)^2$ . It is also known that  $A = n l^2$ . Hence, it can be written that  $n = \left(\frac{d}{l}\right)^2$ . Substitution into Eq. 3.15 results in:

$$\frac{d}{l\sqrt{2}} = \frac{SNR_L^*}{\overline{SNR}_L} \quad , \quad \text{with } d \geq 2s \quad (\text{Eq. 3.17})$$

Now, if the Rose criterion is applied by setting  $SNR_L^* = 3$  and the size of the smallest resolvable rectangle is solved, the result is:

$$d = \frac{3\sqrt{2}}{\overline{SNR}_L} s \quad (\text{Eq. 3.18})$$

With this relation, the measured  $\overline{SNR}_L$  can be directly transformed to the experimental resolution as a function of the  $s$ .

### 3.2.4 Investigation of MC-simulated image data

To support the optimization of our STEM parameters, MC- simulations were conducted with the Casino-software package [4, 139]. An example of the physical 3D-model is presented in Figure 3.2A. The topic of interest was how variations in the BF and DF collection angle, the probe convergence angle, the  $D_e$ , and  $t$  affect the visibility,  $SNR_L^*$  (Eq. 3.15), and resolution (Eq. 3.18) of low-Z nano-objects in liquid. The simulation was run by using parameters presented in Table 2.2 and Table 2.3. The Resulting 32-bit images of size 120 by 107 pixels were cropped, downsampled to 8-bit, and normalized so that they could be presented with comparable average intensity levels, as shown in Fig. 3.2B. The normalization was done with the “Enhance Contrast” -function in ImageJ, so that 0.3% of the pixels were let to become oversaturated.

Visual inspection of the data indicates that increasing  $D_e$  and decreasing  $t$  consistently improved the visibility of simulated nano-objects. In the case of SiONP, the  $D_e = 2.1 \text{ e}\text{-}\text{\AA}^{-2}$  is enough to resolve the object from the background for most of the tested settings and liquid thicknesses. PMS shows an inversion of contrast at low values of  $\beta$ , as was predicted by the analytical model (Fig. 1.1 and 1.2).

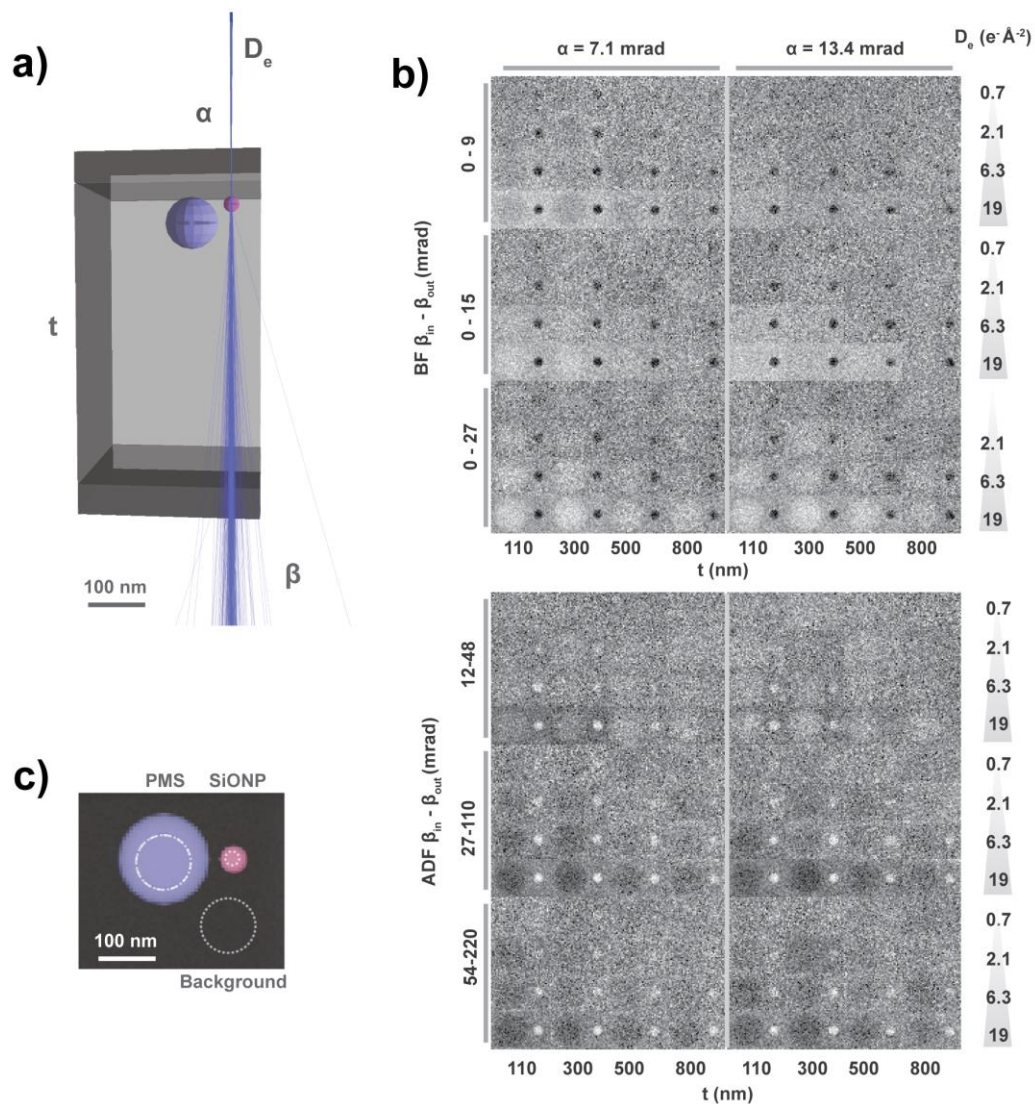


**Figure 3.2. Simulation of liquid cell STEM in Casino-software.** In A) is a screen capture of the side view of the modeled liquid cell in Casino-software. A 100 nm diameter polystyrene microsphere (PMS) particle and 30 nm diameter silica nanoparticle (SiONP) are placed at the upper membrane with thickness ( $t_{SiN}$ ) of 50 nm. The liquid thickness ( $t$ ) was set to 500 nm, and in blue are shown trajectories of 24947 simulated electrons that correspond to electron dose ( $D_e$ ) of  $19 e \cdot \text{\AA}^{-2}$  for the pixel size ( $s$ ) of 3.7 nm. In B) is shown the simulated image data for a total of 192 tested combinations for brightfield (BF) and darkfield (ADF) detector settings ( $\beta_{in} - \beta_{out}$ ). PMS is located on the left side of each sub-panel, and SiONP is located on the right side. In C) is illustrated the ROIs that were used to measure the signal intensity  $\bar{S}_L$  of SiONP and PMS. The ROI diameter and number of pixels within were 15 nm, 12 pixels, and 60 nm, 208 pixels, respectively. To account for the background intensity and standard deviation, a circular ROI of 60 nm was used to measure  $\bar{S}_B$  and  $\sigma_B$ , respectively.

In order to quantitatively compare the effects of  $t$ ,  $\beta$ ,  $\alpha_p$  on the visibility, of PMS and SiONP, simulated image data was analyzed by measuring the  $\bar{S}_L$ ,  $\bar{S}_B$ , and  $\sigma_B$  from ROI's indicated in Fig. 3.2C. Corresponding  $SNR_L^*$  values were calculated for  $D_e = 19 \text{ e}^- \text{ \AA}^{-2}$  by using Eq. 3.15 and plotted against  $t$  as shown in Fig. 3.3A and B. The range of  $SNR_L^*$ -values that do not fulfill with the Rose-criterion (Eq. 3.16) are plotted in grey, indicating that the nano-objects are probably not visible anymore.

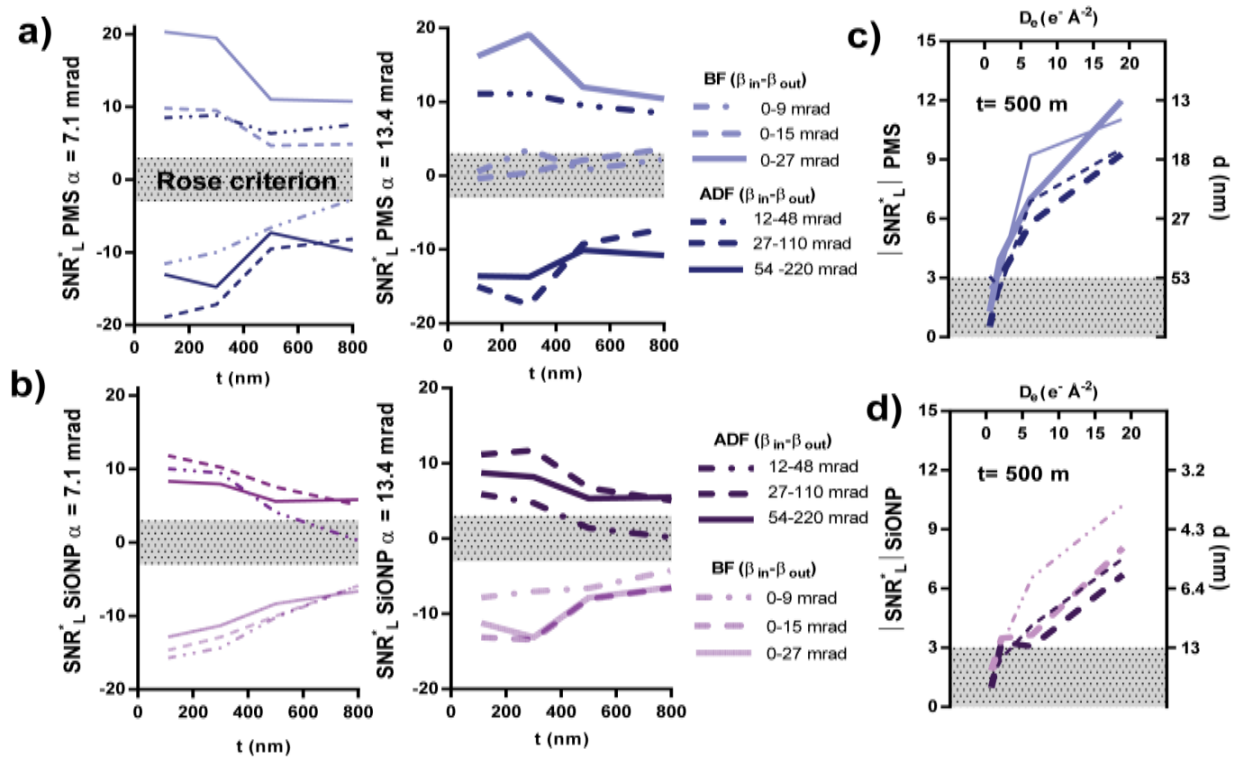


**Figure 3.3 Quantitative comparison between STEM conditions in simulated LPEM of SiONP and PMS.** In A), the  $SNR_L^*$  of PMS was determined from the simulated image data presented in Fig. 3.2B for  $D_e = 19 \text{ e}^- \text{ \AA}^{-2}$  and plotted against the  $t$  for the tested values of  $\alpha_p$  and  $\beta$ . B) is the same for SiONP. In C) and D), is plotted the absolute values of  $SNR_L^*$  as a function of electron dose in order to compare the low dose performance of most optimal BF and DF settings.

According to Fig. 3.3A, the optimal contrast for PMS can be achieved by using BF at  $\beta_{in} - \beta_{out} = 0-27 \text{ mrad}$ , and the selected  $\alpha$  does not affect the image quality significantly. The DF at  $\beta_{in} - \beta_{out} = 27-110 \text{ mrad}$  gave a nearly as good performance, but with an inverse contrast. In Fig. 3.3B, the optimal simulated imaging setting for SiONP is the BF at  $\beta_{in} - \beta_{out} = 0-9$

mrad with a combination of  $\alpha_p = 7.1$  mrad. In the case of DF-detection,  $\beta_{in} - \beta_{out} = 27-110$  mrad delivered the best results independently of the  $\alpha_p$ .

The analyzed data mostly follows the trend where structures are better resolved in thinner liquid layers. Interestingly, when increasing  $t$  from 300 nm to 500 nm, there is a clear drop in the visibility of these nano-objects, after which the image quality plateaus again. For example, see Fig. 3.3A for PMS, BF at  $\beta_{in} - \beta_{out} = 0-27$  mrad.

To estimate the achievable spatial resolution in STEM as a function of the  $D_e$ , Eq. 3.18 was used to translate the  $|SNR_L^*|$  of simulated image data into a value of  $d$  for SiONP (Fig. 3.3C) and PMS (Fig. 3.3D). From the shape of the curves, it seems that the resolution quickly degraded at  $D_e < 5 \text{ e}^{-\text{\AA}^{-2}}$ . In the case of SiONP, individual nanoparticles ( $d < 30$  nm) were resolved with  $D_e$  in the range of 5-10  $\text{e}^{-\text{\AA}^{-2}}$  depending on the detector setting. For PMS, the resolution was inferior, but 100 nm polystyrene particles were resolved with a  $D_e$  around 5  $\text{e}^{-\text{\AA}^{-2}}$  in  $t < 500$  nm.

Finally, it is also interesting to compare how well the Rose-criterion extended to multi-pixel objects describes the visibility of SiONP and PMS. Due to the high  $D_e$  used in simulations, only some of the detector settings resulted  $|SNR_L^*| < 3$  due to the increasing  $t$ . In the case of SiONP, DF setting  $\beta_{in} - \beta_{out} = 12-48$  mrad led to gradual disappearance of SiONP when the  $t$  increased above 500 nm for  $\alpha_p = 7.1$  mrad or above 300 nm for  $\alpha_p = 13.4$  mrad. This agrees well with the visual inspection of Fig. 3.2B.

For PMS, the gradual fading due to the increasing  $t$  took place only for detector setting BF  $\beta_{in} - \beta_{out} = 0-9$  mrad and when the  $t$  increases above 500 nm for  $\alpha_p = 7.1$  mrad. In addition, detector settings BF  $\beta_{in} - \beta_{out} = 0-9$  and 0-15 mrad for  $\alpha_p = 13.4$  mrad led PMS to turn indistinguishable for all tested values of  $t$ . Visual inspection of Fig. 3.2B agreed again with these predictions.

The optimization of imaging parameters via MC-simulations in liquid cell  $t = 500$  nm is summarized in Fig. 3.4. The absolute value of the measured SNR was plotted for all tested values of  $\beta$  and  $\alpha_p$ . In the case of PMS, the best SNR was achieved via  $\beta_{in} - \beta_{out} = 0-27$  mrad

independently of the  $\alpha_p$ . For SiONP, the smaller value of  $\alpha_p$  in combination with  $\beta_{in} - \beta_{out} = 0-9$  or  $0-15$  mrad was optimal.

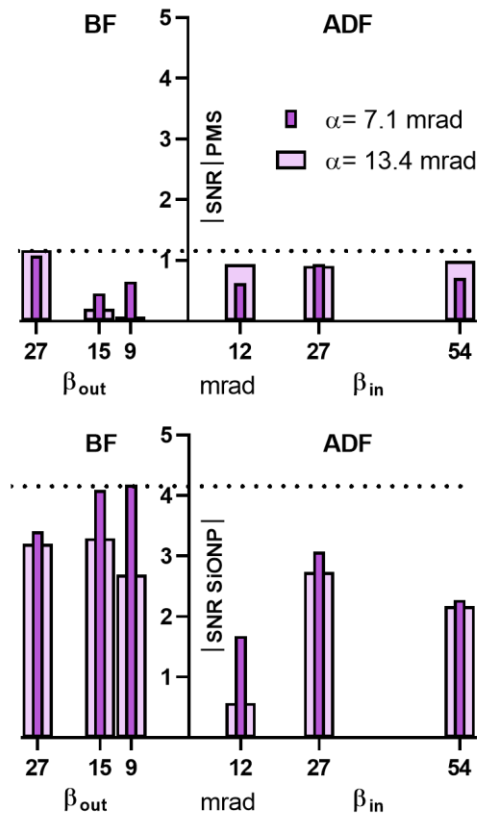


**Figure 3.4 Optimal STEM detection parameters for PMS and SiONP from MC-simulations.** The performance of all tested detection settings is compared side by side for PMS (up) and SiONP (down). The SNR was measured for data simulated in  $t = 500$  nm in liquid and  $D_e = 21 \text{ e}\text{\AA}^{-2}$ .

### 3.2.5 Appearance of binary structures in LPEM

The formation of binary particles results in a core-shell structure as SiONP spontaneously forms a colloidal shell around the larger PMS [1]. Depending on the packing density of the shell, there can be a variation in the observed appearance of the binary structure. To simulate the visual appearance binary particles in LPEM, a core-shell model was modeled in Casino-software. The core consisted of a single PMS particle with constant size and scattering properties (Table 2.2). The shell was constructed by filling it gradually with SiONP and assuming that the  $\text{SiO}_2$  is homogenously distributed along with water.

To determine the scattering properties of the shell, the fractional elemental composition for Si, O, and H ( $f_{Si}$ ,  $f_O$ , and  $f_H$ ) as well as the effective density ( $\rho_{eff}$ ) of the shell was calculated.

The surface area ( $A$ ) of a spherical object with radius ( $r$ ) is given by :

$$A = 4\pi r^2 \quad (\text{Eq. 3.19})$$

The volume ( $V$ ) of a sphere is given by

$$V = \frac{4}{3}\pi r^3 \quad (\text{Eq. 3.20})$$

In order to calculate the  $\rho_{eff}$  for the shell that is occupied by a number of SiONP ( $N_{SiONP}$ ), the shell was approximated to be a rectangular volume divided into cubical cells with a volume ( $V_{cube}$ ) that can each accommodate one SiONP. The area of a side of such cube:

$$A_{cube} = (2r_{SiONP})^2 \quad (\text{Eq. 3.21})$$

And the volume is

$$V_{cube} = (2r_{SiONP})^3 \quad (\text{Eq. 3.22})$$

The maximum number ( $N_{max}$ ) of SiONP that can occupy this shell is

$$N_{max} = \frac{A_{PMS}}{A_{cube}} \quad (\text{Eq. 3.23})$$

We define the fill factor ( $FF$ ) to describe the degree of occupied volume in the shell

$$FF = \frac{N_{SiONP}}{N_{max}} \quad (\text{Eq. 3.24})$$

, where  $N_{SiONP}$  is the number of SiONP in the shell.

The density of any material defined as

$$\rho = \frac{m}{V} \quad (\text{Eq. 3.25})$$

, where  $m$  is mass, and  $V$  is the volume of the object, respectively.

In order to calculate the  $\rho_{eff}$  inside a cubical cell,

$$\begin{aligned}\rho_{eff} &= \frac{m_{SiONP} + m_{H2O}}{V_{cube}} = \\ &= \frac{\rho_{SiONP} \cdot V_{SiONP} + \rho_{H2O} V_{H2O}}{V_{cube}} = \\ &= \frac{\rho_{SiONP} \cdot V_{SiONP} \cdot FF + \rho_{H2O} (V_{cube} - V_{SiONP} \cdot FF)}{V_{cube}}\end{aligned}\quad (\text{Eq. 3.26})$$

To calculate the molar fraction of silica ( $f_{SiO_2}$ ) in each cubical cell, we assume that only water and silica are present in the system.

The molar number ( $n$ ) is defined as

$$n = \frac{m}{M} \quad (\text{Eq. 3.27})$$

, where  $M$  is the molar mass of the material.  $M_{SiO_2} = 60.08$  and  $M_{H_2O} = 18.02 \text{ g mol}^{-1}$ , respectively.

The molar fraction of silica is in the partly filled cell is

$$\begin{aligned}f_{SiO_2} &= \frac{n_{SiONP}}{n_{H_2O} + n_{SiONP}} = \frac{\frac{m_{SiONP}}{M_{SiO_2}}}{\frac{m_{H_2O}}{M_{H_2O}} + \frac{m_{SiONP}}{M_{SiO_2}}} = \\ &= \frac{\frac{\rho_{SiONP} \cdot V_{SiONP} \cdot FF}{M_{SiO_2}}}{\frac{\rho_{H_2O} (V_{cube} - V_{SiONP} \cdot FF)}{M_{H_2O}} + \frac{\rho_{SiONP} \cdot V_{SiONP} \cdot FF}{M_{SiO_2}}}\end{aligned}\quad (\text{Eq. 3.28})$$

, and the molar fraction of water is

$$f_{H_2O} = 1 - f_{SiO_2} \quad (\text{Eq. 3.29})$$

In order to calculate the needed atomic fractions for Silicon ( $f_{Si}$ ), Oxygen( $f_O$ ) and Hydrogen ( $f_H$ ), stoichiometric formulas  $H_2O$  and  $SiO_2$ , were used:

$$f_{Si} = f_{SiO_2} \quad (\text{Eq. 3.30})$$

$$f_O = 2 \cdot f_{SiO_2} + f_{H_2O} \quad (\text{Eq. 3.31})$$

$$f_H = 2 \cdot f_{H_2O} \quad (\text{Eq. 3.32})$$

The maximum number of SiONP was estimated to be 58 (Eq. 3.23). For example, when an image of a binary structure consisting of 1 PMS and 30 SiONPs was simulated,  $N_{SiONP} = 30$ , and calculations resulted following values which were used as input for the sample properties in Casino-software:

$$\rho_{eff} = 1.096 \text{ g cm}^{-3}, f_{Si} = 0.027, f_O = 0.360, \text{ and } f_H = 0.613.$$

The simulation was performed simultaneously for a number of binary structures with different amounts of silica on their shell (Fig. 3.5 A). Casino-file and the Excel-sheet used for obtaining Fig. 3.5 are included in the Supplementary Information.

Judged by the visual appearance, the core-shell structure is best resolved by using BF  $\theta_{in} - \theta_{out} = 0-27$  mrad or DF  $\theta_{in} - \theta_{out} = 54-220$  mrad and  $\alpha = 13.4$  mrad. This conclusion is based on the observation that with these settings, the ring-like structure is observed down to  $N_{SiONP} = 20$ . For other settings, the ring-like structure can be observed only down to the  $N_{SiONP} = 30$ .

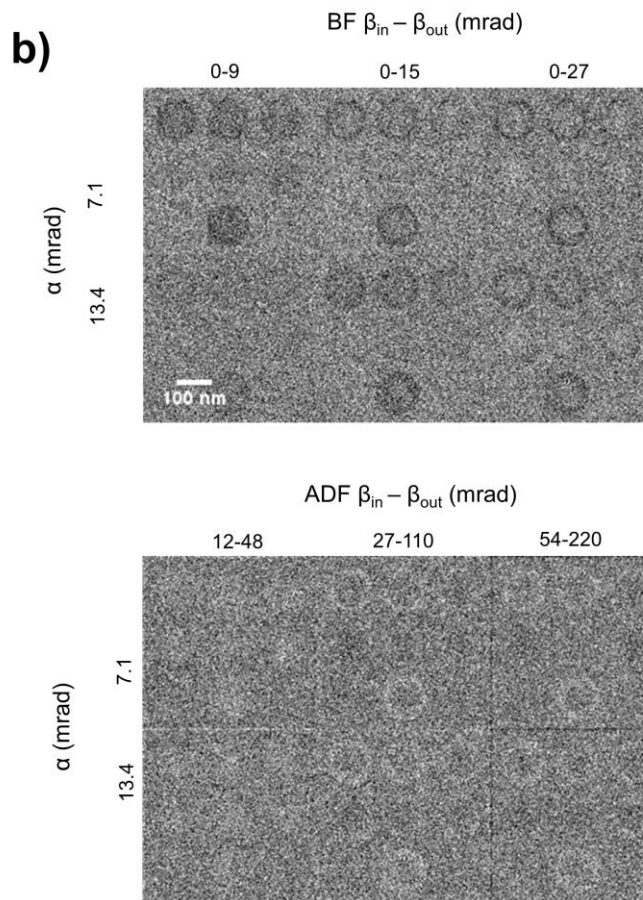
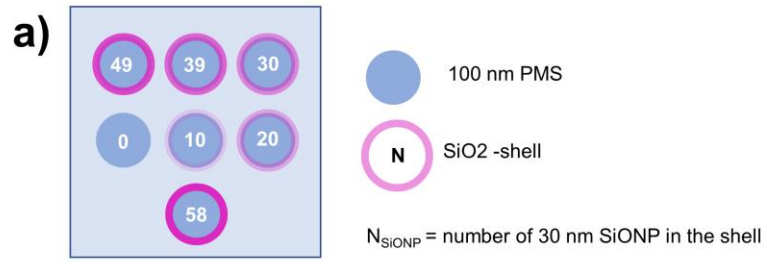


**Figure 3.5 Simulating the core-shell structure of binary particles in  $t = 500$  nm and using  $D_e = 2.1 \text{ e}^{-\text{\AA}^{-2}}$  for BF- and DF- STEM. A) Shows the locations of 100 nm diameter PMS core surrounded by a 30 nm shell with increasing loading of silica (SiO<sub>2</sub>) corresponding to the number of particles ( $N_{SiONP}$ ) added to the shell. B) Simulated BF images for two values of  $\alpha$  and three values of  $\beta_{in} - \beta_{out}$ . C) Simulated ADF images.**

### 3.3 Discussion

To summarize the results, an image analysis method was presented to quantitatively evaluate the visibility (Eq. 3.15) and resolution (Eq. 3.18) of circular multi-pixel objects in noisy image data. A similar method has been presented in [137, 140], where the visibility of multi-pixel objects (or lesions) in biomedical image data was discussed. In both cases, the SNR of the multi-pixel object was found to be proportional to the square root of the number of pixels that occupying the object (Eq. 3.15). This means that if the pixel size of the image is increased, the noise is reduced. The pixel size can be adjusted during the actual image acquisition or in a post-processing step where values of adjacent pixels are averaged.

Monte-Carlo simulations were conducted to estimate the optimal imaging parameters for imaging PMS, SiONP in the liquid cell with  $t$  ranging from 110 - 800 nm. It was found that Eq. 3.15 successfully predicted the visibility of multipixel objects in the simulated data. Simulations estimated that the minimum  $D_e$  required to resolve both PMS and SiONP is in the range of 5-10  $e^{-\text{\AA}^{-2}}$  when optimal detection settings in  $t = 500$  nm are used. This agrees well well with the values obtained via analytical calculations [59] presented in Fig. 1.2.

According to the results summed up in Fig. 3.4, the lower probe convergence angle  $\alpha_p = 7.1$  mrad in combination with small-angle BF imaging  $\theta_{in} - \theta_{out} = 0-9$  is optimal for imaging SiONP in 500 nm of liquid. The benefit of using small probe convergence angle  $\alpha_p$  has been found to be beneficial in related systems [128, 141]. For PMS, the  $\alpha_p = 13.4$  mrad in BF imaging using  $\theta_{in} - \theta_{out} = 0-27$  mrad was found to be optimal. When the visual appearance of binary structures was simulated in Casino-software, results showed that based on the visual judgment, the core-shell structure is best resolved when  $\alpha = 13.4$  is used with BF  $\theta_{in} - \theta_{out} = 0-27$  mrad or DF  $\theta_{in} - \theta_{out} = 54-220$  mrad.

There is a good but not perfect agreement between the MC-simulations and the analytical calculations. (Latter was presented in Fig. 1.1 and Fig. 1.2.) Numerically solved analytical calculations based on [59] suggest that the optimal BF-detection angle for SiONP is at  $\theta_{out} = 16$  mrad for  $\alpha_p = 8$  mrad ( $t = 650$  nm). MC-simulations, on the other hand, indicate that

equally good performance will be achieved with  $\beta_{out} = 9$  and  $\beta_{out} = 15$  when using  $\alpha_p = 7.1$  mrad ( $t = 500$  nm). This discrepancy could be because the inelastic scattering is omitted in MC-simulations, which is expected to overestimate the performance at low values of  $\beta$ , as shown in Fig. 1.4. When imaging SiONP with DF, the optimal  $\beta_{in}$  was found to be 35 mrad from analytical calculations and 27 mrad based on MC-simulations. This can be considered a good match because only a few values of  $\beta_{in}$  were tested in the Casino-software.

For PMS, analytical calculations indicated optimal BF detection at  $\beta = 26$  mrad, which aligns well with the MC-simulations where  $\beta = 27$  mrad was found to be optimal from the tested detection settings. DF-detection for PMS was found to be slightly inferior. This aligns with experimental evidence from [128], where BF-detection was found to be better than DF, when imaging bacterial cells in liquid.

### 3.4 Conclusions

One of the main advantages of MC-simulations is that several parameters of the sample and the microscope can be tested before starting expensive and time-consuming laboratory work. Secondly, simulated image data can be directly compared with experimental data and analyzed by using the same methods. On the downside, executing MC-simulations tended to be more time consuming than performing numerical calculations based on the recent theory [59].

It was shown that the Rose-criterion could be extended to describe the visibility of multi-pixel objects by considering the statistical behavior of the noise while binning the images.

In current work, several parameters were tested, and it was found that BF-detection with  $\beta = 15$ -27 mrad should be optimal for imaging low-atomic number materials such as SiONP and PMS. This is in accordance with recent results obtained with Monte-Carlo simulations [120] and experimental data [128]. If DF-STEM is to be used,  $\beta = 27$ -35 mrad is expected to be optimal in liquid thicknesses of 500 nm. Furthermore, numerical calculations predicted that nearly optimal performance for DF-STEM would be obtained with also higher values of  $\beta$  (Fig. 1.2).

So far, we did not validate these results against experimental data, which would be an important step to evaluate the accuracy and impact of this work so far.

## Chapter 4. Imaging colloidal assemblies in a liquid cell

*“How to image low-Z colloidal assemblies in liquid?”*

### 4.1 Introduction

LPEM potentially allows capturing the structure of low-atomic number material in nanometer resolution as was demonstrated in Fig. 1.6. Recently, structures and processes have been resolved for vesicles [24], organic crystals [81], biomolecules [40], whole cells [142], and colloidal superlattices [98].

In order to obtain nanometer resolution in LPEM as predicted by the theory, two experimental challenges need to be solved. First, the object should stay immobilized for the duration of image acquisition to avoid motion blur effects, and secondly, the sample should be imaged before it gets damaged by the electron beam.

It is a common observation that the colloidal particles and other nano-objects immobilize on the surfaces of the liquid cell due to the favorable interaction with their liquid-solid interface [18]. It has been shown that this interaction can be tailored by functionalizing the  $\text{Si}_3\text{N}_4$  surface with charged groups [48] or by specific interaction via immunologic tethering [143].

It is unlikely that the beam damage can be completely avoided, and hence the beam-induced effects need to be considered when interpreting the data. For amorphous materials, such as studied in this work, the electron beam damage has been observed to manifest as shrinking [128], disintegration, and fading [144] of the irradiated structures. Ideally, by recording a sequence of images and analyzing the beam analyzed changes, a threshold value for cumulative electron dose [39] or electron dose rate [47] can be determined.

#### 4.1.1 Beam damage of polystyrene and Silica

Specific materials studied in this work are polystyrene (PS), and silicon oxide (silica), which are both expected to be susceptible to electron beam damage. When PS particles were studied with cryo-EM, it was observed that they started shrinking at electron doses between  $\sim 120\text{-}600\text{ e}^{-}\text{\AA}^{-2}$  indicating structural damage [145]. Electron energy-loss spectral (EELS) studies conducted on PS at cryogenic temperatures of 123 K indicated that low-loss signal arising from the aromatic phenyl group started decreasing if cumulative electron doses higher than  $\sim 600\text{ e}^{-}\text{\AA}^{-2}$  were used [129]. It is notable that at room temperature  $T = 293$  (RT), the equivalent damage was obtained by using a factor of 5 smaller electron dose.

When PS was studied with Environmental scanning electron microscopy and post-mortem FTIR-analysis, it was found that higher water vapor pressures in the microscope led to faster degradation of the material [94]. The degradation process was characterized by the appearance of carbonyl and hydroxyl bands in the FTIR-spectrum and the simultaneous disappearance of the  $-\text{CH}_3$  and  $-\text{CH}_2$  bands. It was proposed that two mechanisms are responsible for the observed changes in the FTIR-spectrum of PS: First, the direct effect of the beam interacting with the PS film leads to scissoring of C-H bonds and crosslinking of the molecules leaving behind carbon-rich residue. Secondly, when an electron beam interacted with the gas atmosphere or condensed liquid, free-radicals are created which attack the polymer structure leading to hydrolysis and oxidation. Interestingly, it was found that when water condensation, there was an increase in the polymer hydrolysis when water vapor was condensing on the sample. This indicates that the liquid water can, in some cases, enhance the electron beam damage of PS.

Silica may as well undergo changes when exposed to an electron beam. Studies focused on the electron beam damage in oxides materials in general, have shown that the electron beam can lead to, for example, valence-state reduction and mass-loss involving the collective displacement of material in the irradiated area [146]. When silica nanoparticles were imaged in liquid, it was found that cumulative electron doses in the order of  $10^3\text{-}10^4\text{ e}^{-}\text{\AA}^{-2}$  induced deformation of spherical nanoparticles where the deformation was

dependent on the scanning direction of the STEM-probe [130]. In a follow-up study, it was shown that radical scavenger such as acetic acid could be used to stabilize the silica structure to mitigate electron beam effects in liquid [147]. Furthermore, it was proposed that reducing radicals, such as H·, are responsible for the degradation of silica nanoparticles in the presence of water.

To summarize, PS and silica are both expected to be sensitive to the electron beam-induced changes in liquid. PS is an organic polymer, and the direct damage from the electron beam will likely occur at  $D_e$  of 120 - 600  $e^{-\text{Å}^{-2}}$  at the RT. In addition to the direct beam damage, secondary damage from the free-radicals created in water vapor or liquid is expected to damage the structure as well.

The silica, on the other hand, is an inorganic oxide and hence is expected to be more stable in terms of the direct beam damage. However, for  $D_e =$  of  $10^3 - 10^4 e^{-\text{Å}^{-2}}$ , the deformation of SiO<sub>2</sub> has been observed. It is thus likely that PMS will be the component that limits the maximum acceptable  $D_e$  that can be applied when imaging binary assemblies in liquid. Finally, it should be noted that the surface functionalization of both particles may be affected already at much lower electron dose rates [113]. This might have a considerable effect on the dynamic processes of self-assembling structures [7].

#### **4.1.2 Experimental considerations on optimizing the data acquisition**

As it was shown in Chapter 3, the SNR can be, to some extent, improved by optimizing imaging settings and/or reducing the liquid thickness ( $t$ ). Nevertheless, the simulations suggested that electron doses of 5 - 10  $e^{-\text{Å}^{-2}}$  are required to resolve individual PMS or SiONP particles in 500 nm of liquid. Hence, this could translate into a sequence of 50-20 images if acceptable  $D_e$  for PMS is 100  $e^{-\text{Å}^{-2}}$  and that the sample is irradiated only during the image acquisition.

#### **4.1.3 Validation of the contrast and post-mortem analysis**

Another challenge in LPEM of low atomic number material is that the low SNR data can be overwhelmed by any other source of contrast in the system. For example, metallic ions can be reduced on the solid-liquid interface [85] or on solvated structures [102]. Therefore,

metallic contamination may cause unintentional “staining” of the low-contrast structures in an LPEM experiment. Hence, in an ideal case, the observed contrast in a liquid cell experiment is validated by means of a standard sample or, for example, compared to calculated or simulated contrast. Furthermore, *in situ* or *post mortem*, elemental analysis can be conducted to confirm the contents of the liquid cell.

## 4.2 Results

### 4.2.1 Validation of simulated data

To determine whether the simulated data matched experimental results obtained with STEM, either a monolayer of SiONP or PMS was immobilized on the upper window of a liquid cell. After closing the cell, the sample was first examined in ambient conditions and then filled with liquid.

In the case of SiONP, the average  $t/\lambda$  of a dry cell was measured to be 0.75, matching the expected thickness for 100 nm of Si<sub>3</sub>N<sub>4</sub> of 0.73 (Appendix II). The liquid was subsequently introduced to the system by turning on the syringe pump to flow in the aqueous saline (20  $\mu$ L/min) until the liquid filled the whole field of view. The average  $t/\lambda$  across the field of view was measured with EELS log-ratio-technique to amount 3.34, corresponding to 460 nm liquid after subtracting the contribution of windows (Eq. 2.2). 10 STEM images were recorded using  $D_e = 2.3 \text{ e}^{-\text{\AA}^{-2}} / \text{frame}$ . However, due to the continuous function of our scanning unit and limited data transfer speed of the system, the total irradiation of the sample was higher than  $23 \text{ e}^{-\text{\AA}^{-2}}$ . Based on the time between the captured frames (10.48 s) and the set flyback time (10 ms), the total  $D_e$  experienced by the sample was estimated to be a factor of two higher. Images were manually aligned and averaged in a cumulative manner to obtain an image stack in which each consecutive frame was acquired with a higher  $D_e$ . To measure the average SNR of SiONP, 24 particles were selected at a distance of  $0.95 \pm 0.05 \mu\text{m}$  from the edge of the window, which corresponded to a column of 350 nm of liquid measured with the EELS. For analysis of the SNR, the area of the signal was defined by a 15 nm diameter (Fig. 3.1), a spherical region of interest (ROI) in the middle of each selected particle. To measure the average intensity of the standard deviation of the

background signal, an  $880 \times 90$  nm rectangular ROI was created with an area of  $0.079 \mu\text{m}^2$ . The average SNR value for SiONP in 350 nm of liquid was calculated according to Eq. 3.7. During the image acquisition, no observable movement or changes in the intensity was present.

The MC-simulation and analytical calculations were performed with corresponding parameters and setting  $d_{PMS} = 110$  nm and  $d_{SiONP} = 25$  nm. Simulated data were analyzed, as was described in Chapter 3. The analytical SNR was calculated by using Eq. 1.25, where  $N_o$  was given by Eq. 1.29 with  $s$  was set to 3.7 nm. Matlab-scripts are provided in the Supplementary Information.

In Fig. 4.1A, experimental and simulated data were compared side-by-side, which indicated a good visual match. Fig. 4.1B shows that the experimental, analytical, and simulated SNR seem to match within the factor of two, whereby the value predicted by simulation is highest.

When studying the experimental contrast of PMS, some residual liquid was present in the cell after the sample preparation. EELS-measurements showed that the average  $t/\lambda$  of the cell was 1.21, amounting to a  $t = 83$  nm and suggesting only a partly filled cell. A series of 50 STEM images were acquired, resulting in a total of  $D_e = 23 \text{ e}^{\text{\AA}^{-2}}$ . (In the next section, this dataset was analyzed to determine structural beam damage of PMS.) In order to determine the SNR of PMS in thicker liquid, a total of 240  $\mu\text{L}$  of 1:2 SiONP -diluted was injected with PBS of pH 2 using a syringe pump with a flow rate of 20  $\mu\text{L}/\text{min}$ . After one hour, a stack of 27 images was acquired using  $\alpha = 13.4$ ,  $\beta = 54$  mrad,  $\tau = 4 \mu\text{s}$ , and  $s = 3.3$  nm, so that cumulative  $D_e = 50 \text{ e}^{\text{\AA}^{-2}}$ . The average  $t$  across the field of view was measured with EELS as  $t/\lambda = 4.32$ , which is equivalent to 627 nm of water. Although the liquid layer got considerably thicker after the injection of SiONP suspension, no SiONP was seen in the images. To prepare the dataset for analysis, the first frame was removed, and the dataset was aligned. In the case of PMS, the area of the signal was specified by placing 60 nm diameter, spherical ROIs in the middle of 10 particles that were residing  $1.3 \pm 0.3 \mu\text{m}$  from the edge of the window, where the liquid  $t$  was 650 nm. To measure the average intensity

and standard deviation of the background, a polygonal ROI was used with an area of  $0.096 \mu\text{m}^2$ . Results shown in Fig. 4.1 C-D indicate that there is again an agreement within the factor of two; however, in this case, the experimental data shows a stronger negative contrast than the simulated data. During the irradiation, PMS was observed to gradually fade, shrink, or detach from the window.

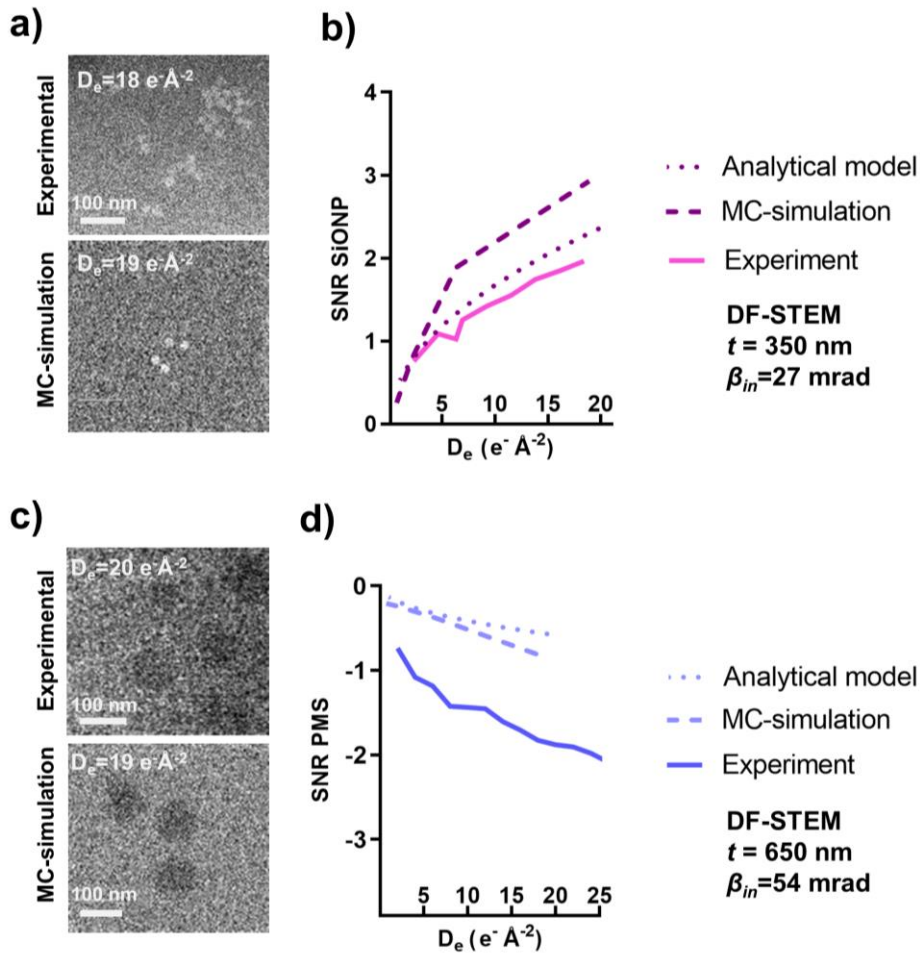


**Figure 4.1. Directly comparing experimental, simulated, and analytically obtained SNR of SiONP and PMS imaged in a liquid cell.** A) Experimental vs. simulated image data is shown for SiONP.  $\alpha_p = 13.4$ , and  $\beta = 27 \text{ mrad}$ ,  $\tau = 5 \mu\text{s}$ , and  $s = 3.3 \text{ nm}$ . B) The average experimental SNR for SiONP is plotted with the SNR obtained from analytical calculations and MC-simulations with corresponding parameters. C) Experimental vs. simulated image data is shown for PMS  $\alpha_p = 13.4$ ,  $\beta = 54 \text{ mrad}$ ,  $\tau = 1 \mu\text{s}$ , and  $s = 3.3 \text{ nm}$ . In D), the average experimental SNR of PMS is plotted as a function of cumulative  $D_e$  along with the SNR obtained from analytical calculations and MC- simulations.

#### 4.2.2 Study on the structural beam sensitivity of PMS

It was observed that when PMS was irradiated in liquid, it disappeared from the field of view. The process is depicted in Fig. 4.2A, where prior to the acquisition of the image, the lower part of the panel was pre-irradiated with a cumulative  $D_e = 42 \text{ e}^- \text{Å}^{-2}$ . At the edges of the pre-irradiated area, the data shows some partially disappeared PMS, as highlighted by the arrowheads. The observation suggests that PMS does not disappear as a whole but disintegrates while still attached to the liquid-solid interface. Because the shrinking of PMS will most likely also affect the observed structure of self-assembled binary structures, it was important to understand the relation between the electron dose and the size of the PMS. This was achieved by first analyzing the data from the sample already shown in Fig. 4.1C-D and secondly, from another sample where PMS was imaged in an empty liquid cell filled with ambient atmosphere.

The data presented in Fig. 4.1C-D was analyzed, and the size of PMSs in the liquid was directly measured as a function of  $D_e$ . Due to the low inherent contrast of PMS, data was noisy, and it was not possible to follow the hypothesized shrinking process on a single particle level. Hence, the size distribution of several PMSs was evaluated as a function of  $D_e$ . Secondly, the noise in the data was reduced by averaging consecutive frames in an image stack (running average). This resulted in a reasonable trade-off between SNR and the number of data points that we obtained for analysis. To automatically analyze the diameter of selected PMSs in a sequence of images, an ImageJ script was created to detect, segment, and measure projected areas of several particles in an image stack.

The analysis was initiated by first creating a running average of five consecutive images in the recorded data that resulted in an effective  $D_e$  of  $10 \text{ e}^- \text{Å}^{-2}$  per frame (Fig. 4.2B). This data was fed to the image processing pipeline described in Appendix III. In short, a bandpass filter was applied that further increased the SNR by averaging values, which effectively reduced the pixel size and thus increased the SNR (Eq. 3.15). As shown in Fig. 4.2C, the bandpass filtering improved the visibility of PMSs' outline that was segmented by the algorithm, as shown in Fig. 4.2D. The ImageJ-script is provided with the Supplementary Information.

It was also tested if the structure of PMS changed when the cell was filled with an ambient atmosphere by studying an air-dried PMS-sample in a sealed liquid cell. In addition, the effect of illumination mode (TEM/STEM) was tested. The air-dried sample showed a negligible water thickness as the EELS thickness measurement indicated  $t/\lambda = 0.78$ . Next, the microscope was switched into TEM-mode, and a sequence of 40 images giving a total  $D_e = 25 \text{ e}^- \text{Å}^{-2}$  was recorded from a previously unexposed area. The microscope was then switched back to STEM-mode, and a sequence of 80 images was acquired at an unexposed region resulting in a total  $D_e = 36.7 \text{ e}^- \text{Å}^{-2}$ . Again, a running average of five consecutive frames was created from the data before it was fed to the processing pipeline.

In Fig. 4.2E, the determined PMS size distribution in  $t = 600 \text{ nm}$  was plotted for several values of  $D_e$ . It was seen that the apparent diameter of the particles decreased and indicated possible shrinkage due to the electron irradiation. A one-way analysis of variance (ANOVA) was performed on the datasets, and it showed that a statistically significant change was indeed taking place in the population of 208 PMS, whereby  $D_e = 20 \text{ e}^- \text{Å}^{-2}$  was required in order to observe the shrinking with a minimum of 99 % statistical confidence (indicated as \*\* in the Fig. 4.2E).

In Fig. 4.2F, the shrinkage of PMSs under four different experimental conditions is plotted as a function of  $D_e$ . When a layer of air-dry PMSs is imaged at an ambient atmosphere, a similar rate of shrinking took place regardless of whether STEM or TEM mode was used. The shrinking of PMS was found to be faster in liquid than in the atmosphere. Moreover, the shrinking was found to be more rapid in  $t = 83 \text{ nm}$  than in  $t = 650 \text{ nm}$ . As a result, the information provided in panel F can be used to estimate the change in the spatial distribution of the PMS in a binary particle when imaged with a given  $D_e$ .

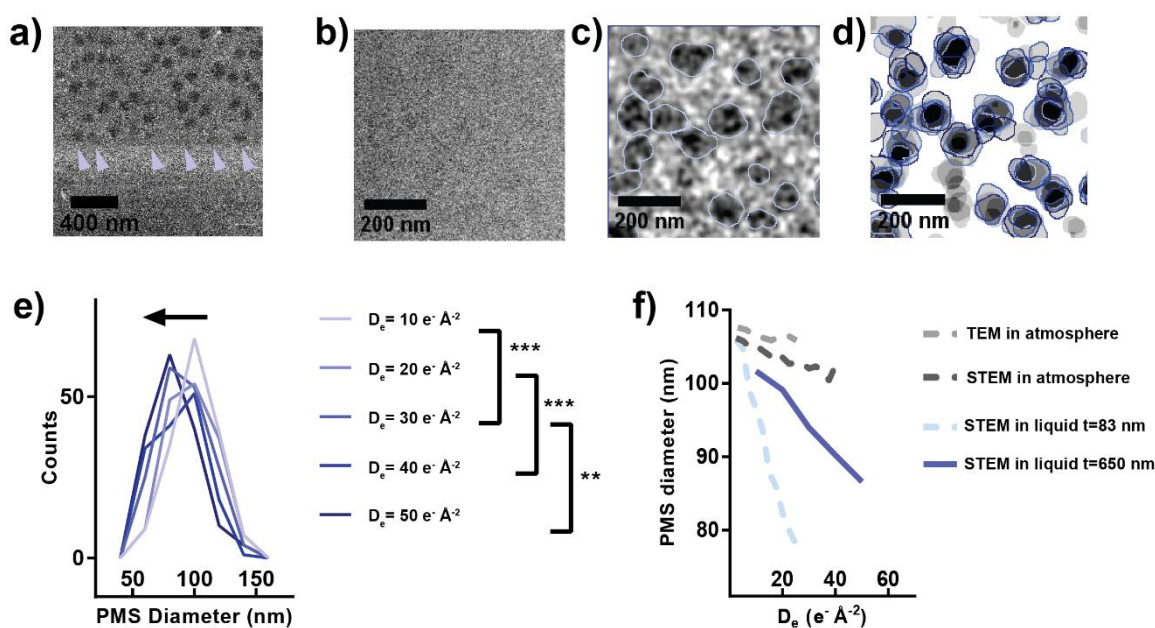


**Figure 4.2. Statistical analysis shows electron beam-induced shrinking of PMS in liquid and air.** A) The lower part corner shows the effect of extended irradiation on PMS monolayer imaged in  $t = 83$  nm. Pre-radiation was delivered to the lower part of the sample in STEM-mode by acquiring the first 50 frames using  $\tau = 1 \mu\text{s}$  and then 2 frames with  $\tau = 20$ . The acquisition of the final image was made with  $\tau = 20$ , and the liquid  $t$  on the adjacent region of the cell was measured to be 83 nm, as reported in the previous section. Arrowheads point to partially removed PMS. In B) PMS is imaged in 650 nm of liquid using  $\alpha_p = 13.4$ ,  $\beta = 54$  mrad,  $\tau = 1 \mu\text{s}$ , and  $s = 3.3$  nm resulting  $D_e = 10 \text{ e}^- \text{ \AA}^{-2}$ . C) is same as the B), but after bandpass-filtering and showing the segmented outline obtained via an image processing pipeline. In D), the segmented objects from five successive frames have been averaged, and objects included in the statistical analysis have been outlined. E) The size distribution of PMS moves toward smaller values as the sample is irradiated, indicating a gradual shrinkage. Asterisks on the legend indicate the statistical probability ( $P$ ) that there is a decrease in segmented diameter.  $P \leq 0.01$  and  $0.001$  for  $**$  and  $***$ , respectively. In F), the size evolution of PMS in the liquid is  $t = 83$  nm, and 650 nm are plotted as well, as the data of air-dried PMS obtained at ambient atmosphere with TEM and STEM.

#### 4.2.3 Imaging pre-formed binary structures

In order to image self-organized binary structures in STEM-mode, they were synthesized by mixing PMS and SiONP prior to measurements. The suspension was diluted 1:10 with HPLC-water, and 2  $\mu\text{l}$  of the mixture was directly loaded into the liquid cell by pipetting it on a plasma cleaned chip. No spacer was used. The average thickness of the cell was measured, indicating  $t/\lambda = 3.97$  that corresponded to 566 nm of liquid. A typical overview

image of the sample is shown in Fig. 4.3A, where structures with varying contrast are visible. Here, pin-pointed by the arrowheads, are visible objects of lower intensity that disappeared from the field of view after a few seconds of constant irradiation. Dynamics of one such structure was captured by recording a sequence of 32 frames with a  $D_e = 0.46 \text{ e}^- \text{ \AA}^{-2}$  per frame and a frame rate of 1.66 FPS. This resulted in a video where binary particles first started rotating and then disappeared from the field of view, leaving behind a few SiONPs attached at the liquid-solid interface. The behavior of these binary structures in the liquid is shown in Fig. 4.3B, where three STEM frames from the video are shown at time points 1.2, 18, and 36 s.

In Fig. 4.3C, eight first frames of the video have been manually aligned and averaged, resulting in  $D_e$  of  $4 \text{ e}^- \text{ \AA}^{-2}$ . The image reveals the Raspberry-type structure, while some of the binary particles are slightly blurred due to their movement.

Many high-contrast structures were visible on the slightly different focal depth and did not react to the beam. After the LPEM experiment, the cell was opened, and both windows were inspected in SEM. On the bottom window, particles were found on both sides, which supports the assumption that bright structures in Fig. 4.3A are dried deposits of binary suspension.

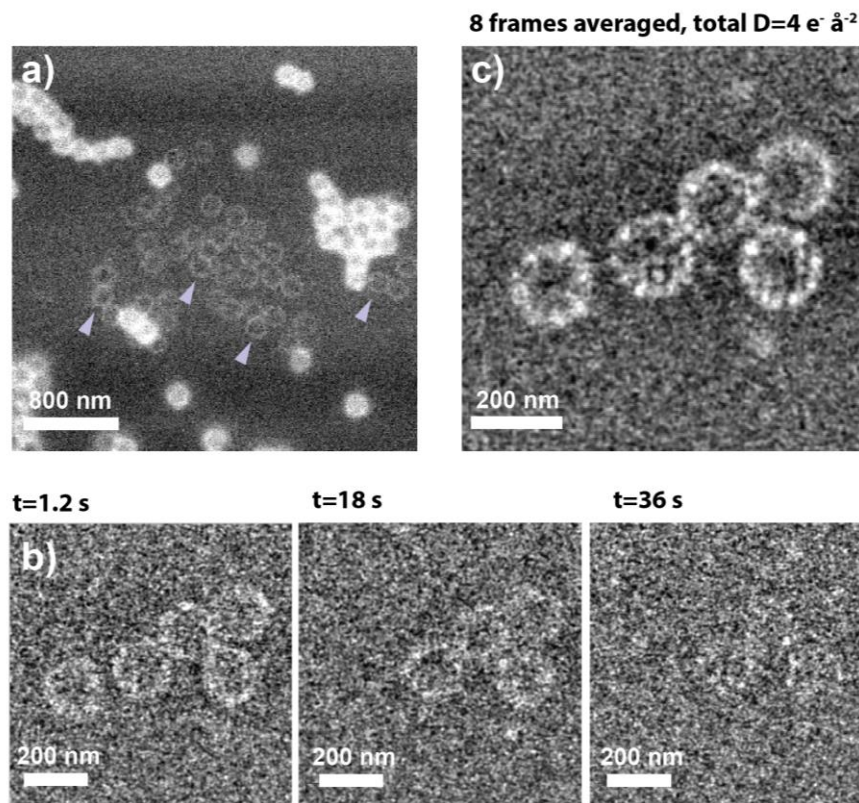


**Figure 4.3 Imaging the structure and dynamics of binary particles in a liquid cell with DF-STEM.** In A) an overview image of a liquid cell experiment showing immersed binary structures imaged with  $s = 10 \text{ nm}$  and  $\tau = 20 \mu\text{s}$  (arrowheads). In B), an image sequence showing a gradual detachment or degradation of binary structures from the liquid-solid interface, leaving few silica nanoparticles behind. Images in the sequence were acquired with  $\theta = 54 \text{ mrad}$ .  $s = 3.3 \text{ nm}$  and  $\tau = 1 \mu\text{s}$  in  $t = 500\text{-}600 \text{ nm}$  and  $D_e = 0.46 \text{ e}^-\text{\AA}^{-2}$  per frame resulting a frame time of  $1.2 \text{ s}$ . In C), 8 aligned frames have been averaged resulting cumulative  $D_e = 4 \text{ e}^-\text{\AA}^{-2}$  to show the characteristic raspberry structure these binary particles.

#### 4.2.4 Comparison of TEM and STEM

The image quality in TEM and in STEM was compared by switching the microscope into TEM-mode and imaging the same sample as above. After the image acquisition in STEM-mode (above), the sample was removed, and the microscope was aligned with the standard AuNP sample in TEM-mode. A nominal magnification of 800kx (GIF-mode) was selected that corresponded to a  $s = 1.65 \text{ nm}$  with Binning 1 of the Gatan UltraScan1000XP – camera. In order to calibrate the  $D_e$ , a sample position was located where no carbon membrane was visible, and the “brightness” was adjusted until the desired intensity on

the camera corresponding to  $D_e = 2.8 \text{ e}^{-\text{\AA}^2\text{s}^{-1}}$  was reached. The corresponding condenser lens setting was saved to the memory of the microscope and used for image acquisition.

Next, the liquid sample earlier imaged in STEM-mode was inserted in the microscope and brought to the eucentric height. The edge of the window was located, and the focus was adjusted. For accurate control of the  $D_e$  and to avoid irradiating samples outside the imaging area, the automatic beam blanker (Gatan, USA) was enabled, and the stage was moved to a new position and was let to stabilize for 1 minute. After this, a sequence of 10 images with an exposure of 1 s was acquired. The procedure was repeated in three locations until a satisfactory sequence was captured. In Fig. 4.4B, is shown the first image of this sequence. In panel D, five consecutive frames were averaged, resulting in a cumulative  $D_e$  of  $14 \text{ e}^{-\text{\AA}^2\text{s}^{-1}}$ . During the image acquisition, no movement or changes of binary structures was observed. Based on the visual appearance of these images, TEM images seems to be slightly astigmatic and show weaker contrast than STEM images in panels A and C.

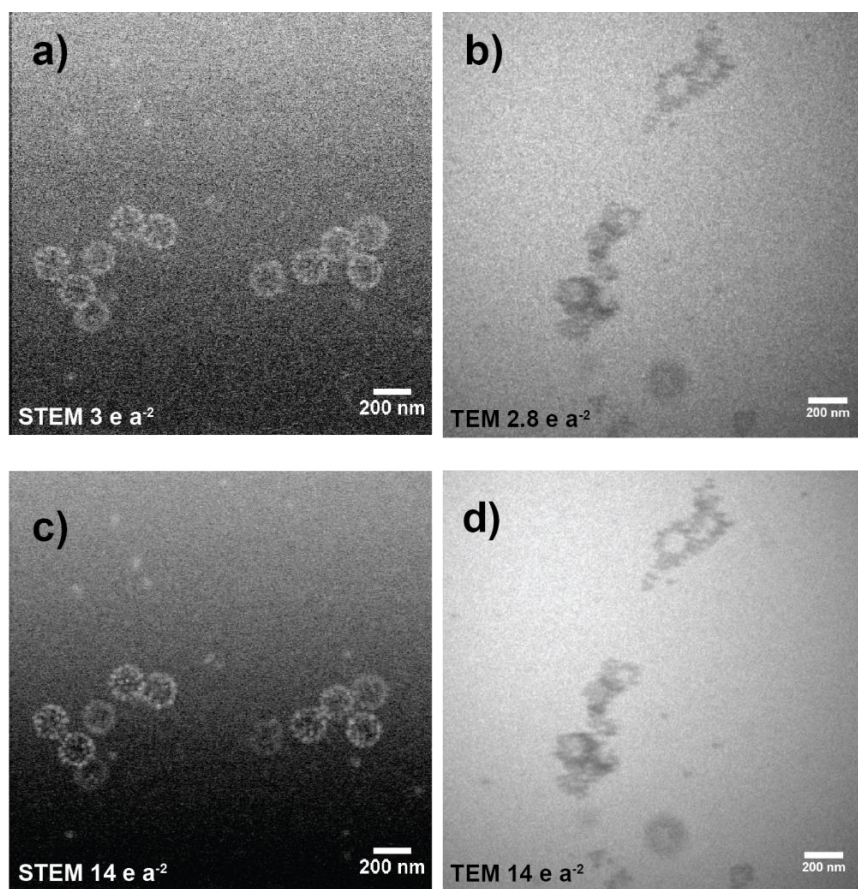


**Figure 4.4** A qualitative comparison of images obtained from binary structures in liquid cell using STEM and TEM,  $t = 500\text{-}600\text{ nm}$ . In A) binary structures shown in previous section are imaged using DF-STEM with  $s = 3.3\text{ nm}$ ,  $\tau = 1\text{ }\mu\text{s}$ ,  $\beta = 54\text{ mrad}$ . 6 frames were averaged, resulting  $D_e = 3\text{ e}^{-\text{\AA}^{-2}}$ . In B) binary structures from the same sample was imaged using BF-TEM and  $s = 1.65\text{ nm}$ , exposure time of  $1\text{ s}$ ,  $\alpha = 32\text{ mrad}$ , resulting  $D_e = 2.8\text{ e}^{-\text{\AA}^{-2}}$ . The C) is same as A, but 28 consecutive frames were averaged resulting  $D_e = 14\text{ e}^{-\text{\AA}^{-2}}$ . D) is same as B but 5 consecutive frames were averaged giving  $D_e = 14\text{ e}^{-\text{\AA}^{-2}}$ .

#### 4.2.5 Artifacts and cross-contamination

During many of the experiments, bright artifacts appeared in the irradiated area of the sample. The deposition of high-contrast artifacts is demonstrated with two datasets. In the first one, pre-assembled binary particles were diluted 1:10 ratio with PBS pH 2 and directly loaded them into a liquid cell using a 200 nm spacer between the chips. The sample was imaged in STEM-mode 36 hours later using  $s = 3.3\text{ nm}$  and  $\tau = 4$ , resulting in  $D_e = 1.9\text{ e}^{-\text{\AA}^{-2}}$  per frame. The stack was automatically aligned, and the first 10 frames of the stack were averaged. The resulting image is shown in Fig. 4.5A, where bright speckles have appeared

on PMS as well as on the window. To study the structure and elemental composition of these artifacts, the holder was removed from the microscope and flushed by flowing approximately 200  $\mu\text{l}$  of HPLC-water to remove the excess salt. The liquid cell was opened, the bottom chip was blotted dry with a piece of lint-free tissue and placed on a regular sample holder. The sample was imaged *post mortem* in DF-STEM mode (Fig. 4.5B). An EDX spectrum image with a size of  $64 \times 64$  pixels using  $I_p = 1.2$  nA and  $\tau = 200$   $\mu\text{s}$  was collected. All spectra from a total of 346 sweeps were summed and plotted in Fig. 4.5C, where chromium and copper signals are present.

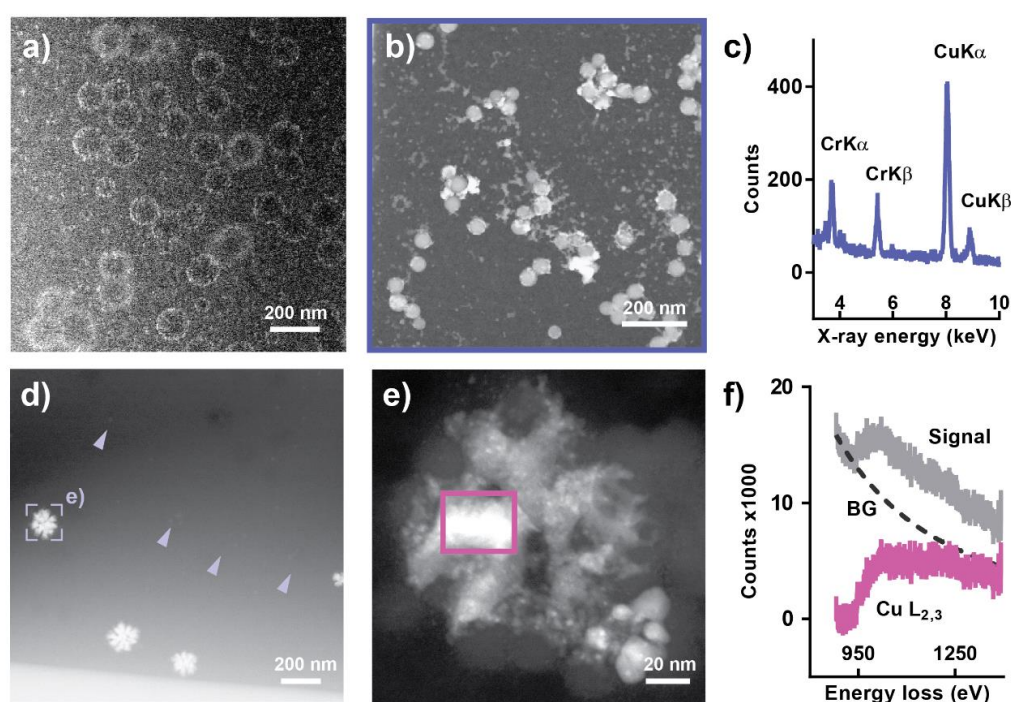


**Figure 4.5 High-contrast artifacts encountered in the liquid cell STEM experiments when imaging pre-assembled binary particles and SiONPs.** In A) bright spherical structures formed under electron illumination when a sample similar to the one presented in Fig. 4.3 and Fig. 4.4 was imaged after 24 hours had passed from the loading suspension into the liquid cell. *Post mortem* EDX-analysis of the sample in C) reveals homogeneously distributed of copper and chromium all over the area shown in B). In C) suspended SiONP is imaged in  $t = 500$  nm and  $D_e = 7.2$   $\text{e}^{-}\text{\AA}^{-2}$  per frame. In the image sequence, bright structures can be seen forming on the windows with some SiONP rotating around them. The E) shows a high magnification *post mortem* image of one of the formed structures of panel D). Here, the high-contrast structure has deposited on an aggregate of SiONP. The electron energy loss (EELS) -mapping shows a copper signal colocalization with the high-contrast structure as shown in F) where the summed EELS-spectrum from the area indicated in E) shows the characteristic Cu  $L_{2,3}$ -edge.

In the second example, the formation of some high contrast features was observed when imaging suspension of SiONP was imaged in a liquid cell. SiONP was diluted 1:5 with PBS pH 2, and 0.2  $\mu\text{l}$  was directly loaded of this on the bottom chip, and the cell was sealed, placing a chip with 200 nm spacer on top. The  $t/\lambda$  of the cell was measured to be 3.43, indicating an average  $t = 470$  nm across the field of view. A stack of 20 images was acquired in STEM-mode using  $s = 1.9$  nm and  $\tau = 5$   $\mu\text{s}$  amounting to  $D_e = 7.3$   $\text{e}^{-\text{\AA}^{-2}}$  per frame. The stack was manually aligned, and the image shown in Fig. 5.5D was obtained after averaging ten last frames of the stack. The data shows high-contrast features appearing on the window as well as few stationary SiONPs (arrows). After the measurement, the cell was opened and rinsed in a beaker of 20 ml of HPLC-grade water and blotted dry with a piece of lint-free tissue. The bottom chip was placed on a standard specimen holder examined the sample in STEM-mode using  $I_p = 400$  pA,  $\tau = 20$   $\mu\text{s}$ , and pixel size of 0.47 nm. The location highlighted in Fig. 4.5D was located *post mortem* (Fig. 4.5E). An EELS spectrum image of size  $26 \times 32$  pixels was recorded using  $s = 3.7$  nm pixel, and  $\tau = 0.1$ s. To locate the copper  $L_{2,3}$  - edge at 931 – 951 eV, the spectrometer was set to record the energy range of 881-1293 eV. In order to increase the SNR of the collected spectra, an area of  $7 \times 6$  pixels was summed from the area indicated in panel E. After fitting and subtracting the exponential background from the spectrum in Gatan Digital Micrograph-software, the characteristic copper  $L_{2,3}$  -edge was visible (Fig. 4.5F). Copper edge was not observed outside of the high contrast features.

In order to investigate if the copper was coming from the sample solution, we performed an ICP-OES analysis on PBS pH2, PBS pH7 as such, and for the SiONP suspension diluted it with HPLC -grade water 1:20. In all samples, the concentration of copper at the wavelength of  $\lambda = 324.754$  nm was lower than the reported limit of detection, 0.00162 mg/ml that corresponds to 1.62 parts per billion.

### 4.3 Discussion

In summary, we have investigated the possibility of using LPEM to study the structure and dynamics of self-assembled low-atomic number material. SiONP and PMS were imaged in a liquid cell using DF-STEM. The experimental SNR was directly compared *in silico* values

obtained with MC-simulations [4] and an analytical model adapted from [59]. For the tested parameters, experimental data matched with values from *in silico* methods within a factor of two. Moreover, better agreement existed between the two *in silico* methods. The outcome thus implies that MC-simulation can also be used for low-Z colloidal nano-objects to predict the image contrast in the experimental data. This agrees with some earlier studies on related systems. For example, when MC-simulations were compared for imaging carbon nanotubes embedded in polymer matrix [120], simulated and experimental data agreed nearly perfectly. Good agreement has also been found in LPEM studies, where intracellular compartments [49] and gold nanoparticles [4] were studied.

For many occasions, attempts to experimentally find the optimal imaging parameters for SiONP and PMS were complicated by the metallic artifacts that formed when on irradiated areas of the sample. The electron beam likely reduced copper ions on windows and on PMS particles, which resulted in high-contrast features on the images. Similar phenomena have been observed for vesicles that were labeled *in situ* using Ni<sup>2+</sup>-ions [102] as well as for cell-derived vesicles that were stained *in situ* using chloroauric acid [148]. Used suspensions and buffer solutions were analyzed by using ICP-OES, but no traces of copper were found. Hence. It was suspected that the contamination was coming from the impurities deposited on the tip of the holder. Thus, further experiments are needed to verify optimal parameters that were discussed using *in silico* in Chapter 3.

The projected size of PMS was observed to shrink when it was irradiated in an empty liquid cell filled with air. This seems to be in accordance with an earlier cryo-EM study, where polystyrene spheres were observed to shrink when embedded in ice. When the cell was filled with liquid, particles gradually disappeared from the field of view. We interpret this so that PMSs also shrank in the liquid. However, we cannot rule out the possibility that the effective density of PMS decreased, and this caused diminishing size in the image analysis of low SNR data [138]. For PMS in liquid, it was observed that it is required  $D_e$  of 30-50 e<sup>-</sup>Å<sup>2</sup> in order to introduce shrinking of 10% in the projected diameter of PMS. Based on the literature survey, the expected threshold for beam damage in the liquid in RT was

expected to be in the range of 120- 600  $e^{-}\text{\AA}^{-2}$ , and this can be considered a good agreement.

To explain the observed shrinking of PMS, we hypothesize that diminishing size is caused by the secondary damage where the electron beam created free radicals damage the structure from the outside. This has been observed to happen in ESEM studies [94]. We hence propose that the surface of PMS is attacked by electron beam generated radicals in the liquid or gaseous surroundings. This leads to depolymerization and subsequent shrinking of PMS. Another possibility is that the oxidized structure of PMS becomes hydrophilic and swells as the water enters the structure. This could lead to diminishing contrast, which in turn, could be interpreted as shrinking by the image processing pipeline that was used to analyze the size distribution (Appendix III, Supplementary Information).

No changes were observed in the structure of SiONP for the tested electron doses ( $< 100 e^{-}\text{\AA}^{-2}$ ). This is in accordance with [130] where elongation of particles was observed at cumulative  $D_e = 10^3 - 10^4 e^{-}\text{\AA}^{-2}$ . However, the damage to the amino functionalization was not investigated and should be addressed in future studies if dynamic experiments are conducted.

In order to image the hierarchical structure of binary particles, a low-dose imaging protocol with a high temporal resolution was used to avoid the motion blur in the images. First, a video of self-assembled binary structures in the liquid was acquired and showed rotation and gradual detachment of aggregate from the surface of the silicon nitride membrane (Fig. 4.3B). In the post-processing step, the data were aligned and averaged to improve the SNR of the data. From the acquired 2D-projection, the raspberry-structure of the binary structures can be resolved, but the visual appearance worse than what was obtained with cryo-EM [1]. From the LPEM data, it was possible to resolve some SiONP's around the PMS, but the determination of the exact number of particles was not feasible. Also, the 3D-distribution of SiNOP's was around the PMS could not be determined. The cryo-EM studies [1] enabled the tomographic construction of the 3D-model, which was not attempted in this work. An example of single-particle 3D-construction in liquid has been

presented in [25] and in principle, the same technique could be applied for this system. However, higher frame-rate videos should be obtained in order to further reduce the motion blur, and binary particles should stay in the longer period of time in the field of view so that a single particle could be imaged from several rotational positions. This implies the need for more understanding about the nano-object-membrane interaction for a controlled detachment process, where particles ideally detach, rotate, and then attach the membrane again.

Detachment processes such as observed in this work have been explained by electrostatic repulsion between the windows and the nanoparticles. The repulsion force can result from the secondary electron production that leads to the charging of the SiN<sub>x</sub>-membrane [109]. Another possibility is that the pH and ionic strength [86] changed due to the radiolysis products that were formed in the liquid volume that was irradiated. The increased ionic strength may have led to the screening of electrostatic charges [113], which promoted the attachment on the window surface in the first place. Finally, beam-induced changes in the pH might have changed interaction potential between the siloxane-terminated SiN<sub>x</sub>-surface [30] and the amino-terminated SiONP. Latter, however, assumes that the amino termination is not irreversibly damaged by the electron beam. The degradation of surface functionalization has been indeed considered a driving force for the irreversible aggregation of gold nanoparticles [109, 111]. In the case of SiONP, the removal of amino groups would result a negatively charged silica-surface. Hence another plausible explanation for the observed detachment is that both the SiN<sub>x</sub>-membrane and SiONP became negatively charged due to the electron beam. Also, the possibility that electron beam led to a sudden disintegration of the binary structure is possible. In Fig. 4.3D, some SiONPs stay in the field of view after the binary structure has detached. This could indicate that the binary structure was destabilized under electron irradiation.

When the DF-STEM and BF-TEM imaging modalities were directly compared in similar conditions, DF-STEM gave more visually appealing results where the expected raspberry-structure [1] was resolved. The BF-TEM images seemed to show a degree of astigmatism that can be perhaps improved by adjusting the astigmaters of post-specimen lenses.

Interestingly, when the BF-STEM was used to image binary structures, they stayed immobilized on the window. This is in contrast to DF-STEM, where particles detached rapidly and became blurred due to their motion. Elsewhere [5], it has also been reported that the imaging of AuNP using STEM induced movement of AuNP, while under constant illumination of TEM, motion blur was not observed.

#### **4.4 Conclusions**

It has been demonstrated that assemblies of low-Z colloidal particles can be imaged in a liquid cell with nearly nm-resolution. Experimental contrast agreed within a factor of two with the MC-simulations and analytical calculations. The structure of PMS is damaged by the electron beam, and this will likely limit the acceptable  $D_e$ , and thus the obtainable resolution in liquid. The raspberry-structure of binary particles was resolved when using DF-STEM. The resolution in the images was limited by the movement of the particles, and thus only a limited amount of information was present compared to the cryo-EM data presented elsewhere [1]. Finally, the need for clean equipment and holder system needs to be stressed. The electron beam can reduce metallic ions into bright artifacts that overwhelm the contrast of low-Z materials and could potentially lead to misinterpretation of data.

## Chapter 5. Fresnel-contrast imaging in liquid

*“How can Fresnel-contrast improve the visibility of SiO<sub>2</sub>-nanoparticles in liquid?”*

### 5.1 Introduction

Fresnel-contrast in EM images is a type of phase-contrast that forms when there is an abrupt change in the projected mean inner potential of the sample [8]. The most typical example of Fresnel-contrast are fringes that are found around the edge of an aperture or a film of holey carbon. Fresnel-fringes are a result of near-field (Fresnel) diffraction observed at typical the defocal distance ( $\Delta f$ ) from the sample. This is in contrast to diffraction experiments in electron microscopy in which the rules of far-field (Fraunhofer) diffraction are used to understand the pattern formation on the detector.

Fresnel-fringes have been used, for instance, to image interfaces [149] and cavities[150]. For modeling the shape and width of the fringe, computational modeling is required [151]. In LPEM, Fresnel-contrast has been used to image nucleation of electron beam-induced bubbles at the liquid-solid interface of a liquid cell [79].

In this work, we are interested how the Fresnel-contrast can improve the resolvability of 25 nm SiONP particles in a liquid cell. First, in which conditions does the Fresnel-contrast appear in terms of defocus ( $\Delta f$ )? As  $\Delta f$  has an effect on the appearance of fringes around the particles, it is expected that an optimal value of  $\Delta f$  should exist. Johnson & Crawford [152] proposed that for repeating structures with a separation  $r > 1$  nm, the optimal value of  $\Delta f$  is given by

$$\Delta f = \frac{r^2}{32\lambda} \quad (\text{Eq. 5.1})$$

Secondly, we were interested in how the Fresnel-contrast can be used in practice to give more information about the colloidal system when compared to, for example, BF-STEM, where no Fresnel-contrast is present.

Multiple scattering in a thick specimen will degrade any type of phase contrast, and hence it has been proposed that for effective phase-contrast imaging, the sample thickness should be below half of the elastic mean free pathlength of the material, thus corresponding approximately  $\sim 160$  nm of liquid excluding the windows [103]. Recent advances in holder design have made it possible to reduce the liquid thickness in a controlled manner so that the average liquid cell thickness is in the range of 200-300 nm when using 200 nm spacer [5]. The novel pressure-controller setup developed by Dr. Sercan Keskin was an essential tool for the acquisition of these results.

**A remark about contributions: Peter Kunnas planned the experiments and proved the feasibility of the experiment by recording Fresnel-fringes around articles and measuring the liquid thickness. Peter Kunnas recorded and analyzed the data in Fig. 5.2- Fig. 5.4. Dr. Sercan Keskin developed the pressure controller setup, acquired, analyzed, and compiled the data shown in Fig. 5.1.**

## 5.2 Results

### 5.2.1 Thinning the liquid layer

The pressure controller was tested in order to demonstrate its capability in thinning the liquid cell. Two microchips with  $\text{SiN}_x$  thickness of 50 nm, one with 200 nm spacer, were plasma cleaned for 5 minutes. In order to create a monolayer of colloidal particles on the bottom window, 0.5  $\mu\text{l}$  of 20 nm diameter, citrate functionalized-Au nanoparticles (AuNP) (Nanopartz, USA) was pipetted on the chip, after which the chip was rinsed with HPLC-water. After air-drying the chip, it was placed on the bottom of the liquid cell holder, and the system was sealed by placing a chip with 200 nm on top. The sample holder was loaded into the microscope, raised to the eucentric height, and imaged first in the dry state (not shown). This was followed by flowing 10% PBS into the cell by using a syringe pump with a flow rate of 20  $\mu\text{l min}^{-1}$ . After 5 minutes, the cell was completely filled with liquid (Fig. 5.1A), and the first thickness profile was measured (here, 1 bar corresponding to ambient atmospheric pressure). The inner pressure of the system was decreased step-

wise, and the thickness profile was measured repeatedly. As a result, the average liquid thickness was reduced from 0.72  $\mu\text{m}$  to 0.23  $\mu\text{m}$  (Fig. 5.1B). The systematic error of the EELS log-ratio method was estimated to be less than 20 % [124], however, recent results obtained from electron holography indicate that the error could be as much as 50 % for liquid water [125].

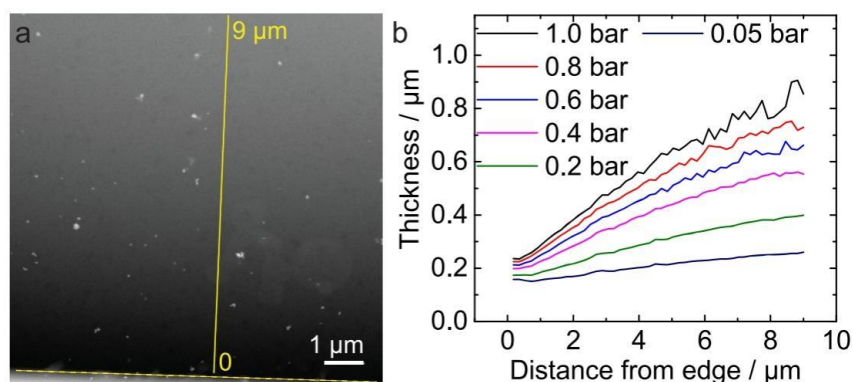


**Figure 5.1 Reducing liquid cell thickness by lowering the inner pressure of the LPEM holder.**

A) 20 k $\times$  DF-STEM image of a liquid cell after flowing in the liquid. The horizontal line indicates the edge of the SiN<sub>x</sub>-window, and the vertical line marks the 9  $\mu\text{m}$  line scan along which the thickness profile of the cell was determined by using EELS log-ratio method. B) Thickness profiles of the cell plotted decreasing values of inner pressure. Reprinted with permission from [5]. Copyright 2019 American Chemical Society.

### 5.2.2 The effect of defocus on the appearance on SiONP-assemblies

A set of experiments was conducted for more insight into how  $\Delta f$ ,  $D_e$ , and the OLA diameter affect the recorded Fresnel-contrast of SiONP in a thinned layer of liquid. The new sample was prepared in a similar manner as what was described above, however, instead of AuNPs, SiONPs were deposited on the top window. In addition, the injected liquid was 44 mM solution of NaCl. After the liquid had filled the window area of the liquid cell, the pressure controller was set to 0.05 bar. The resulting liquid  $t/\lambda$  was determined to be, on average 2.1 corresponding to 240 nm of water. An aggregate of SiONPs was centered in the field of view, and multiple series of 10 images were recorded while adjusting the value of the  $\Delta f$ . The nominal magnification of 2500 $\times$  was used, resulting in  $s =$

0.48 nm. In the post-processing step, the obtained image stack was aligned to remove the effect of specimen drift. Aligned data were then averaged to give a total  $D_e$  of  $70 \text{ e}^{-\text{\AA}^{-2}}$ .

Visual inspection of images shown in Fig. 5.2A revealed that the edges of the individual particles became more pronounced as  $\Delta f$  was made slightly negative ( $-5 \mu\text{m}$ ). Secondly, as the magnitude of  $\Delta f$  increased, the blurring of detail became evident in the images. Insets of the panel A) show the FFT of each corresponding image. FFT's were cropped to show the concentric ring-structure evident, especially at  $\Delta f$  values of  $-17$  and  $-25 \mu\text{m}$ . For a more detailed analysis of the evolving Fresnel-fringe, a profile plot was extracted across a single particle (panel B). This confirms that the Fresnel-fringes grew in width and intensity. The average SNR of five SiONP (small yellow dots in panel A) was measured and calculated, as was described in Chapter 3. The particle SNR is plotted in panel C of Fig. 5.2 and shows that the highest SNR is achieved at  $\Delta f = 0$ .

If the structural detail of a colloidal assembly is to be studied, it is crucial to recognize adjacent particles from each other. Thus, the resolvability of adjacent SiONPs particles was studied. A line profile was extracted from a row of four adjacent SiONPs indicated in panel A). The average intensity of three adjacent gaps was manually measured as well as the average intensity value measured over each particle (dashed horizontal lines on panel D). In order to calculate the SNR of the interparticle gap, the difference of average maximum and minimum values was divided with the standard deviation of the background measured at the area indicated as "BG" in panel A. The calculated SNR of the interparticle gap is plotted in panel E), and the result indicated that maximal SNR was achieved by at  $\Delta f = -17 \mu\text{m}$ .

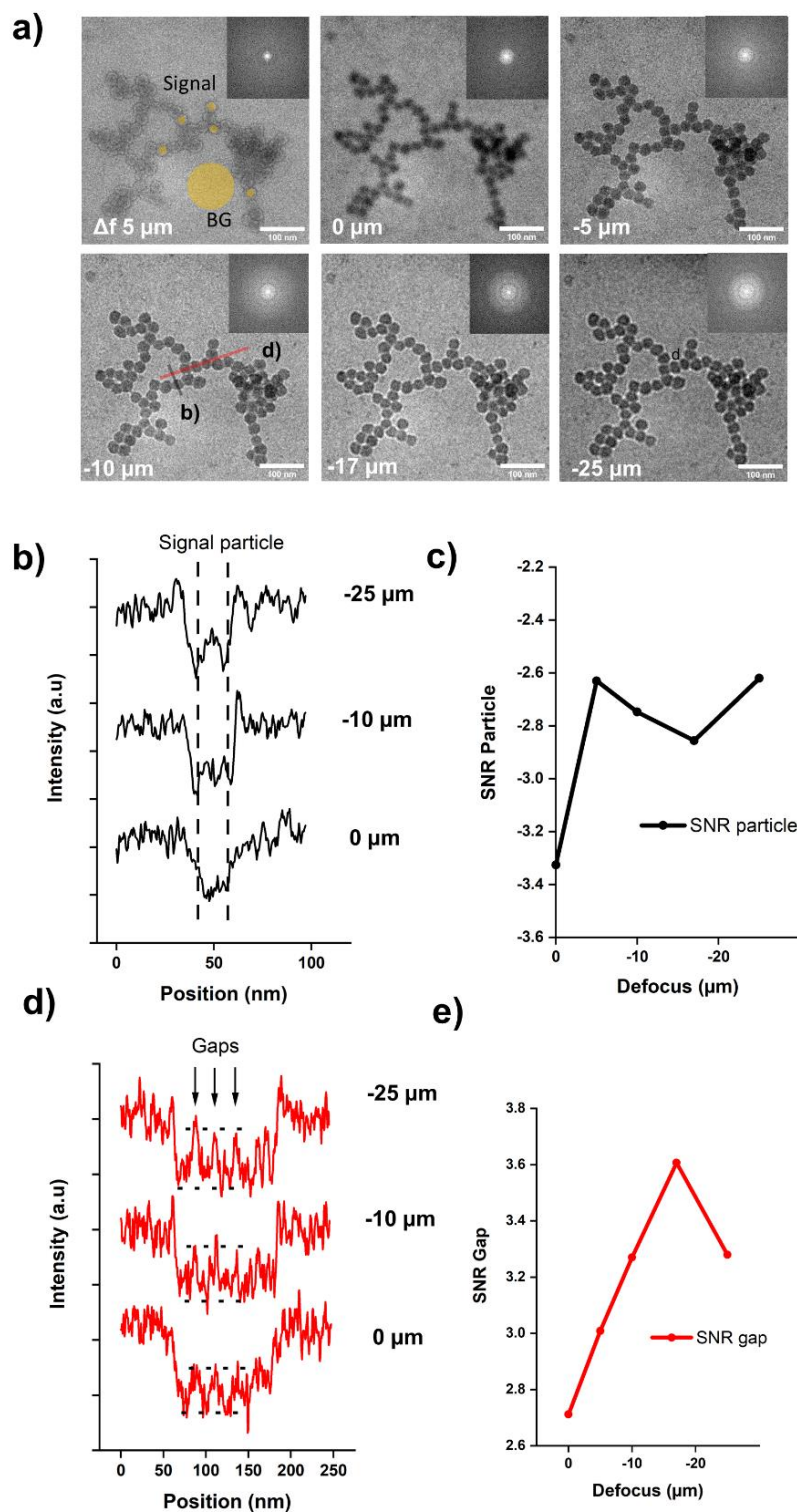


**Figure 5.2** The effect of defocus on the appearance of SiONP and its assemblies in 250 nm of liquid. In A) A focal series of SiONP in a liquid cell was acquired with defocus ( $\Delta f$ ) ranging from +5 to  $-25 \mu\text{m}$ ,  $D_e = 70 \text{ e}^- \text{ \AA}^{-2}$  and  $s = 0.48 \text{ nm}$ . Blue and black lines show locations where line profiles were acquired (averaged over the width of 5 pixels). The five small, yellow circles (“signal”) represent 15 nm wide regions where the SiONP signal was measured in Image. The

larger circle (“BG”) represents the area where the background signal intensity and its standard deviation were measured. The inset shows the cropped fast Fourier transform (FFT) of the corresponding image. B) Profile plots over a single particle for three different  $\Delta f$  values are shown. Dashed vertical lines illustrate the size of the 15 nm mask that was used to measure the signal. C) The average SNR of five SiONPs plotted against the  $\Delta f$  value (Black). In D), the profile plot over a row of three adjacent SiONP. The distance between dashed, horizontal lines indicates the average signal for the interparticle gap, which was manually measured in ImageJ. In E), the SNR of the interparticle gap is plotted as a function of  $\Delta f$ . The scale bar in panel A 100 nm.

### 5.2.3 The effect of the objective lens aperture on the appearance of SiONP

The amount of scattering contrast observed in images depends on the  $\alpha$ , which is determined by the physical size of OLA. Hence, it was tested how the relative intensity of Fresnel-fringes changed when the  $\alpha$  decreased. In addition, the average SNR of five particles was measured as a function  $D_e$  for three values of  $\alpha$ . Finally, the SNR of the interparticle gap was measured manually, as was illustrated in the previous section.

For the experiment, the  $\Delta f$  was adjusted to  $-10 \mu\text{m}$ , and sequences of 10 images using  $D_e = 7 \text{ e}^{-\text{\AA}^{-2}}$  were acquired by varying  $\alpha$  to 64, 32, and 11 mrad. Resulting images were cropped so that that the shadow of the smallest OLA (11 mrad) was excluded, and a field of view of approximately  $0.4 \mu\text{m}$  resulted in images shown in Fig. 5.3A. The line profile of a single particle for  $D_e = 7 \text{ e}^{-\text{\AA}^{-2}}$  is plotted in panel B). Here, the relative intensity and width of the Fresnel-fringe increases as the  $\alpha$  decreases. The average SNR measured again over five particles was plotted as a function of cumulative  $D_e$  for three different values of  $\alpha$ . Curves reveal approximately a two-fold increase in the SNR of a SiONP when reducing the  $\alpha$  from 63 to 11 mrad and a factor of 1.5 increase in SNR when reducing the collection angle from 63 to 32 mrad.

Finally, the effect of  $\alpha$  on the SNR of the interparticle gap was tested. A line profile extending over particles is plotted so that the y-axis shows the actual image intensity recorded by the camera screen (Fig. 5.3D). The smallest objective lens aperture decreases the total intensity measured at the detector with a near factor of 6 compared to the largest aperture. The average signal of the interparticle gap was manually measured as

described earlier, and the SNR is plotted in Fig. 5.3E. Maximum SNR for the gap between the particles was obtained by using the  $\alpha = 32$  mrad. Visual inspection, however, suggests that the gaps are better resolved by using the smallest aperture  $\alpha = 11$  mrad.

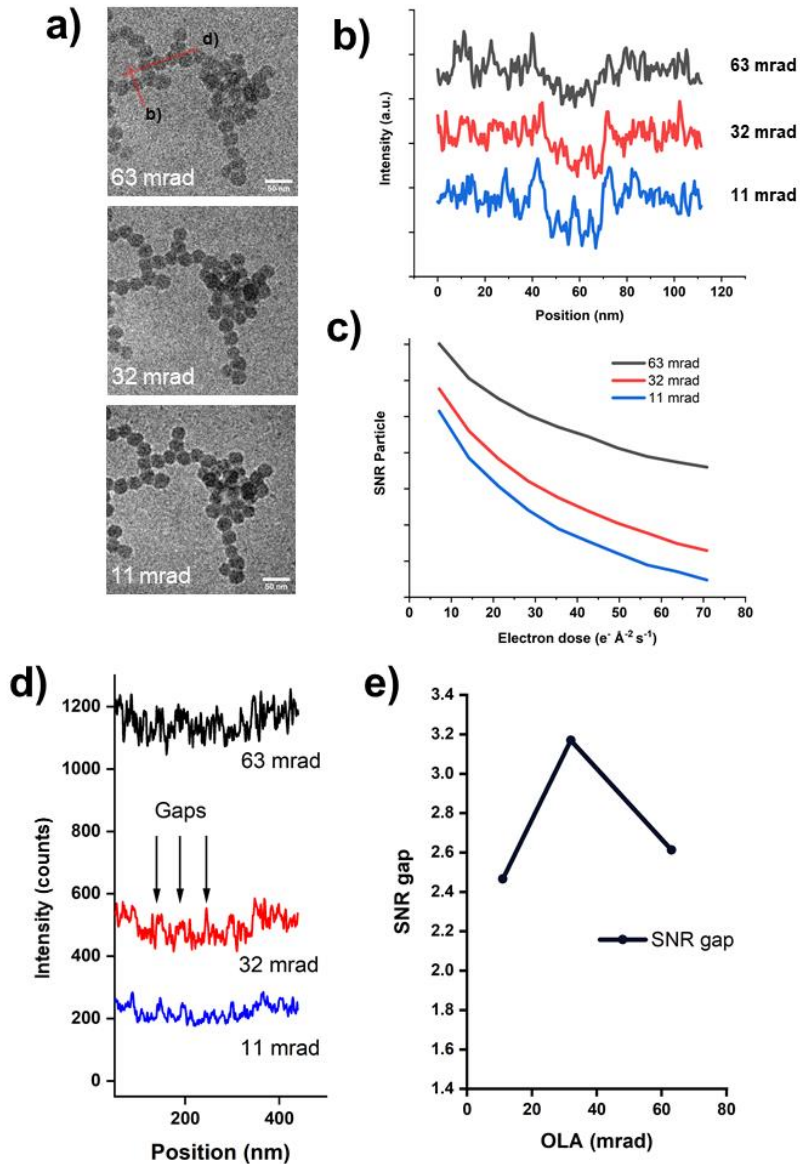


**Figure 5.3** The effect of the objective lens aperture (OLA) appearance of SiONP and its assemblies. In A) SiONPs imaged in  $t = 250$  nm using  $\Delta f = -10$   $\mu\text{m}$  and  $D_e = 7$   $e^- \text{Å}^{-2}$  using three different OLA opening angles. Red lines indicate the locations where profile plots (width 5 pixels) were extracted. In B) the profile across a single particle when varying the OLA opening angle. In C), the average SNR of five SiONP was calculated as a function of  $D_e$  and plotted of all OLA opening angles. In D) The profile of three adjacent SiONP is plotted. Notice the reduction in the number of total counts when OLA opening angle is reduced. In D), the Average SNR of three gaps is plotted against the OLA opening angle.

#### 5.2.4 Putting Fresnel-fringes in work: Comparing Fresnel-contrast imaging with BF-STEM

So far, we have shown that phase-related contrast is present in images of SiONP in 200-300 nm thick layers of liquid. Fresnel-fringes grow in intensity and in width when the  $\Delta f$  is increased. However, increasing defocus did not increase the average contrast of SiONP against the liquid background. However, we do see an increase in the contrast of the interparticle gaps. Now the question remains in which way, if any, the Fresnel-contrast could improve the quality of data when compared to STEM, where no Fresnel contrast is present?

For this, we wanted directly to compare the effect of binning on the experimental TEM data and simulated STEM data.

TEM data was shown already in Fig. 5.4A ( $\beta = 11$  mrad,  $D_e = 7 \text{ e}^{-\text{\AA}^{-2}}$ ) and was compared with BF-STEM data that was simulated in the Casino-software with  $\alpha = 7.1$  mrad,  $\beta_{\text{in}} - \beta_{\text{out}} = 0-9$  mrad, and  $t = 240$  nm. The pixel size used was 0.48 nm, and  $D_e$  was set to 7, 14, and 21  $\text{e}^{-\text{\AA}^{-2}}$ . The experimental and simulated data was binned by using the “Scaling”-function of ImageJ. The scaling factor of 0.5, 0.25, 0.125, 0.0625, and 0.03125 resulting binning of 2, 4, 8, 16, and 32 and pixel size of 0.96, 1.92, 3.84, 7.68, and 15.36 nm, respectively as shown in the Fig. 5.4A, the performed binning consistently improved the visibility of SiONP in simulated STEM data, while the experimental TEM data was affected less. By judging visually, the TEM data start losing detail above the binning of 8 corresponding to pixel size of 3.84 nm. In panel B of Fig. 5.4 the SNR measured from the center of particles is plotted for different values of binning. In panel C, a line profiles over rows of particles imaged in TEM are shown. In panel D, the SNR of the interparticle gap was plotted against the binning number and corresponding pixel size. For experimental TEM data, it was possible to measure the signal until the binning of 16 and for simulated STEM data until the binning of 8. Above these numbers, the location of the gap was not distinguished from the background, and therefore adjacent particles had “merged” together.

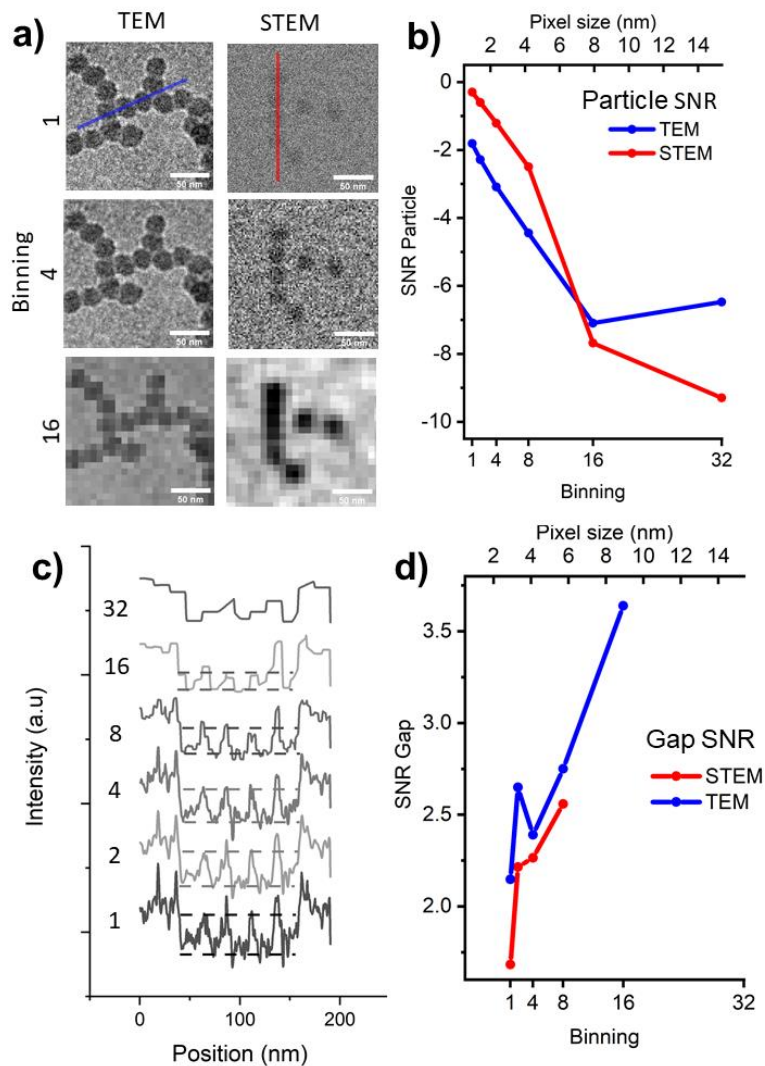


**Figure 5.4** The effect of binning on the appearance of SiONP and its assemblies in experimental BF-TEM and simulated BF-STEM data. On the left column of the panel A), experimental TEM data acquired in  $t = 250$  nm using  $\Delta f = -10$   $\mu\text{m}$  and  $D_e = 7$   $\text{e}^{-\text{\AA}^{-2}}$  and OLA opening angle of 11 mrad and binning values of 1, 4, and 16 pixels. On The left column shows BF-STEM data simulated for  $t = 250$  nm,  $D_e = 7$   $\text{e}^{-\text{\AA}^{-2}}$ ,  $\alpha = 7.1$ , and  $\beta = 9$  mrad. In B), the average SNR of five (TEM) and three (STEM) SiONPs is calculated and plotted against the number of binned pixels. Panel C) shows the profiles of SiONP row for a different number of binned pixels. Horizontal lines represent the average signal for interparticle gaps between the particles. In D), the SNR of Gap has been plotted against the number of binned pixels.

### 5.3 Discussion

The use of phase contrast for imaging colloidal SiONP in a SiN<sub>x</sub> liquid cell containing 200-300 nm of water was investigated. Changing the  $\Delta f$  resulted in changes at the outlines of SiONP, indicating that Fresnel-contrast is present in images. The resolvability of single particles, judged by the SNR, did not improve by increasing the  $\Delta f$ . However, the resolvability of the gap between adjacent particles did improve.

In order to record phase-related effects in LPEM, the thickness of the liquid was minimized. The combination assembling the liquid cell “in air” [24] and the flowing liquid into the dry, plasma-cleaned cell, and finally reducing the inner pressure resulted in controllable liquid thickness in the range of 0.23-0.7  $\mu\text{m}$ . This proved that by using the pressure control system (by Dr. Sercan Keskin) in combination with the “in air” sample loading, it is possible to achieve large areas of a sample thickness corresponding to approximate spacer thickness. In thinned layers of liquid, phase-related effects became visible for SiONP when  $\Delta f$  was adjusted to larger values. First, the overfocus blurred the detail of the SiONP, and secondly, Fresnel-fringes appeared around the particles. A similar effect in liquid has been observed in [153], where Immunoglobulin G molecules were imaged in a thin liquid layer.

Fresnel-fringes visible around SiONPs in defocused images are an indication that there is phase contrast present in the system [8]. However, overfocusing the objective lens at the tested range did not increase the SNR of individual particles. One way to understand this is that despite the Fresnel-fringes, amplitude contrast is dominating the transfer of information at the spatial frequencies corresponding to SiONP.

The SNR of the particle, as well as the interparticle gap, increased when  $\alpha$  was decreased. Changing  $\alpha$  from 63 to 32 mrad increased the average SNR of a SiONP with a factor of 1.5 and made the Fresnel-fringe around the particle more prominent. Changing OLA to 11 mrad further increased the SNR, but also limited the field-of-view to 0.4  $\mu\text{m}$ . Last, it was demonstrated how Fresnel-contrast could be used in practice to improve the data acquisition for imaging SiONP -assemblies in liquid. This was done by investigating the

effect of the binning to experimental TEM data and simulated STEM data. Results indicate that increasing the effective pixel size by binning improves the visibility of SiONP of simulated STEM data. However, increasing the binning above 8 caused adjacent particles to merge together. When binning was tested on experimental TEM data, adjacent particles were still be recognized at the binning of 16.

The optimal defocus value for imaging assemblies of 25 nm SiONP based on [152] (Eq. 5.1), is  $-8 \mu\text{m}$ . Based on the analysis and visual inspection of data presented in Fig. 5.2, the gap between the particles was best resolved by a somewhat larger defocus around  $-17 \mu\text{m}$ . This can be considered as a good agreement as the equation was offered to be a rule of thumb.

In the end, we were left with the question of how Fresnel-contrast can be used to improve the data acquisition when imaging SiONP or it's assemblies in liquid. As was shown in Fig. 5.2B, the average SNR of an individual particle did not improve when  $\Delta f$  in increased, but the average SNR of interparticle gaps did improve to some extent. The acquisition in LPEM is often accomplished as low  $D_e$  as possible in order to avoid unwanted electron beam effects. This leads to increased noise. One way of decreasing the amount of noise is to average adjacent pixels in the image by using binning. Alternatively, larger pixel size can also be set for the data acquisition, as was done in [110] to improve the temporal resolution for imaging unhindered Brownian motion of titania nanoparticles in liquid phase STEM. As was shown in Chapter 3, binning reduces the amount of noise and can hence improve the visibility of multi-pixel objects. Binning by a factor of 2 will increase the area of the pixel with a factor of  $2^2$ . Thus, according to Eq. 3.15, binning by a factor of two, should result in a two-fold increase in the observed SNR ( $\sqrt{2^2} = 2$ ). As a downside, the binning also decreases the maximum achievable resolution by increasing the size of the pixel of the image, and eventually, features in an image start merging together. Based on the results presented in Fig. 5.4, Fresnel-fringes may offer a way to discriminate between adjacent particles at higher values of binning than what was found for MC- simulated in-focus STEM-data. This comparison is by no means extensive and cannot be used to rule whether STEM or TEM is better for imaging colloidal assemblies in  $t = 200\text{-}300 \text{ nm}$ .

However, it should be able to communicate the idea of how Fresnel-contrast imaging could be used as a part of the low-dose imaging protocol in LPEM studies of colloidal assemblies.

#### **5.4 Conclusions**

To conclude, recent developments in the sample preparation methods in liquid cell electron microscopy have made it possible to observe phase-contrast effects when recording images of low atomic number colloids in  $\sim 200$  nm of liquid. At the beginning of this work, it was unclear how phase-contrast could be utilized in low-to-medium magnifications without using a phase plate [66]. It was found that Fresnel-fringes around particles may improve the quality of data, especially if the interest is on resolving morphological details of closely packed assemblies of colloidal particles. In order to address the challenge of dealing with low SNR data often encountered in low-dose imaging, it was also hypothesized that Fresnel-fringes might help to preserve structural details when images are binned in order to reduce the noise in the image. For future studies, it would be interesting to attempt imaging these assemblies by using an order of magnitude lower  $D_e$  than what was done in this work ( $D_e = 7 \text{ e}^{-\text{\AA}^{-2}}$ ). Moreover, the use of the pressure controller might allow direct experimental comparison of available imaging modalities (BF-STEM, BF-TEM, and Energy-filtered TEM) in order to confirm optimal modality for low sample thicknesses where effects of phase-contrast are readily visible.

## Chapter 6. Improved cell design for imaging colloidal assembly in a liquid cell

*“How can the colloidal mass-transport be facilitated in a liquid cell?”*

### 6.1 Introduction

It has been proposed that molecular simulations and direct imaging technologies could be in an important role in the future for giving insight into how the self-organization of nanoscale objects takes place in liquid and related systems [101]. In order to observe the dynamics of colloidal self-assembly in a liquid cell, an adequate number of freely moving colloidal particles is required in the volume of liquid that is studied. It is a common observation that nano-objects are pinned to the solid-liquid interface after they are loaded into the liquid cell. The electron beam typically facilitates the movement of the nano-objects, making it possible to observe dynamics [106] and self-assembly processes [22]. Often it is desirable to extrapolate the LPEM results to the bulk conditions where neither electron beam nor confinement is present. Thus, it would be optimal if colloidal dynamics could be observed independently of the electron dose, and the mass-transport would be governed by diffusion and convection as in a bulk liquid.

While diffusion is powered by the random thermal movement of the liquid molecules, convective flow requires a pressure difference that causes a directed movement of the liquid [154]. Both of these processes, however, are affected in a liquid cell. Brownian motion of nano-objects is affected by the attractive forces with the walls of the liquid cell [87, 109]. In addition, an ordered liquid layer next to the walls has been hypothesized, where diffusion is orders of magnitude slower than in bulk [106]. The convective flow in a liquid cell is hindered by the geometry of the cell. The effect has been modeled by means of analytical calculations in microchannels of 6  $\mu\text{m}$  in height [26] and physical simulations for nanochannels of 200 nm height [25].

In Chapter 4, it was observed that maintaining a 10-minute, continuous liquid flow of SiONP suspension through the liquid cell holder did not result in any observable amount of NP's in the imaging area. Waiting for 1h after cutting off the flow did not result in any visible number of particles either (Fig. 4.1C). This is in contrast to the observations made in [26], where colloidal particles appeared at the field of view some minutes after starting the syringe pump used for injecting the nanoparticle suspension to the tip of the holder. Thus in Chapter 6 of this thesis, we are interested in understanding why the movement of colloidal particles was hindered in the liquid cell and how a recently patented [6] liquid cell design could alleviate encountered problems.

To summarize, colloidal nano-objects are routinely examined with LPEM, but their dynamics and availability in the liquid cell are affected by the high surface-to-volume-ratio of the liquid cell. Here, our first goal is to analyze the underlying causes of colloidal hindrance by directly comparing the colloidal assembly process in bulk liquid and in the confinement of the liquid cell. Based on these results, a new liquid cell design will be tested in order to improve the colloidal mobility and availability in liquid cell electron microscopy.

## 6.2 Results

### 6.2.1 Colloidal assembly in bulk

Our first goal was to characterize the effects of confinement on the availability of SiONP in a standard liquid cell. For this, a simple colloidal system exhibiting the formation of self-assembled monolayer (SAM) was selected where SiONPs spontaneously adhere to the SiN<sub>x</sub>-surface and where no confinement is not affecting the measurement. The experiment was conducted by using a freshly (< 1 h) plasma cleaned SiN<sub>x</sub>-surface (2 mm × 2.6 mm), which was immersed into a suspension of either 1:5 diluted SiONP in PBS pH 2 or pH 7. Used incubation times were 1, 10, and 30 min, after which the surface rinsed in HPLC-grade water. Next, the surface was blotted dry with a piece of lint-free tissue and imaged in SEM with a magnification of 240 k $\times$ . The surface coverage ( $\Theta_{\text{SiONP}}$ ) of SiONP on the SiN<sub>x</sub>-

surface was determined by acquiring SEM images from 5 randomly selected locations from two samples, which had been prepared in parallel using the same conditions. Hence, total 10 images (Fig. 6.1A) were analyzed in ImageJ to measure the ratio of the projected surface area of SiONP coverage and bare SiN<sub>x</sub>. First, images were convoluted with the “Gaussian Blur”-function using kernel diameter of 4 pixels in order to reduce the noise. Next, pixels representing SiONPs on the sample was segmented by using the “Threshold” function. The lower limit for the threshold was manually set to a histogram position of local minima, where the populations of background pixels and pixels representing SiONP overlap. The surface area of the SiONP-covered sample surface was obtained by the “Measure”-command. The  $\Theta_{\text{SiONP}}$  was calculated by dividing the segmented area by the total area of the image (Fig. 6.1B). First, results show that the surface adsorption process takes place in less than one minute, after which the equilibrium has been achieved. Secondly, it appears that the pH has a strong influence on the surface coverage of SiONP. At pH 2 the average  $\Theta_{\text{SiONP}} = 0.7$ , and at pH 7 the  $\Theta_{\text{SiONP}} = 0.2$ . Presumably, the SiN<sub>x</sub>-membrane and amino-terminated SiONPs carry opposite charges in low pH, which favors the formation of denser SAM.

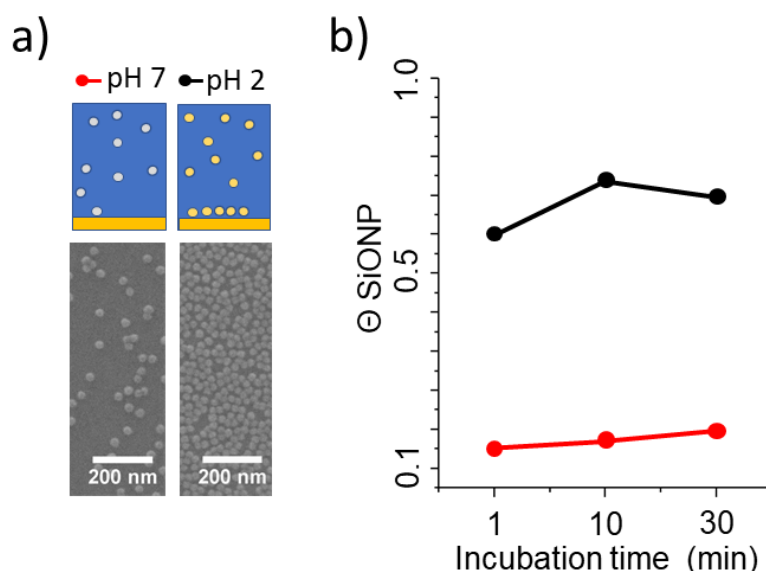


**Figure 6.1. Formation of self-assembled monolayer (SAM) in bulk .** O<sub>2</sub>-plasma-cleaned SiN<sub>x</sub>-surfaces were incubated in 100  $\mu\text{l}$  of SiONP- suspension diluted 1:5 with phosphate-buffered saline (PBS) at pH 2 and pH 7. After rinsing with HPLC- water, surfaces were blotted dry and

imaged in vacuum by using SEM. In A) it can be seen at pH 2, the resulting SAM is denser than in pH 7. In B), the surface coverage of SiONP ( $\theta_{SiONP}$ ) was measured in ImageJ and plotted against the incubation time for both values of pH. Adapted with permission from [155]. Copyright 2019 Cambridge University Press.

### 6.2.2 Colloidal assembly in the confinement of a liquid cell

Now that we had an overview of the SAM formation in bulk conditions, we wanted to test how the surface coverage is affected when the experiment is conducted in the confinement of the liquid cell. As shown in Fig. 6.2A-C, three different methods for forming the SAM *in situ* were tested. In the first experiment, direct loading was tested where 2  $\mu$ l, of 1:5 diluted (PBS pH 2) SiONP-suspension was pipetted on the bottom chip, and then the liquid cell was sealed and imaged (Fig. 6.2A). In the second case, 2  $\mu$ l of 1:5 diluted (PBS pH 7) SiONP suspension was loaded on the bottom chip, and then the liquid cell was sealed. Before the image was acquired (Fig. 6.2B), 100 microliters of PBS pH 2 was flowed through the system with a flow speed of 10  $\mu$ l/min in order to initiate the formation of SAM. Finally, Fig. 6.2C the liquid cell was assembled “in air” without liquid, and then 100  $\mu$ l of 1:5 diluted (PBS pH 2) SiONP suspension was flowed through the system, after which the sample was imaged. The formation of dense SAM was observed only when SiONP was directly loaded on in pH 2. Direct loading of SiONP in pH 7 and subsequent decrease in pH resulted in a few SiONPs in the field of view (yellow box), but no formation of SAM. In the case of panel C), no SiONP was observed in the field of view. In all cases, bright artifacts formed during image acquisition (blue circles). In Chapter 4, similar structures were found to be caused by beam-induced deposition of copper contamination at the solid-liquid interface (Fig. 4.5D-F).

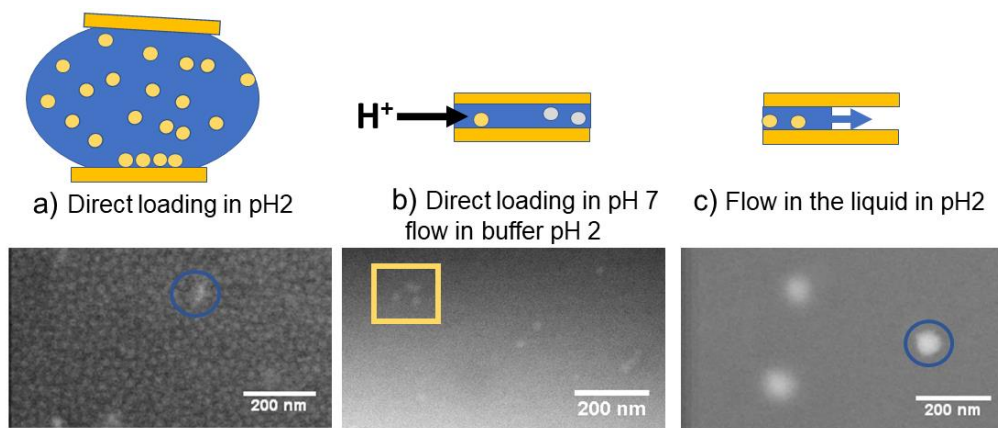


**Figure 6.2 Three different loading methods were tested to observe the SAM formation in confinement.** A) Direct loading in pH 2. B) Direct loading in pH7 and subsequent lowering of the pH by flowing in acidic buffer C) Directly flowing in the SiONP in pH 2. Only direct loading in pH 2 resulted in SAM, while individual particles were also observed in B), as indicated by the yellow square. In all of the cases, bright artifacts were observed. Liquid samples were imaged in BF-STEM mode using  $s = 3.3$ ,  $\tau = 5 \mu\text{s}$ ,  $\alpha_p = 13.4 \text{ mrad}$ , and  $\beta_{\text{in}} - \beta_{\text{out}} = 54 - 220 \text{ mrad}$ . Reprinted with permission from [155]. Copyright 2019 Cambridge University Press.

Based on the evidence shown in Fig. 6.1 and Fig. 6.2, it was concluded that the formation of SAM is hindered in the confinement of the liquid cell. To get more insight into this hindered organization, the sample from the experiment described in Fig. 6.2C was opened and rinsed in a bath of HPLC-water and blotted dry with a piece of lint-free tissue. The top chip was imaged with SEM, and the low-magnification overview image is shown in Fig. 6.3A. It seems that there is a clear border between the area closer to the edge of the chip and the area at the center of the chip (pink dashed line). Closer examination with SEM (grey boxes) revealed that the highlighted boundary is due to the formation of SAM that took place only in the vicinity of the chip edge. Lesser coverage of SiONP was found when images were acquired at the center of the cell. This indicates that SiONP immobilizes on the solid-liquid interface rapidly as it enters the confined space of the liquid cell. Furthermore, this implies that no convective flow was established in the middle of the liquid cell, which transported SiONP to the imaging area.

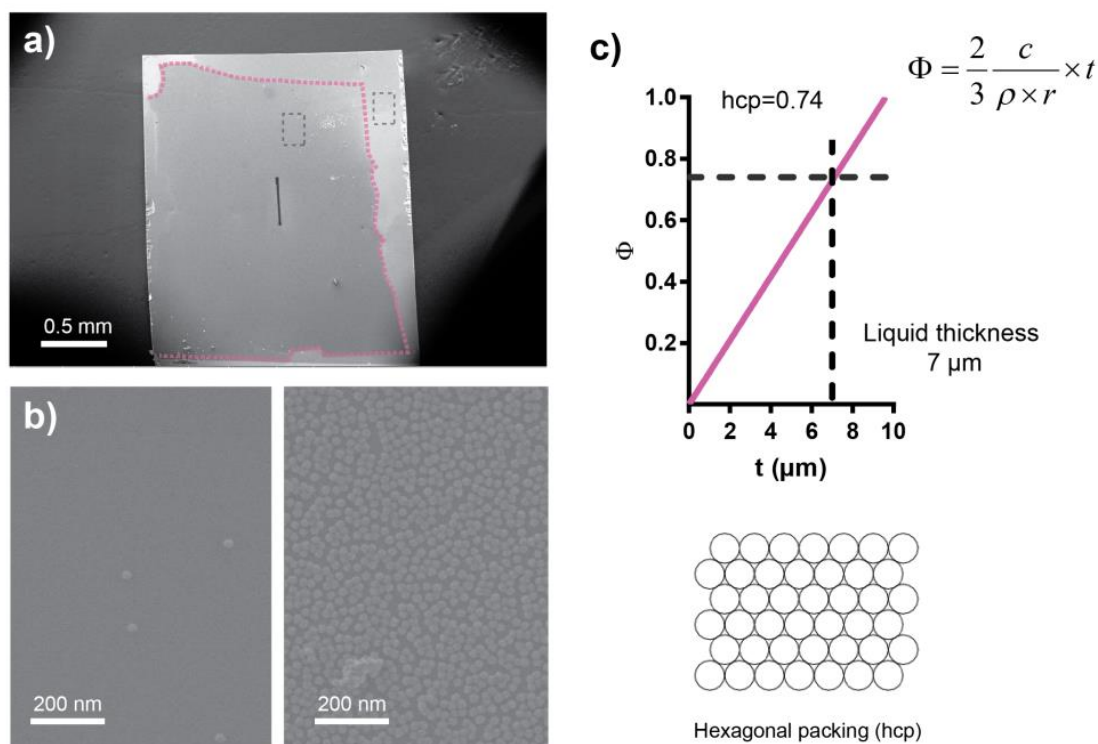


**Figure 6.3 Colloidal mobility is hindered in a standard liquid cell.** A) a low magnification SEM image of a situation after an experiment where 100  $\mu\text{l}$  (20  $\mu\text{l}/\text{min}$ ) of SiONP (pH2) has been injected into a liquid cell with a 200 nm spacer (Fig. 6.2C). B) Close to the edges, there is a higher surface coverage of SiONP compared to the area closer to the center of the liquid cell. C) To further illustrate the problem, the derived relation (Eq. 6.9) to illustrate how thick spacer ( $t$ ) is required to have a sufficient amount of colloidal species with a radius of  $r$ , the density of  $\rho$ , and mass concentration of  $c$ . Here, using values determined for your SiONP suspension ( $r = 15$  nm,  $\rho = 1.37$  g  $\text{cm}^{-3}$ , and  $c = 3.22$  g  $\text{l}^{-1}$ ) it is seen that 7  $\mu\text{m}$  spacer thickness is required to observe the hexagonal packing on both windows if flow and diffusional transport are absent.

#### 6.2.4 Why is colloidal assembly hindered in a liquid cell?

To summarize, we were not able to observe the formation of SAM when the dispersion of SiONP was injected into the liquid cell by using the in-built flow system of the commercial liquid cell holder. We believe that at least two factors are contributing to the depletion of SiONP in confinement. First, it is likely that the convective liquid flow induced by the syringe pump does not reach the middle of the liquid cell, as was also suggested in [25]. Therefore, the colloidal mass transport of SiONP is mainly resulting from the diffusive flux of colloidal particles from the bulk liquid surrounding the liquid cell.

The time scale for diffusion in a liquid cell can be evaluated by first calculating the diffusion coefficient by using the Einstein-Stokes equation [156]:

$$D = \frac{K_b T}{4\pi \eta r} \quad (\text{Eq. 6.1})$$

, where  $K_b$  is the Boltzmann constant,  $T$  is the temperature,  $\eta$  is the dynamic viscosity, and  $r$  is the radius of the diffusing object. For 30 nm SiONP in a liquid cell,  $r = 15$  nm,  $T = 293$  K,  $K_b = 1.38 \times 10^{-23}$  J K<sup>-1</sup> and  $\eta = 1 \times 10^{-3}$  Pa s resulting  $D_{SiONP} = 2.145 \times 10^{-11}$  m<sup>2</sup> s<sup>-1</sup>.

The mean square displacement ( $\langle \Delta x^2 \rangle$ ) for two-dimensional diffusion is defined as

$$\langle \Delta x^2(\tau) \rangle = 4D\tau \quad (\text{Eq. 6.2})$$

, where  $\tau$  is the time of diffusion.

The distance that a SiONP needs to travel from the bulk liquid to the window area is approximately 1 mm. By setting  $\langle x \rangle = 1$  mm, we get  $\tau = 12000$ s, which corresponds approximately 3 h for a 30 nm SiONP to diffuse 1 mm.

The second reason for seeing only a small number of SiONP in the imaging area is that there are simply not enough SiONPs in the confined volume that could form a densely packed SAM that was seen in Fig. 6.1A and Fig. 6.2A. To illustrate this, a relation between the  $t$  and  $\Theta$  was derived.

The number of SiONP ( $N_{SiONP}$ ) in a liquid cell volume ( $V_{cell}$ )

$$N_{SiONP} = \frac{c V_{cell}}{m_{SiONP}} \quad (\text{Eq. 6.3})$$

, where  $c$  is the concentration of SiO<sub>2</sub> and  $m_{SiONP}$  is the average mass of a SiONP obtained by

$$m_{SiONP} = \frac{4}{3} \pi r^3 \rho_{SiONP} \quad (\text{Eq. 6.4})$$

, where  $r$  and  $\rho_{SiONP}$  are the radius and the density of SiONP, respectively. The projected area of the SiONP ( $A_{SiONP}$ ) is given by

$$A_{SiONP} = \pi r^2 \quad (\text{Eq. 6.5})$$

The total surface area of the liquid cell composed of two chips with length  $l$  and width  $w$  is

$$A_{cell} = 2wl \quad (\text{Eq. 6.6})$$

The total volume of the liquid cell is

$$V_{cell} = wlt \quad (\text{Eq. 6.7})$$

Assuming perfect adsorption of SiONP on the walls of the liquid cell, the resulting surface coverage is obtained by

$$\Phi = \frac{N_{SiONP} A_{SiONP}}{A_{cell}} \quad (\text{Eq. 6.8})$$

After substitution of Eq. 6.2- Eq. 6.6 into Eq. 6.7, the following relation is obtained:

$$\Phi = \frac{2ct}{3\rho r} \quad (\text{Eq. 6.9})$$

, which shows that the resulting surface coverage is linearly related to the thickness of the liquid layer. The theoretical maximal packing efficiency for SiONP on the planar surface is hexagonal packing (hcp) for which  $\Theta = 0.74$ . The Eq. 6.8 was plotted as a function of  $t$  in Fig. 6.3C using the following values  $\rho = 1370000 \text{ g m}^{-3}$ ,  $r = 15 \times 10^{-9} \text{ m}$ ,  $c = 3200 \text{ g m}^{-3}$ . It can be seen that the amount of theoretically available particles required for achieving hcp is reached only when  $t > 7 \text{ }\mu\text{m}$ . The spacer thickness in the previous experiment was 200 nm, and according to the Eq. 6.9, the surface coverage of only 0.02 can be expected in case no transport of particles from the bulk liquid is taking place.

### 6.2.5 Improved chip design with a microchannel

To summarize so far, the experimental and theoretical evidence imply that the confinement of the liquid cell leads to depletion of suspended SiONPs in the volume between chips. This is likely due to the small spacer thickness, which results in too low a number of SiONP to observe dense SAM's as in bulk (Eq. 6.9). In addition, small

nanochannel dimensions result in the flow resistance that is likely higher than what was found in [26]. This leads to a situation where mass transport is governed by diffusion, which was shown to be slow in millimeter- length scales of a standard liquid cell (Eq. 6.1 and Eq. 6.2).

In order to improve the colloidal availability in the imaging area, a patented chip design [6] was tested that allows the bulk liquid to reach a distance of only some microns from the window. In addition, the length of the nanochannel is considerably shorter, which could result in smaller flow resistance [26]. The tested chip design incorporating microchannels is shown in the 6.4A-D.

**NOTE: As this work has not yet been published, all accurate measures of the chip design are excluded from this report. Furthermore, scale bars have been intentionally left out from some of the following figures.**

In the absence of the flow, the main advantage of the new cell design is that the bulk liquid is brought right next to the imaging area. The bulk liquid will act as a reservoir for SiONP, from which particles are transported to the imaging area by diffusion in a matter of seconds or minutes, rather than hours. This is because there is a quadratic dependence (Eq. 6.2) between  $\tau$  and traveled distance. Thus, reducing the diffusion length by a factor of 100, should reduce the required diffusion time with a factor 10 000. For a SiONP, this means that diffusion time will reduce to  $\sim 1$  s if the diffusion length in the nanochannel is reduced to 10  $\mu\text{m}$ .

The electron transparent window was fabricated from 50 nm-thick SiN<sub>x</sub>-membrane. Two types of chips were manufactured (Norcada, Canada). The first type is with a microchannel of triangular cross-section on both sides of the window. Microchannels extend some distance from the edge of the window. The second type of chip is a standard chip that has a microfabricated spacer chip that defines the liquid thickness shown in Fig. 6.4B (right). Before use, chips were plasma-cleaned for 5 minutes to remove organic contaminants and to ensure the good wettability of the liquid cell.

The liquid cell was assembled into a commercial holder (Ocean, DENSSolutions, Netherlands), and a leak-test was performed in a vacuum station (HiCube, Pfeiffer, Germany). No leaks were present, and the vacuum reached the level of  $10^{-6}$  Pa in a matter of minutes. Next, 100  $\mu\text{l}$  of HPLC-water was pumped through the flow inlet using a syringe pump with a flow speed of 10  $\mu\text{l}/\text{min}$ . No change in the vacuum readout was observed.

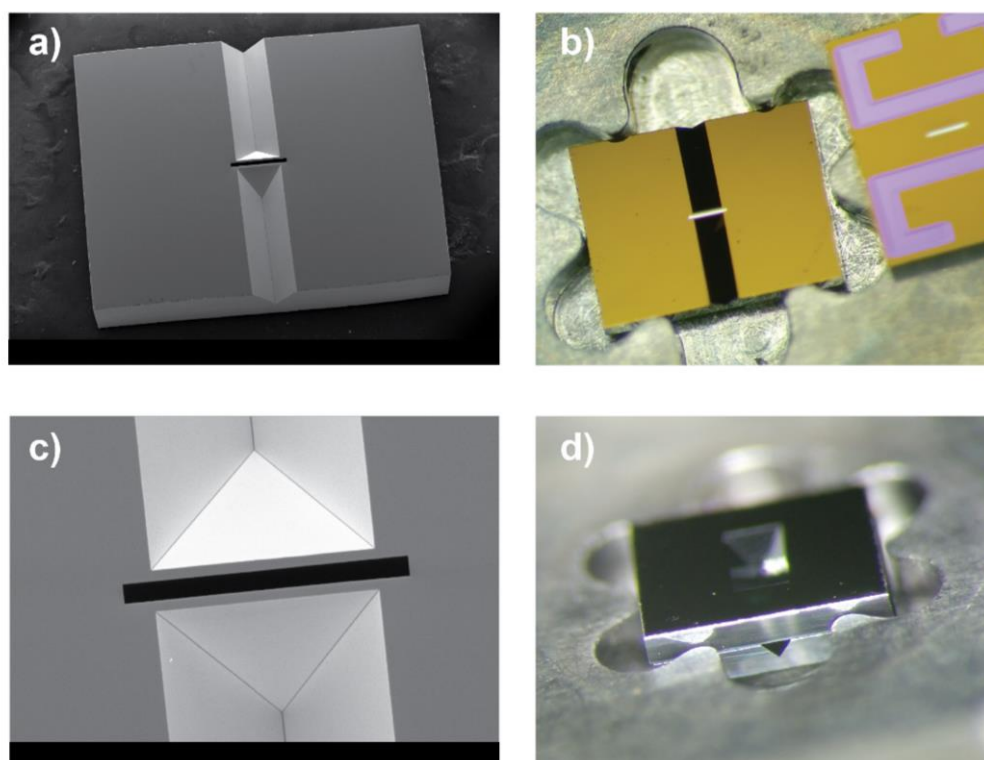


**Figure 6.4.** The new liquid cell design incorporating microchannels was based on [6]. In A), a low magnification SEM image and in B) and a photograph of the new chip design. In C), the window area is shown. Panel D) shows the microchannel chip (bottom) mounted on the DENS Ocean holder with a regular 200 nm spacer chip placed on top.

### 6.2.6 Colloidal assembly in a “microchannel” liquid cell

To evaluate the performance of the microchannel liquid cell in LPEM, two experiments were conducted to test if the colloidal availability is improved in the imaging area. In the first case, an  $\text{O}_2$ -plasma cleaned microchannel chip was placed on the bottom of the holder tip, and a regular chip with 200 nm spacer was placed on top. The cell was sealed,

and the holder was inserted into the microscope and connected it to a syringe pump loaded with 200  $\mu\text{l}$  of SiONP diluted 1:5 with 10 mM PBS, pH 2.

In order to collect 100 frames with a defined interval of 20 s, the “STEM Averager”-script for Digital Micrograph-software by Dave Mitchell (Release date 15.7.17) was used. To avoid unnecessary electron irradiation of the sample, the beam was set to automatically “park” on the silicon frame if the image acquisition was not in progress. The experiment was initiated by starting the syringe pump and image acquisition simultaneously. By using the flow speed of 20  $\mu\text{l min}^{-1}$ , a total of 60  $\mu\text{l}$  of SiONP in PBS pH 2 was flowed through the system. The liquid appeared on the window 1.5 minutes after starting the flow and was sustained for another 1.5 minutes before the syringe pump was turned off. After  $\sim 17$  minutes from starting the experiment, some aggregates were seen to move across the field of view, and the focus was slightly corrected to counteract the stage drift in the z-direction. Immediately, SiONP became visible, as shown in Fig. 6.5A where 10 consecutive frames were averaged, resulting in  $D_e = 25 \text{ e}^{-\text{\AA}^{-2}}$ . The appearance of SiONP is here seen at 34 minutes after starting the flow. Irregular high-contrast details are visible at all time points and are likely resulting from solid contamination on the membrane. The liquid thickness was determined to be  $> 750 \text{ nm}$  as we were not able to measure the inelastic mean-free path using the log-ratio-method.

After the LPEM measurement, the holder was flushed with 200  $\mu\text{l}$  of HPLC-grade water to remove freely suspended SiONP particles. Next, the cell was opened, and both chips were blotted dry with a piece of tissue followed by a *post mortem* examination with SEM. The shape of the microchannel can be clearly seen on the opposite spacer chip, which had been placed on top. (Fig. 6.5B) The shape seen in Fig. 6.5C was caused by the SiONPs that had adhered to the  $\text{SiN}_x$ -surface (Panel D).

When the examination was focused on the window, it was possible to distinguish the region where the dataset shown in panel A was acquired. The area has a square shape that is due to the lower coverage of SiONP compared to the surrounding area (Fig. 6.5E). In

addition, the edges of the exposed area seemed to be somewhat densely packed than on the unexposed area.

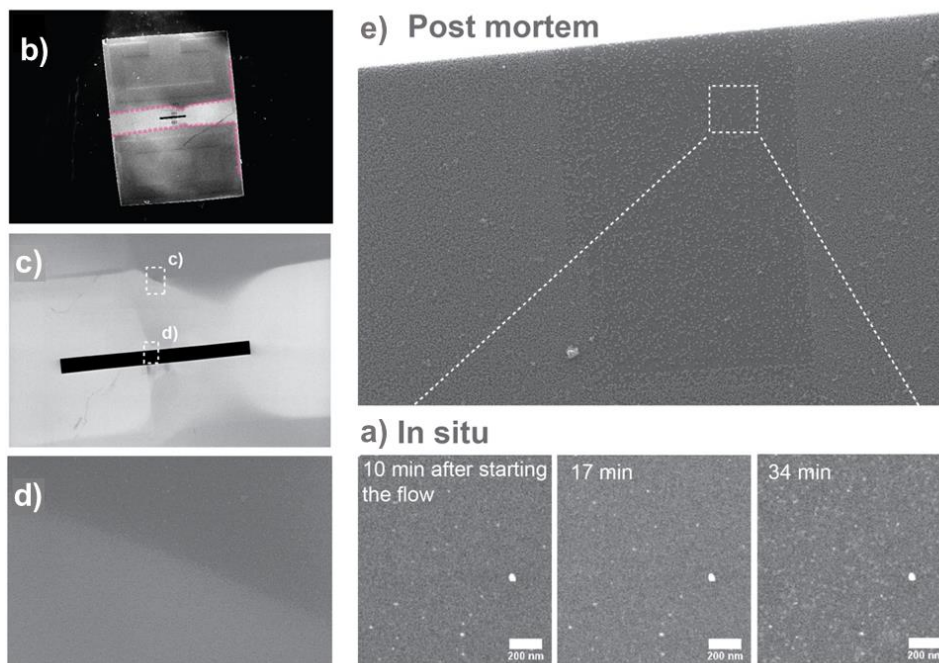


**Figure 6.5 New chip design with a microchannel allows recording dynamics of SiONP attachment on the window.** A) Shows the appearance of SiONP on the window at 34 minutes. The experiment was conducted with DF-STEM using  $\alpha_p = 13.4$  mrad,  $\theta = 54$  mrad,  $s = 3.3$  nm, and  $\tau = 5$   $\mu$ s which resulted  $D_e = 2.5$   $e^{-\text{\AA}^{-2}}$  per frame. In *post mortem* analysis (SEM), the opposite 200 nm spacer chip shows a sharp outline of the microchannel where SiONPs have formed a dense SAM, as shown in panels B)-D). In E), a *post mortem* SEM image from the window area shows the same area where the images *in situ*-experiment of A) were recorded.

### 6.2.7 Binary self-assembly in standard and “microchannel” liquid cell

Finally, an experiment was made to test is if the formation of the binary assembly can be accomplished in the liquid cell equipped with microchannels. First, PMS particles were immobilized on the  $O_2$ - plasma cleaned window of a 200 nm spacer chip. In short, we diluted the PMS suspension 1:100 with PBS and pipetted 2  $\mu$ l on the window and waited for 1 minute. After this, the whole chip was immersed into an HPLC-water path and blotted dry with a piece of lint-free tissue. The holder was assembled and sealed by placing the microchannel-chip on the bottom and the PMS-modified spacer-chip on top. The air-

dry sample was loaded into the microscope and inspected. After the presence of PMS in the liquid cell was confirmed, the recording was paused, and 100  $\mu\text{l}$  of SiONP diluted 1:5 with PBS pH 2, was flowed through the holder using a flow speed of 20  $\mu\text{l min}^{-1}$ . Due to the uneven flow, or a possible crack on the window, only part of the liquid cell was filled, and SiONP was not located evenly over the whole window area. However, from 20 minutes after starting the flow, of structure resembling PMS particles covered with SiONPs were found. Images were recorded using  $\tau = 20 \mu\text{s}$  resulting in  $D_e = 9.6 \text{ e}^{-\text{\AA}^{-2}}$  per frame. Binary structures were observed to shrink when a series of images was recorded from the same location. This agrees with the results summarized earlier in Fig. 4.2. The liquid thickness was determined to be 300 nm by using the EELS log-ratio method. In order to obtain the image shown in Fig. 6.5A, the original data were processed with ImageJ “Bandpass filter”-function to remove horizontal stripes (tolerance  $\pm 5 \%$ ) and spatial frequencies corresponding to features larger than 400 pixels.

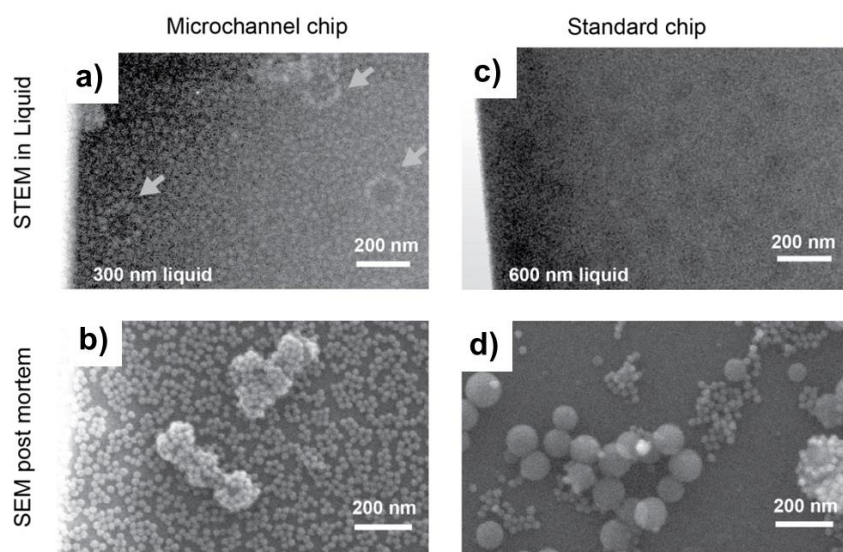


**Figure 6.6 Comparing results of binary self-assembly obtained with two different cell designs.**

In A) are shown binary structures (arrows) formed in the microchannel liquid cell imaged using  $\alpha_p = 13.4 \text{ mrad}$ ,  $\theta = 27 \text{ mrad}$ ,  $\tau = 20 \mu\text{s}$ , and  $D_e = 9.6 \text{ e}^{-\text{\AA}^{-2}}$ . In B), the sample is studied *post mortem* in SEM, showing some binary particles and dense coverage of SiONP on the surface of the window. For comparison, the sample from the experiment discussed in Fig. 4.1B and Fig. 4.2 is shown in panel C). No SiONP are seen in the presence of liquid ( $\alpha_p = 13.4 \text{ mrad}$ ,  $\theta = 54 \text{ mrad}$ ,  $D_e = 20 \text{ e}^{-\text{\AA}^{-2}}$ ). In D), the *post mortem* analysis shows some SiONP present in the window area of the opened liquid cell. However, the coverage is lower than what was seen for microchannel liquid cell in panel B).

After the LPEM experiment, the cell was opened, rinsed in a bath of HPLC water, and blotted dry. The sample was investigated *post mortem* in SEM, indicating a dense coverage of SiONP at the region of the window (Fig. 6.6B). In order to directly compare results from microchannel liquid cell with the standard liquid cell, the data from the experiment shown in Fig. 4.1B and Fig. 4.2A-F is presented in Fig. 6.6C-D. It can be seen that the microchannel liquid cell results in denser coverage of SiONP both on the PMS, and on the surface of the window.

### 6.3 Discussion

In summary, an improved microchannel liquid cell design [6] was tested in order to initiate and sustain a colloidal self-assembly reaction in a thin liquid layer. Based on the experimental and theoretical results, the colloidal mass-transport in the confinement of the standard liquid cell was facilitated mainly by diffusion, which resulted in only a limited number SiONP appearing at the imaging area during a time scale from minutes to 1 hour. When the required diffusion distance was reduced to some micrometers (the new microchannel design), evidence of effective SiONP transport to the imaging area was seen.

To characterize the performance of the liquid cell flow system to initiate colloidal self-assembly reaction, the formation of SAM on the SiN<sub>x</sub>-surface from SiONP was studied. It was found that the low pH 2 facilitated a rapid (< 1 min) formation of dense monolayers with average surface coverage  $\theta = 0.7$  while at pH 7 the observed surface coverage was found to be only 0.2. This behavior is likely due to the changes in the surface charge of the SiONP as the pH is lowered. This is supported by the  $\zeta$ -potential measurements (See Methods), where the average  $\zeta$ -potential of SiONP in pH 2 and pH 7 was reported as 14 mV and -21 mV, respectively. It is assumed that the surface charge of SiN<sub>x</sub>-membrane is negative [30], and thus, the more favorable net electrostatic interaction leads to the observed increase in the  $\theta$ . When the attachment of positively charged latex-spheres on negatively charged mica-surface was studied in [157],  $\theta$  was found to be in the order of 0.15-0.4 and dependent on the concentration of latex spheres. Elsewhere,[158], the process was described as random surface adsorption (RSA), which is driven by the attachment of particles randomly on the surface until no more particles can fit. The

theoretical “jamming limit” for RSA is  $\theta = 0.54$ , which is less than the observed in our work for adsorption in bulk. This implies that the formation of SiONP SAM on SiN<sub>x</sub>-surface is not a pure RSA-process, but SiONP’s tend to pack into higher densities than the jamming limit predicts.

When three different methods for observing the formation of SAM in confinement were tested, only the “direct loading” resulted in the formation of SAM in the imaging area. We hypothesize that this is because the SAM is rapidly formed from bulk liquid when the 2  $\mu$ l drop of SiONP is loaded on the chip. This is supported by [157], where the formation of a colloidal monolayer on a curved surface was calculated to be 11 s. However, nearly two order of magnitudes longer equilibrium times were observed in [158], where some hours were needed to reach equilibrium for the formation for colloidal SAM or planar mica surfaces.

The formation of colloidal SAM was also hindered when the sample was first directly loaded, and the SAM formation was induced by lowering the pH of the suspension inside the liquid cell. Based on the calculations, it was concluded that the number of particles was in the liquid cell was too low, and this was the reason for observing only a few particles in the field of view. According to Eq. 6.9, the observed  $\theta$  is linearly proportional to  $t$  and  $c$ . Calculations showed that a spacer thickness of 7  $\mu$ m was needed in order to observe the SAM density comparable to bulk. Another option would be to use highly concentrated solutions of SiONP’s in order to improve the availability of SiONP. The latter approach has been applied in [98], where centrifugation was used to increase the concentration of colloidal species to observe colloidal self-assembly.

Interestingly, when the liquid cell was filled with SiONP suspension using the flow system, the SAM was not formed on the window even though the liquid quickly appeared in the field of view. Similar observations were made in [25], where the loading of ferritin particles by flow was not successful. In the same study, the liquid flow in a 200 nm nanochannel was simulated, and results suggested that the flow is not sufficient in the middle of the liquid cell. This is in contrast to [26], where the loading of latex microspheres was

successful via flow when the channel height of  $6\ \mu\text{m}$  was used. It is thus likely that the liquid flow resistance becomes too high to effectively load colloidal species into the liquid cell.

In the absence of effective flow, the mass-transport in the liquid cell is governed by diffusion. Diffusion, however, is slow in macroscopic length scales due to the quadratic dependence of diffusion time on the mean displacement (Eq. 6.2).

In order to improve the mass-transport in the liquid cell, a novel cell design [6] was tested, in which the length of the nanochannel connecting the bulk liquid and the imaging area was decreased from mm-scale to some micrometers. The improvement in the diffusion time was expected to be a factor of 10 000, resulting in diffusion time of seconds instead of hours. The first tests indicated that the liquid cell design incorporating the microchannels enabled to initiate colloidal self-assembly reactions in confinement.

When the SiONP suspension (pH 2) was flowed into the liquid cell, the first SiONPs were observed to appear on the window after 17 minutes of initiating the flow. This is still three orders of magnitude longer time than what was expected on the basis of Eq. 6.2. One possible explanation for the discrepancy is that the effective diffusion velocity of the SiONP is slowed down because particles quickly adhere the nearest surface of the liquid cell when they enter the nano-channel.

When the formation of SAM was studied in the microchannel liquid cell, an important observation concerning the effects of the electron beam was made. Results indicated that the electron beam locally inhibited the formation of SAM, and this led to the sharp outline that was observed in Fig. 6.5E. We hypothesize that the electron beam permanently changed the surface properties of the window, thus preventing the formation of the dense SAM. If this had not been the case, SiONPs would have had plenty of time to adhere to the solid-liquid interface after the electron beam was moved to another location and until the cell was finally flushed with water and opened after the experiment ( $\sim 30$  minutes). A possible explanation for the reduced surface coverage is the changed surface chemistry of the  $\text{SiN}_x$ . Possibly the solvated electrons reduced silanol groups, which led to the weaker

negative surface charge of the SiN<sub>x</sub>-membrane and hence reduced attractive electrostatic force with SiONP's carrying a positive charge.

Finally, the assembly of binary structures took place in the confinement of the liquid cell. However, we did not observe the process *in situ*. Binary structures were observed after the reaction had already ended and were found to shrink likely to the depolymerization of the PMS-core, as was shown in Chapter 4.

## 6.4 Conclusions

In summary, an improved microchannel liquid cell design [6] was tested in order to initiate and sustain a colloidal self-assembly reaction in a thin liquid layer. Based on the experimental and theoretical results, the colloidal mass-transport in the confinement of the standard liquid cell was facilitated mainly by diffusion, which resulted in only a few SiONP appearing at the imaging area during a time scale from minutes to 1 hour. When the required diffusion distance was reduced to some micrometers (the new microchannel design), evidence of effective SiONP transport to the imaging area was obtained.

In future experiments, it is reasonable to expect direct observation of colloidal dynamics by using the microchannel liquid cell design. In addition, it would be beneficial to characterize the flow capabilities in the microchannel design by, for example, measuring the convective motion of nano-objects as a function of the flow speed as was done in [26]. In addition to numerical calculations [154], dedicated software could be used to model the liquid flow in the nanochannel [25].

## Chapter 7. Conclusions and outlook

At the beginning of this project, it was unclear how suitable LPEM was for studying low-Z colloidal assemblies formed out of SiONP and PMS. Also, it was unclear what type of specific information LPEM could be obtained complementary to, for example, cryo-EM studies of a similar system [1]. The expected challenges were the low inherent contrast of the sample and the beam sensitivity of the liquid suspension. Therefore, the first question was how the structure and dynamics of binary particles can be visualized using liquid-phase STEM before the electron beam irreversibly damages the sample.

In order to tackle the problem with expected low contrast, *in silico* methods (MC-simulations and numerical calculations) were used to predict the achievable SNR and/or resolution when imaging PMS, SiONP, and binary structures in a liquid cell using BF- and DF-STEM. It was possible to estimate the optimal  $\beta$ , and secondly, the required electron dose needed to resolve these nano-objects.

When the collection of experimental data started, it was surprisingly noticed that many of the images showed high contrast features appearing in the field of view that was irradiated. These were unexpected based on the results from the *in silico* methods, and subsequent elemental analysis revealed that these “bright spots” were containing mainly copper, which was not supposed to be present in the system. Thus, we hope to show that *in silico* were useful because of two reasons: First, the optimization of the data acquisition via the optimal collection angle of the detector was studied before starting the experimental work. Secondly, and perhaps more importantly, artifacts caused by metallic contamination were recognized early during the course of the work. Latter example also illustrates the importance of *post mortem* studies after an LPEM experiment.

Even if optimal imaging parameters were used, the resulting electron dose was still large enough to induce observable changes in the sample. Therefore, an acceptable electron dose needed to be determined. It was found that the electron beam caused PMS particles to shrink, possibly due to the depolymerization of the material. Depending on the sample conditions, 30-50  $e^{-}\text{\AA}^{-2}$  was enough to induce a 10 % shrink of PMS. Considering that 5-10

$e^{-\text{\AA}^{-2}}$  is needed to resolve a single SiONP in  $t = 300\text{-}600$  nm liquid cell, it is expected to be challenging to record the dynamics of binary assembly due to the beam sensitivity of the PMS. It is possible that also the amino-functionalization of SiONP is damaged to some extent by the electron beam and should be considered in future studies.

It was indeed possible to observe the structure of pre-assembled binary particles in a liquid cell while still staying below the acceptable cumulative electron dose. The ring-like structure resembled the one predicted by the MC-simulations. The image quality, however, was degraded by the movement of the particles, which disappeared from the field of view before detailed information about the SiONP distribution around the PMS-core was obtained. To promote the immobilization of the binary structures on the window, suitable chemical modification of the  $\text{SiN}_x$ -membrane and uniform illumination used in TEM should be tested in the future.

For the optimal low-dose performance of BF-TEM, it would be beneficial to enable detection via phase-contrast. The presence of phase contrast effects (Fresnel-fringes) in a thinned layer liquid was verified by studying the effect of defocus on the appearance of SiONP assemblies. It was found that large defocal values improved the visibility of interparticle gaps between adjacent SiONPs. In addition, it was found that Fresnel-fringes may potentially allow the improvement of SNR in the image data by enabling the use of larger pixel-size while still allowing to discriminate between adjacent nano-objects. In future studies, the possibility to include Fresnel-contrast imaging in a low-dose imaging protocol should be investigated.

Finally, the possibility to record the dynamics of the binary self-assembly process in a liquid cell was investigated. Here the first question was how to initiate and sustain the colloidal self-assembly reaction in the liquid cell so that it could be recorded. Early in the studies, it was observed that a very few SiONPs reached the middle of the liquid cell when the liquid flow was used for loading in the SiONPs. Control experiments where the formation of self-assembled monolayers was studied revealed that the colloidal assembly was indeed hindered in the confinement of a standard liquid cell. The main reasons for this

observation were hypothesized to be low number SiONPs in the confined liquid volume and also the slow, diffusion-driven mass-transport in the mm-long nanochannel of the standard liquid cell. To improve the colloidal availability at the imaging area, a new liquid cell design was tested, and the formation of SAM and binary particles was achieved in the liquid cell. It was found that the electron beam interfered with the formation of SAM, possibly due to the beam-induced changes of the SiN<sub>x</sub>-membrane. In the case of binary particles, the process itself was not observed *in situ*. The beam-induced shrinking was, however, found to affect the formed binary structures, which were again observed to shrink. For future experiments, it would be thus important to minimize the irradiation before the actual recording of the self-assembly has started. Another thing that requires more work in the future is to measure or otherwise evaluate the likely improvement in the flow capabilities of the new liquid cell design, which incorporated a microchannel that reduced the nanochannel length from mm-to  $\mu\text{m}$  range. This could be achieved by directly measuring the speed of the liquid front in the imaging area supported by computational evaluation of the liquid flow pattern.

### **7.1 The impact: general workflow for designing an LPEM experiment**

During this work, several aspects of LPEM were studied in order to gain insight into the structure and dynamics of colloidal assembly. However, the key impact of this work has been the efforts to systemically work through the many variables that affected the quality and reproducibility of results obtained with the LPEM. As has been demonstrated in this thesis, several unknowns need to be dealt with before LPEM can be used to probe into a given system. Variables include suitable imaging modality, acceptable electron dose, total dose history of the sample, required spatial and temporal resolution, electron beam damage, data-analysis, and consequences of confining a nano-object or a reaction into a femtoliter volume of the liquid cell. All of these factors may contribute to the obtained result, and thus obtaining a good reproducibility [24] for LPEM experiments is challenging. On the other hand, the cost of a single liquid cell experiment is typically a minimum of ~50 € [14], which is the approximate price for two commercial disposable chips that are used to assemble a liquid cell. Thus, during this work, we have strived to also understand how

the methodology of LPEM could be developed towards the direction where it could be applied to various soft matter systems.

It is likely not possible to come up with a single universal workflow for LPEM experiments because such a wide range of systems and system-specific questions can be studied. However, based on the literature and the experience gained during this work, a tentative, generally applicable workflow is provided to summarize those experimental steps that need to be taken in order to design a successful LPEM-experiment.

The feasibility of an LPEM experiment can be evaluated by first considering the required spatial resolution that is needed to solve the question at hand. As was shown in this work, *in silico* methods can be used as first-approximation tools to calculate the expected resolution and contrast for a given system.

Control experiments are needed to account for the effects of electron beam and confinement on the studied system. In addition, the computational results should be validated to verify that the obtained experimental contrast agrees to some extent with the *in silico* predictions. The hopes for attainable resolution might need to be adjusted in case the system is especially beam sensitive. In case the dynamics of a chemical or physical process are to be studied, it is important to find a controlled way to initiate and sustain the reaction in the confinement of the liquid cell. Data processing and analysis strategy should be considered early on as often the data from LPEM are affected by noise, and hence validation and quantification of observations can be challenging.

Ideally, the actual LPEM experiment is conducted with optimal imaging parameters in order to maximize the amount of information per used electron and to minimize the electron beam damage. To promote the reproducibility of an LPEM experiment, all details, including the time waiting between the steps of the sample preparation, should be reported. Furthermore, the total dose history of the sample is to be reported as radiolytic products can diffuse in the liquid environment. The *post mortem* analysis can be useful, especially when objects of interest have adhered to the window. This potentially allows to

study the structure with higher resolution and also to perform elemental analysis via EDX or EELS exclude unwanted artifacts.

Finally, the data obtained in LPEM is typically from a limited volume of the sample and also is affected by the confinement and the electron beam. It is thus beneficial to use complementary techniques such as dynamic light scattering (DLS), small-angle x-ray scattering (SAXS), optical nanoscopy, and molecular simulations to support the findings made with LPEM.

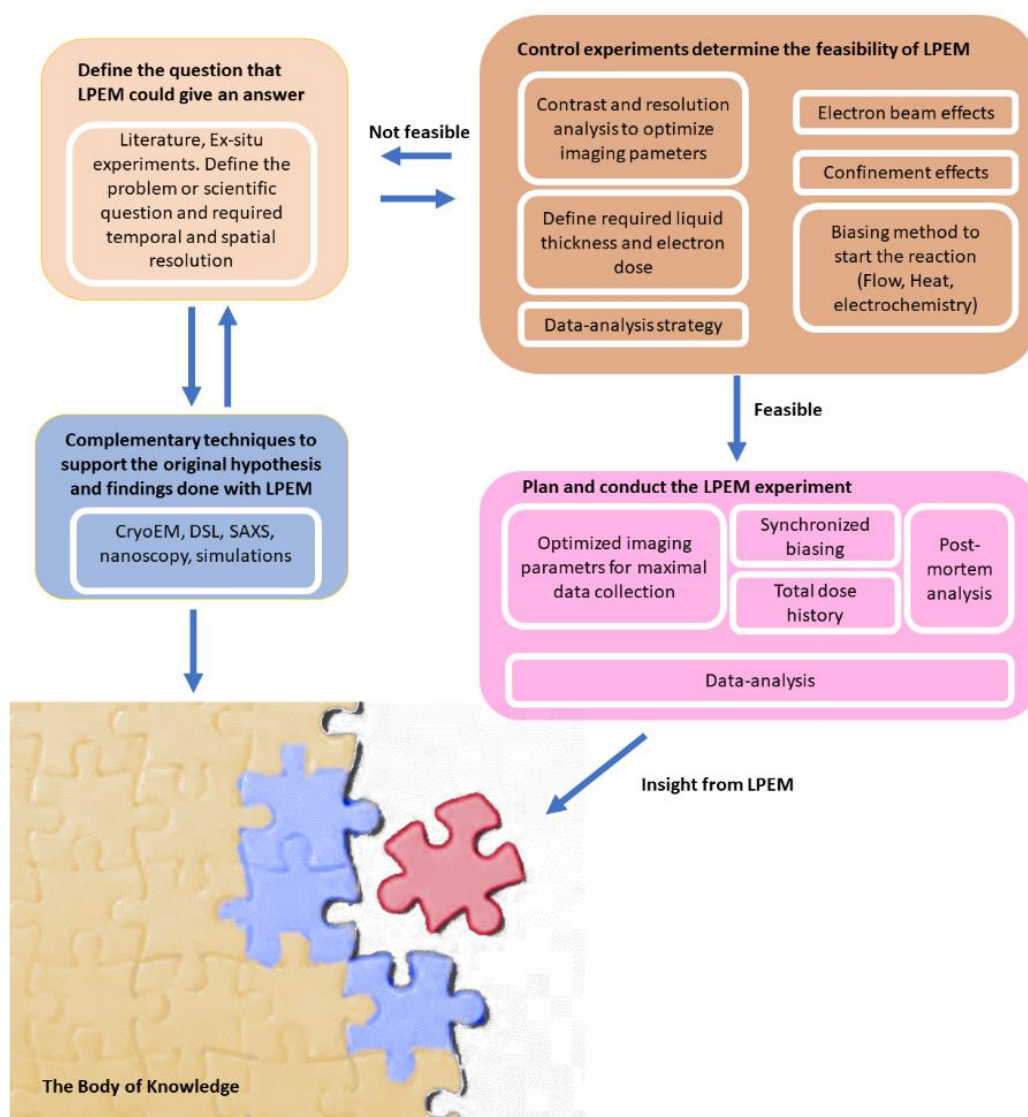


Figure 7.1 A general workflow proposed for planning and conducting an LPEM experiment.

## 7.2 Outlook

LPEM has been around since the early years of the electron microscopy, and recently it has received the interest of the wider scientific community. Although challenges are substantial, the attainable spatial resolution of LPEM is in the range that only some microscopic methods can probe directly. Commercial liquid cell holders and digital data acquisition are in the reach of almost any electron microscopy group, and this has given the technique a push forward in the past ten years. However, LPEM still not a technique that could be applied to any given system to probe its structure and dynamics as it happens in the bulk liquid. One reason for this is that every type of LPEM experiment typically requires a unique setup where the sample preparation, control experiments, imaging, and finally, data-analysis are tailored around a specific problem.

In terms of controlling the electron beam-induced effects, several technical solutions are expected to enable improved low-dose performance in LPEM. Such include aberration correction [103], and phase-plate technologies [66], which can be used to optimize the electron optical system for thick specimens and to enable medium and low magnification imaging with phase contrast, respectively. Adaptive sampling [159] techniques can be used to minimize the unnecessary irradiation on the sample. In STEM, this has already been realized using the combination of sparse scanning and in-painting techniques [160]. In TEM, a multi-pass instrument has been tested [161] where electron-optical mirrors are used to refocus already transmitted beam back on the sample multiple times, and finally, the electron beam is passed to the detector. This effectively results in spatially modulated sampling, where areas of high transmittance are sampled multiple times with higher beam intensity.

Secondly, the sample preparation is in a big role in LPEM, and some recent advances are expected to become more widely available in the near future. Replacing  $\text{SiN}_x$ -windows with, for example, graphene can enable high-resolution imaging due to the reduced sample thickness. The rational design of supported GLS's [162] could enable automatic sample preparation techniques similar to VitroBots used in cryo-EM. Automated sample preparation has already been introduced for the  $\text{SiN}_x$ -liquid cell platform [23], where a

robotic liquid dispenser was used to fill and assemble the liquid cell in an automated way. Finally, a microfluidic lab-on-a-chip platform has recently commercialized that enables direct flow capabilities and liquid heating on the same chip [27].

It is thus expected that in the near future, LPEM will be applied to several new systems, and this will hopefully help to further elucidate the fundamental challenges of LPEM, namely electron beam effects and confinement of the sample.

## Bibliography

- [1] M. A. Moradi *et al.*, "Formation of Hierarchical Hybrid Silica-Polymer Using Quantitative Cryo- Electron Tomography," *Microscopy and Microanalysis*, vol. 25, no. S1, pp. 59-60, 2019, doi: 10.1017/S1431927618016021.
- [2] H. Wu, H. Friedrich, J. P. Patterson, N. A. J. M. Sommerdijk, and N. de Jonge, "Liquid-Phase Electron Microscopy for Soft Matter Science and Biology," *Advanced Materials*, p. 2001582, 2020.
- [3] P. Hovington, D. Drouin, and R. Gauvin, "CASINO: A new Monte Carlo code in C language for electron beam interaction—Part I: Description of the program," *Scanning*, vol. 19, no. 1, pp. 1-14, 1997.
- [4] H. Demers, N. Poirier-Demers, D. Drouin, and N. de Jonge, "Simulating STEM imaging of nanoparticles in micrometers-thick substrates," *Microscopy and microanalysis : the official journal of Microscopy Society of America, Microbeam Analysis Society, Microscopical Society of Canada*, vol. 16, no. 6, pp. 795-804, 2010, doi: 10.1017/S1431927611005770.
- [5] S. Keskin, P. Kunnas, and N. de Jonge, "Liquid-Phase Electron Microscopy with Controllable Liquid Thickness," *Nano Letters*, vol. 19, no. 7, pp. 4608-4613, 2019/07/10 2019, doi: 10.1021/acs.nanolett.9b01576.
- [6] N. De Jonge, "Transmission electron microscopy for imaging live cells," *US patent 9.207,196 B2*, 2015.
- [7] I. W. Hamley, *Introduction to Soft Matter Synthetic and Biological Self-Assembling Materials, Revised Edition*. 2007.
- [8] D. B. Williams and C. B. Carter, *Transmission Electron Microscopy: A Textbook for Materials Science*. 2009, pp. 760-760.
- [9] S. S. W. Tai and X. M. Tang, "Manipulating biological samples for environmental scanning electron microscopy observation," *Scanning*, vol. 23, no. 4, pp. 267-272, 2001.
- [10] D. C. Pease, *Histological techniques for electron microscopy*. Academic Press, 1960.
- [11] L. E. Franken, E. J. Boekema, and M. C. A. Stuart, "Transmission electron microscopy as a tool for the characterization of soft materials: application and interpretation," *Advanced Science*, vol. 4, no. 5, p. 1600476, 2017.
- [12] K. Murata and M. Wolf, "Cryo-electron microscopy for structural analysis of dynamic biological macromolecules," *Biochimica et Biophysica Acta (BBA) - General Subjects*, vol. 1862, no. 2, pp. 324-334, 2018/02/01/ 2018, doi: <https://doi.org/10.1016/j.bbagen.2017.07.020>.
- [13] A. Dance, "Molecular motion on ice," *Nature methods*, pp. 1-5, 2020.

- [14] C. B. Carter and D. B. Williams, *Transmission electron microscopy: Diffraction, imaging, and spectrometry*. Springer, 2016.
- [15] J. Wu *et al.*, "In situ environmental TEM in imaging gas and liquid phase chemical reactions for materials research," *Advanced Materials*, vol. 28, no. 44, pp. 9686-9712, 2016.
- [16] v. E. Ruska, "Beitrag zur übermikroskopischen Abbildung bei höheren Drucken," *Kolloid-Zeitschrift*, vol. 100, no. 2, pp. 212-219, 1942.
- [17] C. Cassidy *et al.*, "Water without windows: Evaluating the performance of open cell transmission electron microscopy under saturated water vapor conditions, and assessing its potential for microscopy of hydrated biological specimens," *PLOS ONE*, vol. 12, no. 11, p. e0186899, 2017, doi: 10.1371/journal.pone.0186899.
- [18] I. M. Abrams and J. W. McBain, "A CLOSED CELL FOR ELECTRON MICROSCOPY," *Science*, vol. 100, no. 2595, p. 273, 1944, doi: 10.1126/science.100.2595.273.
- [19] M. J. Williamson, R. M. Tromp, P. M. Vereecken, R. Hull, and F. M. Ross, "Dynamic microscopy of nanoscale cluster growth at the solid-liquid interface," *Nat Mater*, vol. 2, no. 8, pp. 532-6, Aug 2003, doi: 10.1038/nmat944.
- [20] K.-L. Liu *et al.*, "Novel microchip for in situ TEM imaging of living organisms and bio-reactions in aqueous conditions," *Lab on a Chip*, vol. 8, no. 11, pp. 1915-1921, 2008.
- [21] N. de Jonge, D. B. Peckys, G. J. Kremers, and D. W. Piston, "Electron microscopy of whole cells in liquid with nanometer resolution," *Proceedings of the National Academy of Sciences of the United States of America*, vol. 106, no. 7, pp. 2159-2164, 2009, doi: 10.1073/pnas.0809567106.
- [22] E. Cepeda-Pérez and N. de Jonge, "Dynamics of gold nanoparticle clusters observed with liquid-phase electron microscopy," *Micron*, vol. 117, pp. 68-75, 2019.
- [23] J. P. Patterson *et al.*, "Picoliter Drop-On-Demand Dispensing for Multiplex Liquid Cell Transmission Electron Microscopy," *Microscopy and Microanalysis*, vol. 22, no. 03, pp. 507-514, 2016, doi: 10.1017/S1431927616000659.
- [24] A. Ianiro *et al.*, "Liquid-liquid phase separation during amphiphilic self-assembly," *Nature Chemistry*, vol. 11, no. 4, pp. 320-328, 2019/04/01 2019, doi: 10.1038/s41557-019-0210-4.
- [25] G. Marchello, C. De Pace, N. Wilkinson, L. Ruiz-Perez, and G. Battaglia, "4D liquid-phase electron microscopy of ferritin by Brownian single particle analysis," *arXiv preprint arXiv:1907.03348*, 2019.
- [26] E. A. Ring and N. de Jonge, "Microfluidic System for Transmission Electron Microscopy," *Microscopy and Microanalysis*, vol. 16, no. 5, pp. 622-629, 2010, doi: 10.1017/S1431927610093669.
- [27] J. T. van Omme *et al.*, "Liquid phase transmission electron microscopy with flow and temperature control," *Journal of Materials Chemistry C*, 10.1039/D0TC01103G 2020, doi: 10.1039/D0TC01103G.
- [28] C. Mueller, M. Harb, J. R. Dwyer, and R. J. D. Miller, "Nanofluidic Cells with Controlled Pathlength and Liquid Flow for Rapid, High-Resolution In Situ Imaging with Electrons," *The Journal of Physical Chemistry Letters*, vol. 4, no. 14, pp. 2339-2347, 2013, doi: 10.1021/jz401067k.
- [29] M. J. Dukes, J. Moering, and J. Damiano, "Optimization of Liquid Cell Transmission Electron Microscopy for Energy Dispersive X-Ray Spectroscopy," *Microscopy and Microanalysis*, vol. 24, no. S1, pp. 304-305, 2018.
- [30] K. W. Nichols, *Silicon Nitride Thin Films for Nanofluidic Device Fabrication*. 2017, pp. 190-236.
- [31] M. N. Yesibolati *et al.*, "Mean Inner Potential of Liquid Water," *Physical Review Letters*, vol. 124, no. 6, p. 065502, 02/13/ 2020, doi: 10.1103/PhysRevLett.124.065502.

- [32] D. F. Parsons, "Electron Microscopy and Diffraction of Wet Unstained and Unfixed Biological Objects," 1974.
- [33] S. E. Kirk, J. N. Skepper, and A. M. Donald, "Application of environmental scanning electron microscopy to determine biological surface structure," *Journal of Microscopy*, vol. 233, no. 2, pp. 205-224, 2009/02/01 2009, doi: 10.1111/j.1365-2818.2009.03111.x.
- [34] D. B. Peckys and N. De Jonge, "Gold nanoparticle uptake in whole cells in liquid examined by environmental scanning electron microscopy," *Microscopy and Microanalysis*, vol. 20, no. 1, pp. 189-197, 2014.
- [35] J. M. Yuk *et al.*, "High-Resolution EM of Colloidal Nanocrystal Growth Using Graphene Liquid Cells," *Science*, vol. 336, no. 6077, pp. 61-64, Apr 2012, doi: 10.1126/science.1217654.
- [36] A. Yulaev, A. Lipatov, A. X. Lu, A. Sinitskii, M. S. Leite, and A. Kolmakov, "Imaging and Analysis of Encapsulated Objects through Self-Assembled Electron and Optically Transparent Graphene Oxide Membranes," *Advanced Materials Interfaces*, vol. 4, no. 2, pp. 1-11, 2017, doi: 10.1002/admi.201600734.
- [37] J. Yang *et al.*, "MoS<sub>2</sub> liquid cell electron microscopy through clean and fast polymer-free MoS<sub>2</sub> transfer," *Nano letters*, vol. 19, no. 3, pp. 1788-1795, 2019.
- [38] M. Textor and N. de Jonge, "Strategies for preparing graphene liquid cells for transmission electron microscopy," *Nano letters*, vol. 18, no. 6, pp. 3313-3321, 2018.
- [39] S. Keskin and N. de Jonge, "Reduced Radiation Damage in Transmission Electron Microscopy of Proteins in Graphene Liquid Cells," *Nano Letters*, vol. 18, no. 12, pp. 7435-7440, 2018/12/12 2018, doi: 10.1021/acs.nanolett.8b02490.
- [40] H. Wang, B. Li, Y.-J. Kim, O.-H. Kwon, and S. Granick, "Intermediate states of molecular self-assembly from liquid-cell electron microscopy," *Proceedings of the National Academy of Sciences*, vol. 117, no. 3, pp. 1283-1292, 2020.
- [41] S. M. Ghodsi, S. Anand, R. Shahbazian-Yassar, T. Shokuhfar, and C. M. Megaridis, "In Situ Study of Molecular Structure of Water and Ice Entrapped in Graphene Nanovessels," *ACS Nano*, vol. 13, no. 4, pp. 4677-4685, 2019/04/23 2019, doi: 10.1021/acsnano.9b00914.
- [42] D. J. Kelly *et al.*, "Nanometer Resolution Elemental Mapping in Graphene-Based TEM Liquid Cells," *Nano Letters*, vol. 18, no. 2, pp. 1168-1174, 2018/02/14 2018, doi: 10.1021/acs.nanolett.7b04713.
- [43] G. Dunn *et al.*, "Graphene-Sealed Flow Cells for In Situ Transmission Electron Microscopy of Liquid Samples," *ACS Nano*, 2020.
- [44] N. Mohanty, M. Fahrenholtz, A. Nagaraja, D. Boyle, and V. Berry, "Impermeable graphenic encasement of bacteria," *Nano Letters*, vol. 11, no. 3, pp. 1270-1275, 2011, doi: 10.1021/nl104292k.
- [45] D. B. Peckys, U. Korf, and N. de Jonge, "Local variations of HER2 dimerization in breast cancer cells discovered by correlative fluorescence and liquid electron microscopy," *Science Advances*, vol. 1, no. 6, p. e1500165, 2015, doi: 10.1126/sciadv.1500165.
- [46] D. B. Peckys and N. de Jonge, "Visualizing Gold Nanoparticle Uptake in Live Cells with Liquid Scanning Transmission Electron Microscopy," *Nano Letters*, vol. 11, no. 4, pp. 1733-1738, Apr 2011, doi: 10.1021/nl200285r.
- [47] J. P. Patterson *et al.*, "Observing the Growth of Metal-Organic Frameworks by in Situ Liquid Cell Transmission Electron Microscopy," *Journal of the American Chemical Society*, vol. 137, no. 23, pp. 7322-7328, Jun 2015, doi: 10.1021/jacs.5b00817.
- [48] A. W. Robertson, G. Zhu, B. L. Mehdi, R. M. J. Jacobs, J. De Yoreo, and N. D. Browning, "Nanoparticle Immobilization for Controllable Experiments in Liquid-Cell Transmission

- Electron Microscopy," *ACS Applied Materials & Interfaces*, vol. 10, no. 26, pp. 22801-22808, 2018/07/05 2018, doi: 10.1021/acsami.8b03688.
- [49] D. B. Peckys, P. Mazur, K. L. Gould, and N. De Jonge, "Fully hydrated yeast cells imaged with electron microscopy," *Biophysical Journal*, vol. 100, no. 10, pp. 2522-2529, 2011, doi: 10.1016/j.bpj.2011.03.045.
- [50] B. L. Gilmore *et al.*, "Visualizing viral assemblies in a nanoscale biosphere," *Lab on a chip*, vol. 13, no. 2, pp. 216-9, 2013, doi: 10.1039/c2lc41008g.
- [51] J. M. Rodenburg and E. B. Macak, "Optimising the resolution of TEM/STEM with the electron ronchigram," *Microscopy*, 2013.
- [52] N. de Jonge and F. M. Ross, "Electron microscopy of specimens in liquid," *Nature Nanotechnology*, vol. 6, no. 11, pp. 695-704, Nov 2011, doi: 10.1038/nnano.2011.161.
- [53] P. Rez, "Comparison of phase contrast transmission electron microscopy with optimized scanning transmission annular dark field imaging for protein imaging," *Ultramicroscopy*, vol. 96, no. 1, pp. 117-124, 2003/07/01/ 2003, doi: [https://doi.org/10.1016/S0304-3991\(02\)00436-9](https://doi.org/10.1016/S0304-3991(02)00436-9).
- [54] B. Hafner, "Scanning electron microscopy primer," *Characterization Facility, University of Minnesota-Twin Cities*, pp. 1-29, 2007.
- [55] A. Bogner, G. Thollet, D. Basset, P. H. Jouneau, and C. Gauthier, "Wet STEM: A new development in environmental SEM for imaging nano-objects included in a liquid phase," *Ultramicroscopy*, vol. 104, no. 3, pp. 290-301, 2005/10/01/ 2005, doi: <https://doi.org/10.1016/j.ultramic.2005.05.005>.
- [56] R. Brydson and N. Hondow, "Electron energy loss spectrometry and energy dispersive X-ray analysis," *Aberration-Corrected Analytical Transmission Electron Microscopy*, pp. 163-210, 2011.
- [57] R. F. Egerton, *Physical principles of electron microscopy*. Springer, 2005.
- [58] H. Kohl and L. Reimer, *Transmission Electron Microscopy: Physics of Image Formation*, 5th ed. Springer, 2008, pp. 601-601.
- [59] N. de Jonge, "Theory of the spatial resolution of (scanning) transmission electron microscopy in liquid water or ice layers," *Ultramicroscopy*, vol. 187, pp. 113-125, 2018, doi: 10.1016/j.ultramic.2018.01.007.
- [60] H.-R. Zhang, R. F. Egerton, and M. Malac, "Local thickness measurement through scattering contrast and electron energy-loss spectroscopy," *Micron*, vol. 43, no. 1, pp. 8-15, 2012/01/01/ 2012, doi: <https://doi.org/10.1016/j.micron.2011.07.003>.
- [61] R. F. Egerton, "Radiation damage to organic and inorganic specimens in the TEM," *Micron*, vol. 119, pp. 72-87, 2019/04/01/ 2019, doi: <https://doi.org/10.1016/j.micron.2019.01.005>.
- [62] F. Salvat, A. Jablonski, and C. J. Powell, "ELSEPA—Dirac partial-wave calculation of elastic scattering of electrons and positrons by atoms, positive ions and molecules," *Computer physics communications*, vol. 165, no. 2, pp. 157-190, 2005.
- [63] A. Rose, "Comparative Noise Properties of Vision, Television, and Photographic Film," in *Vision: Human and Electronic*, A. Rose Ed. Boston, MA: Springer US, 1973, pp. 95-110.
- [64] J. Beutel, H. L. Kundel, and R. L. Van Metter, *Handbook of medical imaging*. Spie Press, 2000.
- [65] N. de Jonge, A. Verch, and H. Demers, "The influence of beam broadening on the spatial resolution of annular dark field scanning transmission electron microscopy," *Microscopy and Microanalysis*, vol. 24, no. 1, p. 8, 2018.
- [66] K. Nagayama, "Development of phase plates for electron microscopes and their biological application," *European Biophysics Journal*, vol. 37, no. 4, pp. 345-358, 2008.

- [67] Y. C. Wang, T. M. Chou, M. Libera, E. Voelkl, and B. G. Frost, "Measurement of Polystyrene Mean Inner Potential by Transmission Electron Holography of Latex Spheres," *Microscopy and Microanalysis*, vol. 4, no. 2, pp. 146-157, 1998, doi: 10.1017/S143192769898014X.
- [68] L. Reimer and B. Lödding, "Calculation and tabulation of Mott cross-sections for large-angle electron scattering," *Scanning*, vol. 6, no. 3, pp. 128-151, 1984.
- [69] D. Rez, P. Rez, and I. Grant, "Dirac–Fock calculations of X-ray scattering factors and contributions to the mean inner potential for electron scattering," *Acta Crystallographica Section A: Foundations of Crystallography*, vol. 50, no. 4, pp. 481-497, 1994.
- [70] R. R. Meyer and A. I. Kirkland, "Characterisation of the signal and noise transfer of CCD cameras for electron detection," *Microscopy Research and Technique*, vol. 49, no. 3, pp. 269-280, 2000.
- [71] U. M. Mirsaidov, H. Zheng, Y. Casana, and P. Matsudaira, "Imaging protein structure in water at 2.7 nm resolution by transmission electron microscopy," *Biophysical journal*, vol. 102, no. 4, pp. L15-L17, 2012.
- [72] E. J. Kirkland, "Plotting Transfer Functions," in *Advanced Computing in Electron Microscopy*, E. J. Kirkland Ed. Boston, MA: Springer US, 2010, pp. 233-240.
- [73] J. A. Mindell and N. Grigorieff, "Accurate determination of local defocus and specimen tilt in electron microscopy," (in eng), *J Struct Biol*, vol. 142, no. 3, pp. 334-47, Jun 2003, doi: 10.1016/s1047-8477(03)00069-8.
- [74] R. H. Wade, "Electron microscope transfer functions for partially coherent axial illumination and chromatic defocus spread," 1977.
- [75] K. F. Han, J. W. Sedat, and D. A. Agard, "Mechanism of image formation for thick biological specimens: exit wavefront reconstruction and electron energy-loss spectroscopic imaging," *Journal of Microscopy*, vol. 178, no. 2, pp. 107-119, 1995, doi: 10.1111/j.1365-2818.1995.tb03586.x.
- [76] K. F. Han, J. W. Sedat, and D. A. Agard, "Practical image restoration of thick biological specimens using multiple: Focus levels in transmission electron microscopy," *Journal of Structural Biology*, vol. 120, no. 3, pp. 237-244, 1997, doi: 10.1006/jsbi.1997.3914.
- [77] E. J. Kirkland, "Theory of Calculation of Images of Thick Specimens," in *Advanced Computing in Electron Microscopy*, E. J. Kirkland Ed. Boston, MA: Springer US, 2010, pp. 115-161.
- [78] F. M. Ross and W. M. Stobbs, "Computer modelling for Fresnel contrast analysis," *Philosophical Magazine A: Physics of Condensed Matter, Structure, Defects and Mechanical Properties*, vol. 63, no. 1, pp. 37-70, 1991, doi: 10.1080/01418619108204592.
- [79] Y. Tomo, K. Takahashi, T. Nishiyama, T. Ikuta, and Y. Takata, "Nanobubble nucleation studied using Fresnel fringes in liquid cell electron microscopy," *International Journal of Heat and Mass Transfer*, vol. 108, pp. 1460-1465, 2017/05/01/ 2017, doi: <https://doi.org/10.1016/j.ijheatmasstransfer.2017.01.013>.
- [80] M. Wang, C. Park, and T. Woehl, "Toward Quantitative Liquid Cell Electron Microscopy through Kinetic Control of Solution Chemistry," *Microscopy and Microanalysis*, vol. 25, no. S1, pp. 23-24, 2019, doi: 10.1017/S1431927618015854.
- [81] T. Yamazaki *et al.*, "Two types of amorphous protein particles facilitate crystal nucleation," *Proceedings of the National Academy of Sciences of the United States of America*, vol. 114, no. 9, pp. 2154-2159, Feb 2017, doi: 10.1073/pnas.1606948114.
- [82] A. S. Powers, H.-G. Liao, S. N. Raja, N. D. Bronstein, A. P. Alivisatos, and H. Zheng, "Tracking Nanoparticle Diffusion and Interaction during Self-Assembly in a Liquid Cell," *Nano Letters*, vol. 17, no. 1, pp. 15-20, 2017/01/11 2017, doi: 10.1021/acs.nanolett.6b02972.

- [83] D. B. Peckys and N. de Jonge, "Liquid scanning transmission electron microscopy: imaging protein complexes in their native environment in whole eukaryotic cells," *Microsc Microanal*, vol. 20, no. 2, pp. 346-65, Apr 2014, doi: 10.1017/S1431927614000099.
- [84] B. L. Mehdi *et al.*, "Observation and quantification of nanoscale processes in lithium batteries by operando electrochemical (S) TEM," *Nano letters*, vol. 15, no. 3, pp. 2168-2173, 2015.
- [85] P. Abellan, T. J. Woehl, L. R. Parent, N. D. Browning, J. E. Evans, and I. Arslan, "Factors influencing quantitative liquid (scanning) transmission electron microscopy," *Chemical Communications*, 10.1039/C3CC48479C vol. 50, no. 38, pp. 4873-4880, 2014, doi: 10.1039/C3CC48479C.
- [86] N. M. Schneider, M. M. Norton, B. J. Mendel, J. M. Grogan, F. M. Ross, and H. H. Bau, "Electron-Water interactions and implications for liquid cell electron microscopy," *Journal of Physical Chemistry C*, vol. 118, no. 38, pp. 22373-22382, 2014, doi: 10.1021/jp507400n.
- [87] L. R. Parent *et al.*, "Tackling the Challenges of Dynamic Experiments Using Liquid-Cell Transmission Electron Microscopy," (in English), *Accounts of Chemical Research*, Review vol. 51, no. 1, pp. 3-11, Jan 2018, doi: 10.1021/acs.accounts.7b00331.
- [88] R. Kröger and A. Verch, "Liquid Cell Transmission Electron Microscopy and the Impact of Confinement on the Precipitation from Supersaturated Solutions," *Minerals*, vol. 8, no. 1, 2018, doi: 10.3390/min8010021.
- [89] P. J. M. Smeets, K. R. Cho, R. G. E. Kempen, N. A. J. M. Sommerdijk, and J. J. De Yoreo, "Calcium carbonate nucleation driven by ion binding in a biomimetic matrix revealed by in situ electron microscopy," *Nature materials*, vol. 14, no. 4, pp. 394-399, 2015.
- [90] Y. Mei, Y. Lu, F. Polzer, M. Ballauff, and M. Drechsler, "Catalytic Activity of Palladium Nanoparticles Encapsulated in Spherical Polyelectrolyte Brushes and Core-Shell Microgels," *Chemistry of Materials*, vol. 19, no. 5, pp. 1062-1069, 2007/03/01 2007, doi: 10.1021/cm062554s.
- [91] S. M. Rehn and M. R. Jones, "New Strategies for Probing Energy Systems with In Situ Liquid-Phase Transmission Electron Microscopy," *ACS Energy Letters*, vol. 3, no. 6, pp. 1269-1278, 2018/06/08 2018, doi: 10.1021/acsenerylett.8b00527.
- [92] T. J. Woehl and P. Abellan, "Defining the radiation chemistry during liquid cell electron microscopy to enable visualization of nanomaterial growth and degradation dynamics," *Journal of Microscopy*, vol. 265, no. 2, pp. 135-147, 2017/02/01 2017, doi: 10.1111/jmi.12508.
- [93] M. Wang, C. Park, and T. J. Woehl, "Quantifying the Nucleation and Growth Kinetics of Electron Beam Nanochemistry with Liquid Cell Scanning Transmission Electron Microscopy," *Chemistry of Materials*, vol. 30, no. 21, pp. 7727-7736, 2018/11/13 2018, doi: 10.1021/acs.chemmater.8b03050.
- [94] Kitching and Donald, "Beam damage of polypropylene in the environmental scanning electron microscope: an FTIR study," *Journal of Microscopy*, vol. 190, no. 3, pp. 357-365, 1998/06/01 1998, doi: 10.1046/j.1365-2818.1998.00346.x.
- [95] P. Abellan, T. H. Moser, I. T. Lucas, J. W. Grate, J. E. Evans, and N. D. Browning, "The formation of cerium(iii) hydroxide nanoparticles by a radiation mediated increase in local pH," *RSC Advances*, 10.1039/C6RA27066B vol. 7, no. 7, pp. 3831-3837, 2017, doi: 10.1039/C6RA27066B.
- [96] M. A. Touve *et al.*, "Polymerization-Induced Self-Assembly of Micelles Observed by Liquid Cell Transmission Electron Microscopy," *ACS Central Science*, 2018.
- [97] L. R. Parent *et al.*, "Directly Observing Micelle Fusion and Growth in Solution by Liquid-Cell Transmission Electron Microscopy," 2017.

- [98] Z. Ou, Z. Wang, B. Luo, E. Luijten, and Q. Chen, "Kinetic pathways of crystallization at the nanoscale," *Nature Materials*, 2019/10/28 2019, doi: 10.1038/s41563-019-0514-1.
- [99] M. A. Touve, A. S. Carlini, and N. C. Gianneschi, "Self-assembling peptides imaged by correlated liquid cell transmission electron microscopy and MALDI-imaging mass spectrometry," *Nature Communications*, vol. 10, no. 1, p. 4837, 2019/10/23 2019, doi: 10.1038/s41467-019-12660-1.
- [100] J. J. De Yoreo and S. N. A. J. M., "Investigating materials formation with liquid-phase and cryogenic TEM," *Nature Reviews Materials*, vol. 12, pp. 16035-16035, 2016, doi: 10.1038/natrevmats.2016.35.
- [101] C. A. Silvera Batista, R. G. Larson, and N. A. Kotov, "Nonadditivity of nanoparticle interactions," *Science*, 2015, doi: 10.1126/science.1242477.
- [102] K. Gnanasekaran, H. Chang, P. J. M. Smeets, J. Korpany, F. M. Geiger, and N. C. Gianneschi, "In Situ Ni<sup>2+</sup> Stain for Liposome Imaging by Liquid-Cell Transmission Electron Microscopy," *Nano Letters*, vol. 20, no. 6, pp. 4292-4297, 2020/06/10 2020, doi: 10.1021/acs.nanolett.0c00898.
- [103] N. de Jonge, L. Houben, R. E. Dunin-Borkowski, and F. M. Ross, "Resolution and aberration correction in liquid cell transmission electron microscopy," *Nature Reviews Materials*, vol. 4, no. 1, pp. 61-78, 2019/01/01 2019, doi: 10.1038/s41578-018-0071-2.
- [104] H. Cho, M. R. Jones, S. C. Nguyen, M. R. Hauwiller, A. Zettl, and A. P. Alivisatos, "The use of graphene and its derivatives for liquid-phase transmission electron microscopy of radiation-sensitive specimens," *Nano Letters*, vol. 17, no. 1, pp. 414-420, 2017, doi: 10.1021/acs.nanolett.6b04383.
- [105] S. Keskin *et al.*, "Visualization of Multimerization and Self-Assembly of DNA-Functionalized Gold Nanoparticles Using In-Liquid Transmission Electron Microscopy," *Journal of Physical Chemistry Letters*, vol. 6, no. 22, pp. 4487-4492, 2015, doi: 10.1021/acs.jpcclett.5b02075.
- [106] A. Verch, M. Pfaff, and N. De Jonge, "Exceptionally Slow Movement of Gold Nanoparticles at a Solid/Liquid Interface Investigated by Scanning Transmission Electron Microscopy," *Langmuir*, vol. 31, no. 25, pp. 6956-6964, 2015, doi: 10.1021/acs.langmuir.5b00150.
- [107] B. a. Grzybowski, C. E. Wilmer, J. Kim, K. P. Browne, and K. J. M. Bishop, "Self-assembly: from crystals to cells," *Soft Matter*, vol. 5, no. 6, pp. 1110-1110, 2009, doi: 10.1039/b819321p.
- [108] J. N. Israelachvili, *Intermolecular and surface forces*. Academic press, 2011.
- [109] T. J. Woehl and T. Prozorov, "The Mechanisms for Nanoparticle Surface Diffusion and Chain Self-Assembly Determined from Real-Time Nanoscale Kinetics in Liquid," *The Journal of Physical Chemistry C*, vol. 119, no. 36, pp. 21261-21269, 2015/09/10 2015, doi: 10.1021/acs.jpcc.5b07164.
- [110] M. N. Yesibolati, K. I. Mortensen, H. Sun, A. Brostrøm, S. Tidemand-Lichtenberg, and K. Møhlhave, "Unhindered Brownian Motion of Individual Nanoparticles in Liquid Phase Scanning Transmission Electron Microscopy," *Nano Letters*, 2020.
- [111] Y. Liu, X.-M. Lin, Y. Sun, and T. Rajh, "In Situ Visualization of Self-Assembly of Charged Gold Nanoparticles," *Journal of the American Chemical Society*, vol. 135, no. 10, pp. 3764-3767, 2013/03/13 2013, doi: 10.1021/ja312620e.
- [112] T. A. J. Welling *et al.*, "Observation of Undamped 3D Brownian Motion of Nanoparticles Using Liquid-Cell Scanning Transmission Electron Microscopy," *Particle & Particle Systems Characterization*, p. 2000003, 2020.
- [113] J. Kim, M. R. Jones, Z. Ou, and Q. Chen, "In Situ Electron Microscopy Imaging and Quantitative Structural Modulation of Nanoparticle Superlattices," *ACS Nano*, vol. 10, no. 11, pp. 9801-9808, 2016/11/22 2016, doi: 10.1021/acsnano.6b05270.

- [114] R. F. Egerton, "Control of radiation damage in the TEM," *Ultramicroscopy*, vol. 127, pp. 100-108, 2013/04/01/ 2013, doi: <https://doi.org/10.1016/j.ultramic.2012.07.006>.
- [115] M. Wang, T. U. Dissanayake, C. Park, K. Gaskell, and T. J. Woehl, "Nanoscale Mapping of Nonuniform Heterogeneous Nucleation Kinetics Mediated by Surface Chemistry," *Journal of the American Chemical Society*, vol. 141, no. 34, pp. 13516-13524, 2019/08/28 2019, doi: 10.1021/jacs.9b05225.
- [116] S. W. Chee, Z. Baraissov, N. D. Loh, P. T. Matsudaira, and U. Mirsaidov, "Desorption-Mediated Motion of Nanoparticles at the Liquid–Solid Interface," *The Journal of Physical Chemistry C*, pp. acs.jpcc.6b07983-acs.jpcc.6b07983, 2016, doi: 10.1021/acs.jpcc.6b07983.
- [117] X. Fu, B. Chen, J. Tang, M. T. Hassan, and A. H. Zewail, "Imaging rotational dynamics of nanoparticles in liquid by 4D electron microscopy," *Science*, 10.1126/science.aah3582 vol. 355, no. 6324, p. 494, 2017.
- [118] G. Lin *et al.*, "Nanodroplet-Mediated Assembly of Platinum Nanoparticle Rings in Solution," *Nano Letters*, vol. 16, no. 2, pp. 1092-1096, 2016/02/10 2016, doi: 10.1021/acs.nanolett.5b04323.
- [119] Y. Zhou *et al.*, "Growth and assembly of cobalt oxide nanoparticle rings at liquid nanodroplets with solid junction," *Nanoscale*, vol. 9, no. 37, pp. 13915-13921, 2017.
- [120] K. Gnanasekaran, G. de With, and H. Friedrich, "Quantification and optimization of ADF-STEM image contrast for beam-sensitive materials," *Royal Society Open Science*, vol. 5, no. 5, p. 171838, 2018, doi: 10.1098/rsos.171838.
- [121] T. Yokoi, Y. Sakamoto, O. Terasaki, Y. Kubota, T. Okubo, and T. Tatsumi, "Periodic Arrangement of Silica Nanospheres Assisted by Amino Acids," *Journal of the American Chemical Society*, vol. 128, no. 42, pp. 13664-13665, 2006/10/01 2006, doi: 10.1021/ja065071y.
- [122] G. T. Hermanson, *Bioconjugate Techniques*, 2nd ed. Amsterdam: Elsevier, 2013.
- [123] T. Malis, S. C. Cheng, and R. F. Egerton, "EELS log-ratio technique for specimen-thickness measurement in the TEM," *Journal of Electron Microscopy Technique*, vol. 8, no. 2, pp. 193-200, 1988/02/01 1988, doi: 10.1002/jemt.1060080206.
- [124] K. L. Jungjohann, J. E. Evans, J. A. Aguiar, I. Arslan, and N. D. Browning, "Atomic-scale imaging and spectroscopy for in situ liquid scanning transmission electron microscopy," *Microscopy and microanalysis : the official journal of Microscopy Society of America, Microbeam Analysis Society, Microscopical Society of Canada*, vol. 18, no. 3, pp. 621-7, 2012, doi: 10.1017/S1431927612000104.
- [125] M. N. Yesibolati *et al.*, "Electron inelastic mean free path in water," *Nanoscale*, 2020.
- [126] X. Xu, T. Franke, K. Schilling, N. A. J. M. Sommerdijk, and H. Cölfen, "Binary Colloidal Nanoparticle Concentration Gradients in a Centrifugal Field at High Concentration," *Nano Letters*, vol. 19, no. 2, pp. 1136-1142, 2019/02/13 2019, doi: 10.1021/acs.nanolett.8b04496.
- [127] A. Jablonski, F. Salvat, C. J. Powel, and A. Y. Lee, "NIST Electron Elastic-Scattering Cross-Section Database Version 4.0, NIST Standard Reference Database Number 64," 2016.
- [128] T. H. Moser, T. Shokuhfar, and J. E. Evans, "Considerations for imaging thick, low contrast, and beam sensitive samples with liquid cell transmission electron microscopy," *Micron*, vol. 117, pp. 8-15, 2019/02/01/ 2019, doi: <https://doi.org/10.1016/j.micron.2018.10.007>.
- [129] Varlot, Martin, and Quet, "Physical and chemical changes in polystyrene during electron irradiation using EELS in the TEM: contribution of the dielectric function," *Journal of Microscopy*, vol. 191, no. 2, pp. 187-194, 1998/08/01 1998, doi: 10.1046/j.1365-2818.1998.00376.x.

- [130] J. Zečević, J. Hermannsdörfer, T. Schuh, K. P. de Jong, and N. de Jonge, "Anisotropic shape changes of silica nanoparticles induced in liquid with scanning transmission electron microscopy," *small*, vol. 13, no. 1, p. 1602466, 2017.
- [131] M. W. P. van de Put, C. C. M. C. Carcouët, P. H. H. Bomans, H. Friedrich, N. de Jonge, and N. A. J. M. Sommerdijk, "Writing silica structures in liquid with scanning transmission electron microscopy," *Small*, vol. 11, no. 5, pp. 585-590, 2015.
- [132] D. F. Kyser, "Monte Carlo Simulation in Analytical Electron Microscopy," in *Introduction to Analytical Electron Microscopy*, J. J. Hren, J. I. Goldstein, and D. C. Joy Eds. Boston, MA: Springer US, 1979, pp. 199-221.
- [133] R. Eckhardt, S. Ulam, and J. Von Neumann, "the Monte Carlo method," *Los Alamos Science*, no. 15, p. 131, 1987.
- [134] A. A. Sousa, M. F. Hohmann-Marriott, G. Zhang, and R. D. Leapman, "Monte Carlo electron-trajectory simulations in bright-field and dark-field STEM: Implications for tomography of thick biological sections," *Ultramicroscopy*, vol. 109, no. 3, pp. 213-221, 2009.
- [135] D. C. Joy and S. Luo, "An empirical stopping power relationship for low-energy electrons," *Scanning*, vol. 11, no. 4, pp. 176-180, 1989.
- [136] N. de Jonge, N. Poirier-Demers, H. Demers, D. B. Peckys, and D. Drouin, "Nanometer-resolution electron microscopy through micrometers-thick water layers," *Ultramicroscopy*, vol. 110, no. 9, pp. 1114-1119, 2010, doi: 10.1016/j.ultramic.2010.04.001.
- [137] Q. Bao and A. F. Chatziioannou, "Estimation of the minimum detectable activity of preclinical PET imaging systems with an analytical method," *Medical Physics*, vol. 37, no. 11, pp. 6070-6083, 2010/11/01 2010, doi: 10.1118/1.3495817.
- [138] K. Eldevik, W. Nordhøy, and A. Skretting, "Relationship between sharpness and noise in CT images reconstructed with different kernels," *Radiation protection dosimetry*, vol. 139, no. 1-3, pp. 430-433, 2010.
- [139] H. Demers *et al.*, "Three-dimensional electron microscopy simulation with the CASINO Monte Carlo software," *Scanning*, vol. 33, no. 3, pp. 135-146, 2011, doi: 10.1002/sca.20262.
- [140] S. R. Cherry, J. A. Sorenson, and M. E. Phelps, *Physics in nuclear medicine e-Book*. Elsevier Health Sciences, 2012.
- [141] K. Aoyama, K. Nagano, and K. Mitsuoka, "Optimization of STEM imaging conditions for cryo-tomography," *Microscopy*, vol. 66, no. 3, pp. 212-216, 2017.
- [142] D. Alansary, D. B. Peckys, B. A. Niemeyer, and N. de Jonge, "Detecting single ORAI1 proteins within the plasma membrane reveals higher-order channel complexes," *Journal of Cell Science*, vol. 133, no. 1, 2020.
- [143] A. Cameron Varano, A. Rahimi, M. J. Dukes, S. Poelzing, S. M. McDonald, and D. F. Kelly, "Visualizing virus particle mobility in liquid at the nanoscale," *Chem. Commun.*, vol. 51, no. 90, pp. 16176-16179, 2015, doi: 10.1039/C5CC05744B.
- [144] H. Wang, K. H. Nagamanasa, Y.-J. Kim, O.-H. Kwon, and S. Granick, "Longer-Lasting Electron-Based Microscopy of Single Molecules in Aqueous Medium," *ACS Nano*, 2018/07/18 2018, doi: 10.1021/acsnano.8b04190.
- [145] M. A. Winnik, C. L. Zhao, O. Shaffer, and R. R. Shivers, "Electron microscopy studies of polystyrene-poly(methyl methacrylate) core-shell latex particles," *Langmuir*, vol. 9, no. 8, pp. 2053-2065, 1993/08/01 1993, doi: 10.1021/la00032a025.
- [146] N. Jiang, "Electron beam damage in oxides: a review," *Reports on Progress in Physics*, vol. 79, no. 1, p. 016501, 2015/12/18 2015, doi: 10.1088/0034-4885/79/1/016501.
- [147] M. J. Meijerink, C. Spiga, T. W. Hansen, C. D. Damsgaard, K. P. de Jong, and J. Zečević, "Nanoscale Imaging and Stabilization of Silica Nanospheres in Liquid Phase Transmission

- Electron Microscopy," *Particle & Particle Systems Characterization*, vol. 36, no. 1, p. 1800374, 2019/01/01 2019, doi: 10.1002/ppsc.201800374.
- [148] M. Piffoux *et al.*, "Monitoring the dynamics of cell-derived extracellular vesicles at the nanoscale by liquid-cell transmission electron microscopy," *Nanoscale*, 10.1039/C7NR07576F vol. 10, no. 3, pp. 1234-1244, 2018, doi: 10.1039/C7NR07576F.
- [149] F. M. Ross and W. M. Stobbs, "A study of the initial stages of the oxidation of silicon using the Fresnel method," *Philosophical Magazine A: Physics of Condensed Matter, Structure, Defects and Mechanical Properties*, vol. 63, no. 1, pp. 1-36, 1991, doi: 10.1080/01418619108204591.
- [150] W. M. Stobbs, "Electron Microscopical Techniques For The Observation Of Cavities," *Journal of Microscopy*, vol. 116, no. 1, pp. 3-13, 1979, doi: 10.1111/j.1365-2818.1979.tb00184.x.
- [151] R. E. Dunin-Borkowski, "The development of Fresnel contrast analysis, and the interpretation of mean inner potential profiles at interfaces," (in eng), *Ultramicroscopy*, vol. 83, no. 3-4, pp. 193-216, 2000/06// 2000, doi: 10.1016/s0304-3991(00)00015-2.
- [152] D. J. Johnson and D. Crawford, "Defocusing phase contrast effects in electron microscopy," *Journal of Microscopy*, vol. 98, no. 3, pp. 313-324, 1973, doi: 10.1111/j.1365-2818.1973.tb03835.x.
- [153] C. Wadell, S. Inagaki, T. Nakamura, J. Shi, Y. Nakamura, and T. Sannomiya, "Nanocuvette: A Functional Ultrathin Liquid Container for Transmission Electron Microscopy," *ACS Nano*, vol. 11, no. 2, pp. 1264-1272, Feb 28 2017, doi: 10.1021/acsnano.6b05007.
- [154] C. Kleinstreuer, *Microfluidics and nanofluidics: theory and selected applications*. John Wiley & Sons, 2013.
- [155] P. Kunnas, S. Rzadkiewicz, M.-A. Moradi, J. Patterson, N. Sommerdijk, and N. de Jonge, "Challenges in Observing the Formation of Colloidal, Self-Assembled Monolayers with In Situ Electron Microscopy in Liquid," *Microscopy and Microanalysis*, vol. 25, no. S1, pp. 55-56, 2019, doi: 10.1017/S1431927618016008.
- [156] A. Einstein, "Über die von der molekularkinetischen Theorie der Wärme geforderte Bewegung von in ruhenden Flüssigkeiten suspendierten Teilchen," *Annalen der physik*, vol. 4, 1905.
- [157] M. Sadowska, Z. Adamczyk, and M. Nattich-Rak, "Mechanism of nanoparticle deposition on polystyrene latex particles," *Langmuir*, vol. 30, no. 3, pp. 692-699, 2014, doi: 10.1021/la404046c.
- [158] C. A. Johnson and A. M. Lenhoff, "Adsorption of charged latex particles on mica studied by atomic force microscopy," *Journal of colloid and interface science*, vol. 179, no. 2, pp. 587-599, 1996.
- [159] T. Dahmen *et al.*, "Feature Adaptive Sampling for Scanning Electron Microscopy," *Scientific Reports*, Article vol. 6, p. 25350, 05/06/online 2016, doi: 10.1038/srep25350.
- [160] N. D. Browning *et al.*, "Using Sub-Sampling/Inpainting to Control the Kinetics and Observation Efficiency of Dynamic Processes in Liquids," *Microscopy and Microanalysis*, vol. 24, no. S1, pp. 242-243, 2018, doi: 10.1017/S1431927618001708.
- [161] C. Ophus, T. Juffmann, S. A. Koppell, B. B. Klopfer, R. Glaeser, and M. A. Kasevich, "Reducing Electron Beam Damage with Multipass Transmission Electron Microscopy," *Microscopy and Microanalysis*, vol. 23, no. S1, pp. 1794-1795, 2017.
- [162] N. Noh, J. Park, J. S. Park, K. Koo, J. Y. Park, and J. M. Yuk, "Lithographically patterned well-type graphene liquid cells with rational designs," *Lab on a Chip*, vol. 20, no. 15, pp. 2796-2803, 2020.

- [163] D. R. G. Mitchell and M. J. B. Nancarrow, "Probe current determination in analytical TEM/STEM and its application to the characterization of large area EDS detectors," *Microscopy Research and Technique*, vol. 78, no. 10, pp. 886-893, 2015/10/01 2015, doi: 10.1002/jemt.22551.
- [164] C. Trevor, "Using Bernd's easy current measuring control for the 2keV Drift Tube rev. 2," in "Technical document," 2013.
- [165] T. H. Moser, H. Mehta, C. Park, R. T. Kelly, T. Shokuhfar, and J. E. Evans, "The role of electron irradiation history in liquid cell transmission electron microscopy," *Science Advances*, vol. 4, no. 4, p. eaaq1202, 2018, doi: 10.1126/sciadv.aaq1202.
- [166] N. Ahmad, Y. Le Bouar, C. Ricolleau, and D. Alloyeau, "Growth of dendritic nanostructures by liquid-cell transmission electron microscopy: a reflection of the electron-irradiation history," *Advanced Structural and Chemical Imaging*, vol. 2, no. 1, p. 9, 2016/06/30 2016, doi: 10.1186/s40679-016-0023-0.
- [167] M. E. Holtz, Y. Yu, J. Gao, H. D. Abruña, and D. A. Muller, "In Situ Electron Energy-Loss Spectroscopy in Liquids," *Microsc.Microanal.*, vol. 19, pp. 1027-1035, 2013.
- [168] T. Ferreira. "ImageJ User Guide - IJ 1.46r | Analyze Menu." <https://www.ncbi.nlm.nih.gov/pubmed/> (accessed 15.08.2019).
- [169] C. H. Li and P. K. S. Tam, "An iterative algorithm for minimum cross entropy thresholding," *Pattern Recognition Letters*, vol. 19, no. 8, pp. 771-776, 1998/06/01/ 1998, doi: [https://doi.org/10.1016/S0167-8655\(98\)00057-9](https://doi.org/10.1016/S0167-8655(98)00057-9).

## Publications

1. P. Kunnas, S. Rzedkiewicz, M.-A. Moradi, J. Patterson, N. Sommerdijk, and N. de Jonge, "Challenges in Observing the Formation of Colloidal, Self-Assembled Monolayers with In Situ Electron Microscopy in Liquid," *Microscopy and Microanalysis*, vol. 25, no. S1, pp. 55-56, 2019
2. S. Keskin, P. Kunnas, and N. de Jonge, "Liquid-Phase Electron Microscopy with Controllable Liquid Thickness," *Nano Letters*, vol. 19, no. 7, pp. 4608-4613, 2019/07/10 2019
3. B. Uder, H. Gao, P. Kunnas, N. de Jonge, and U. Hartmann, "Low-force spectroscopy on graphene membranes by scanning tunneling microscopy," *Nanoscale*, vol. 10, no. 4, pp. 2148-2153, 2018
4. G. Hahn, P. Kunnas, N. de Jonge, and R. Kempe, "General synthesis of primary amines via reductive amination employing a reusable nickel catalyst," *Nature Catalysis*, vol. 2, no. 1, pp. 71-77, 2019
5. T. Schwob, P. Kunnas, N. de Jonge, C. Papp, H. P. Steinrück, and R. Kempe, "General and selective deoxygenation by hydrogen using a reusable earth-abundant metal catalyst," *Science Advances*, vol. 5, no. 11, 2019

## Oral communications and conferences

Kunnas, P., Dahmke, I., de Jonge, N., *Liquid-phase electron microscopy: from colloidal dynamics to transmembrane proteins in whole SKBR3 cell*. Invited lecture, Turku Biolmaging, 2018

## Invited lectures in conferences

P. Kunnas, I.N. Dahmke, N. de Jonge, N. *Studying soft systems with electron microscopy in liquid*. "Celebration of the Electron-symposium", Invited lecture, DESY, CFEL Hamburg, 2017

### **Poster communications in conferences**

P. Kunnas, M.A. Moradi, J. Patterson, N. Sommerdijk, N. de Jonge, *Liquid-phase Electron Microscopy of Colloidal Self-assembled monolayers*, Self-assembly of colloidal systems 2018

P. Kunnas, M.A. Moradi, J. Patterson, N. Sommerdijk, N. de Jonge, *Challenges in liquid-phase Electron Microscopy of Colloidal Self-assembled monolayers*, International Conference on In Situ and Correlative Electron Microscopy 2018

P. Kunnas, M.A. Moradi, J. Patterson, N. Sommerdijk, N. de Jonge, *Liquid-phase Electron Microscopy for observing colloidal self-assembly of low-Z material* Microscopy of Organic-Inorganic Interfaces-2019 meeting

### **Supplementary Information**

The following supplementary files are available on request:

1. MATLAB script for calculating the attainable resolution in STEM and TEM. Used for Figures 1.1-1.4 and Figure 1.6.
2. Casino file used for simulating the data shown in Figures 3.2-3.4
3. Casino file used for simulating the data shown in Figure 3.5
4. Microsoft Excel sheet used for calculating  $\rho_{eff}$ ,  $f_{Si}$ , and  $f_0$ , and  $f_H$  in the binary shell structure In Figure 3.5
5. The Casino file used for simulating the data shown in Figures 4.1A and B
6. MATLAB script for calculating the attainable SNR in Figure 4.1A
7. MATLAB script for calculating the attainable SNR in Figure 4.1B
8. ImageJ script for analyzing the PMS shrinkage in Figure 4.2 and Appendix III
9. The Casino file used for simulating the data used in Figure 5.4

## Appendix I: Determination of the electron dose

### Introduction

The electron beam causes a range of effects that need to be considered when interpreting the data obtained LPEM. In order to improve the reproducibility of the obtained data, it is, therefore, crucial to accurately report the electron dose ( $D_e$ ) is for any LPEM experiment.

The ideal instrument for direct measurement of the electron beam current ( $I_p$ ) is the Faraday cup that can be inserted in the column and is connected to an external pico amperemeter via the airlock of the goniometer. In this work, we did not have access to such a dedicated system. Instead, the  $I_p$  was measured by two in-built pico-amperometers installed in the microscope: One connected to the fluorescent screen of the microscope and the other connected to the so-called drift tube of the EEL spectrometer. [163]. Also, the CCD-detectors (cameras) of the microscope can be used for measuring the  $I_p$ . Both cameras do have a high degree of linearity also at the lower beam intensities, so they are better suited for measuring low beam currents such as used in STEM. For accurate results, it is required to know the average efficiency at which each incoming electron will create photons when hitting the scintillator material coupled to the CCD. The conversion efficiency ( $k_{\text{eff}}$ ) is dependent on the acceleration voltage and is also instrument specific. Furthermore, the conversion properties of the scintillator may change over time due to the depositing contamination and degradation.

Once the electron beam current ( $I_p$ ) is a known, calculation of the electron dose can be done by using Eq. 1.

$$D_e = \frac{I_p t}{eA} \quad (\text{Eq. 1})$$

, where  $t$  is the exposure time,  $e$  is the elementary charge, and  $A$  is the exposed time [2].

## Results and Discussion

### Determination of the $I_p$

The  $I_p$  was first measured using the smaller fluorescent screen of the microscope. The microscope was operated in TEM mode at  $U = 200$  kV by using a spot size 1C and condenser lens aperture size of  $50 \mu\text{m}$ . The electron beam was condensed so that it just fitted the small fluorescent screen with a diameter of  $r = 1.2$  cm. The current readout from the pico- amperemeter was displayed on the microscopes graphical user interface as  $198 \text{ pAcm}^{-2}$ . This was converted into absolute units by multiplying it with “Jeol small fluorescent screen factor”  $11 \text{ cm}^2$ , which was obtained from a representative (Dr. Pankau) of the camera manufacturer Gatan. Hence,

$$I_p = 198 \frac{\text{pA}}{\text{cm}^2} * 11 \text{ cm}^2 = 2.18 \text{ nA}$$

It should be noted that the “Jeol small fluorescent screen factor” does not correspond to the physical size of the screen, which is  $\pi(1.2 \text{ cm})^2 = 4.5 \text{ cm}^2$ . The reason for this is not known.

The second measurement of the  $I_p$  was done by using EELS picoamperometer and instructions obtained from the instrument manufacturer (Gatan, USA) [164]. In short, the electron beam was directed directly to the wall of the u-shaped drift tube, which is located after the entrance aperture of the spectrometer. The body of the drift tube is electrically connected to a picoamperometer, and the readout can be accessed by dedicated “Drift Tube Current.gtk”-plugging for Gatan Digital Micrograph. The current readout was manually stored from six measurements taken 10 seconds apart. The average  $I_p$  was found to be ~10 % higher than what was obtained by using the fluorescent screen above.

We decided to use the lower current value obtained via fluorescent screen as this value should be comparable with the other in-house JEOL-microscope.

### Determination of the $k_{\text{eff}}$

The conversion efficiency was determined for both cameras by the following method:

The binning from the camera settings was set 1, and the automatic background correction of images was turned off, meaning that no dark reference or gain reference image was subtracted from the pixel intensities. The beam was condensed so that it fitted the screen (Fig. I.1) and a single image was acquired using the automatic exposure time (t). Immediately after, the  $I_p$  was measured with the small fluorescent ( $I_p = 2.14$  nA) screen as described above. In the post-processing step, a circular ROI was drawn around the illuminated area in GMS and the total number of counts ( $N_{tot}$ ) was acquired with the “Sum”-function. To calculate the conversion efficiency  $k_{eff}$  for the Gatan US1000XP-camera, the following formula was used:

$$k_{eff} = \frac{e N_{tot}}{I_p t} = \frac{1.602e-19 \frac{C}{Electron} * 6.39e+10 Counts}{2.14e-9 \frac{C}{s} 0.475 s} = 9.9 \frac{counts}{electron} \quad (\text{Eq. 3})$$

The  $k_{eff}$  for Gatan Orius -camera was found to be 4.0 counts/electron.

### Measurement of the STEM probe current

The Gatan US1000XP-camera was used to measure the  $I_p$  in STEM-mode when the probe size was set to 4C, and 20  $\mu\text{m}$  condenser lens aperture was used. The electron beam was directed at the camera, and camera length was used to condense the beam so that the whole probe fitted the viewing area. An image was acquired using binning 1 and automatic exposure time. The resulting image is shown in panel B of Fig. I.1 with  $t = 5.0$  s resulting a  $N_{tot} = 2.51E +10$  counts on the circular are marked on the image. Rearranging the Eq 3. gives

$$I_p = \frac{e N_{tot}}{t k_{eff}} = 81 \text{ pA}$$

To double-check the result, we immediately measured the probe current also by using available picoamperometers. The readout from the picoamperometer attached on the

fluorescent screen was manually saved 5 times every ten seconds, resulting  $I_p = 85$  pA. When the picoamperometer of the EEL spectrometer was used, an average of  $I_p = 88.6$  was obtained. Tabulated values obtained from the microscope manufacturer indicated that the factory default for these probe and condenser settings should be 80 pA. Hence we concluded that we are able to measure the value  $I_p$  within 10 % confidence interval.

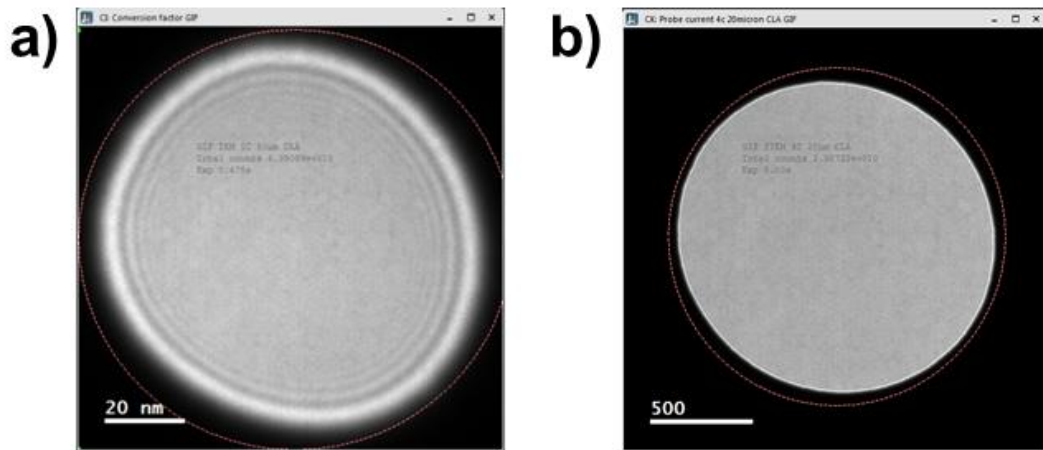


**Figure I.1 Measuring the electron beam current with CCD-camera.** A) An image of the TEM electron probe was acquired with the Gatan US1000XP-camera using exposure time ( $t$ ) of 0.475 . The number of total counts ( $N_{tot}$ ) under the indicated circle is  $6.39e+10$  counts. B) An image of the STEM probe  $t = 5$  s,  $N_{tot} = 2.52e+10$  counts.

## Conclusions

The  $I_p$  can be measured directly by using the picoamperometers of the microscope and EEL spectrometer. The estimated accuracy of the method was 10 %. Another way of measuring the beam current is by the CCD cameras once the conversion efficiency is determined.

## **Appendix II: Measuring liquid thickness by using electron energy-loss spectroscopy**

### **Introduction**

We have argued that accurate reporting of electron dose is essential for obtaining reproducible data with LPEM. Similarly, it can be argued that the liquid thickness should be reported and that it is an important dimension of metadata. In transmission mode (STEM and TEM), increasing thickness leads to loss of image resolution, and the optimal imaging modality is dependent on the liquid thickness [59]. Furthermore, the amount of deposited energy per projected area is dependent on the thickness and thus may be a factor in the appearance of beam-induced effects [61]. Finally, the liquid thickness may also play a role if reactions are studied in the liquid cell. Thin liquid layers may lead to depletion of reactants in the confined volume of the liquid cell and hence affect the kinetics or morphology of growing structures [85, 88, 165, 166]. The separation between liquid cell walls can also affect the flow resistance and thus mass-transport in the liquid cell if flow configuration is used[26]

Generally speaking, two principal methods exist for determining the sample thickness in electron microscopy: 1) Measuring the number of transmitted electrons vs. incoming electrons (exponential scattering law) and 2) Characterization of the energy distribution of transmitted electrons (EELS Log-ratio technique) [60].

In LPEM, both the exponential scattering law [21] and EELS log-ratio technique[124, 167] have been used to estimate the liquid thickness. In both cases, the measurement itself is straightforward using digital detectors, but estimating absolute thickness requires the calculation of the scattering cross-section and introduces the uncertainty [125]. Furthermore, the linear relationship between thickness and measured electron distribution breaks down in thick samples, and this may limit the applicability of the measurement [60].

Independent of how the absolute value of the thickness is calculated, it is important that the measured quantity ( $I_t/I_o$  or  $t/\lambda$ ) is reported with the collection angle of the microscope setup (Objective lens aperture or EELS entrance aperture).

## Results

### Measuring liquid thickness by using EELS

The principal method measuring for measuring the liquid thickness in this work was based on EELS, and the experimental scheme was adapted from Jungjohan et al. [124].

In short, the method can be divided into three steps:

- 1) Record the complete energy-loss spectrum of the transmitted electron beam.
- 2) Determine the relative thickness  $(t/\lambda)_{tot}$  from the data by the log-ratio method .
- 3) Estimate the value of  $\lambda$  for both water and material of windows (Here,  $Si_3N_4$ ) and the then calculating the absolute liquid thickness  $t_{H_2O}$  by assuming that

$$(t/\lambda)_{tot} = t_{Si_3N_4}/\lambda_{Si_3N_4} + t_{H_2O}/\lambda_{H_2O} \quad (\text{Eq. 1})$$

### Recording and processing the energy-loss spectra

In panel A of Fig. II.1 is shown a HAADF-STEM image of a corner of a liquid cell partly filled with water. A total of 34 spectra were acquired along the green line separated by a distance of 270 nm, using an acquisition time of 50 ms, a collection angle of 16.6 mrad and electron beam convergence angle 13.4 mrad. Two representative spectra are shown—one from the area filled by liquid (B) and others filled by gas (C).

To calculate the  $t/\lambda$  , the total relative thickness of the sample, the following equation from Malis et al. [123] was used

$$(t/\lambda)_{tot} = \ln \left( \frac{I_{tot}}{I_{ZLP}} \right) \quad (\text{Eq. 2})$$

Where  $I_{tot}$  is the total sum of the integrated intensity spectrum, and  $I_{ZLP}$  is the sum of intensities integrated over the zero-loss peak centered at 0 eV. The relative thickness profile shown in Panel D was calculated automatically by the “Log-ratio”-function of the Gatan Digital Micrograph 3.41 -software (GMS).

### Estimation of the inelastic mean-free path length for water and silicon nitride

The method is based on calculating the inelastic mean free path length defined as [123]

$$\lambda = \frac{106 F E_0}{E_M \ln \left( \frac{2 \beta E_0}{E_M} \right)} \quad (\text{Eq. 3})$$

Where,  $E_0$  is the acceleration voltage (200000 eV,) and  $\beta$  is the collection semi-angle of the spectrometer (8.3e-3 rad),  $F$  is the relativistic factor

$$F = 1 + \frac{1 + \frac{E_0}{1022}}{\left(1 + \frac{E_0}{511}\right)^2} \quad (\text{Eq. 4})$$

(and

$$E_M = (7.6 Z_{eff})^{0.36} \quad (\text{Eq. 5})$$

Where  $Z_{eff}$  is the effective atomic number of the material given by

$$Z_{eff} = \frac{\sum f_n Z_n^{1.3}}{\sum f_n Z_n^{0.3}} \quad (\text{Eq. 6})$$

Where  $f_n$  and  $Z_n$  are the atomic fraction and atomic number of the species  $n$ , respectively.

Used stoichiometric formulas for silicon nitride and water are  $\text{Si}_3\text{N}_4$  and  $\text{H}_2\text{O}$ .

Typing in the given values resulted in  $\lambda_{\text{H}_2\text{O}} = 175.4 \text{ nm}$  and  $\lambda_{\text{Si}_3\text{N}_4} = 135.9 \text{ nm}$ .

Finally, the  $t_{water}$  can be calculated by assuming  $t_{Si_3N_4} = 100$  nm rearranging the Eq. 1 to give

$$t_{H_2O} = \left( \left( \frac{t}{\lambda} \right)_{tot} - \frac{t_{Si_3N_4}}{\lambda_{Si_3N_4}} \right) * \lambda_{H_2O} \quad (\text{Eq. 7})$$

The profile for the absolute liquid thickness is shown in the Pane E of Fig. II.1

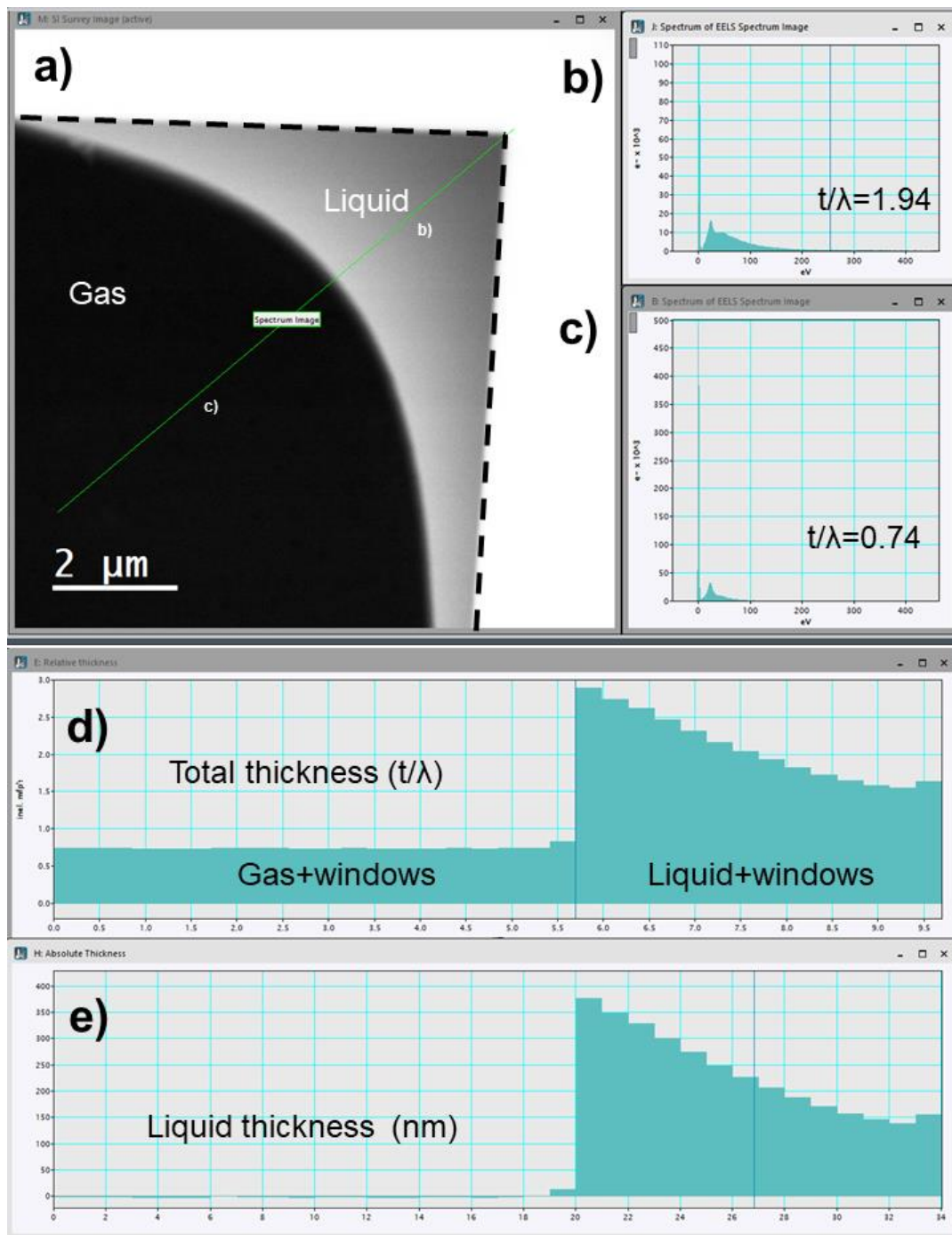


**Figure II.1 Determining the liquid thickness by using Electron energy-loss spectroscopy (EELS) and Log-ratio-method in Gatan Digital Micrograph software.** A) An overview HAADF-STEM image (20 kx) of a partly filled liquid cell. A meniscus separates the gas and liquid-filled parts of the liquid cell. Dashed lines indicate the edge of the window. The green diagonal line indicates the location of the line scan along which the spectrum image (not shown) was acquired. B) and C) shows EEL spectra and calculated  $t/\lambda$  values for locations indicated in panel A) (liquid and gas, respectively). D) Shows the calculated total relative sample thickness ( $t/\lambda$ ) tot along the line scan. E) Shows the calculated absolute liquid thickness (nm) after subtracting the

contribution of 100 nm of SiNx ( $0.74 t/\lambda$ ) and multiplication by the calculated value of  $\lambda_{water}=175$  nm.

### **Applicability and error related to $\lambda$**

It has been reported that EELS-log ratio technique can be used to measure sample thicknesses up to  $5 \lambda$  corresponding to  $t_{water}$  of 750 nm when two 50 nm Si<sub>3</sub>N<sub>4</sub> are used. (Eq. 7). The method is expected to give results with an acceptable error level of 15% [123, 124], which is due to the uncertainties related to calculating the  $\lambda$ . In a recent study, the inelastic mean free pathlength of liquid water was measured by using electron holography in a liquid cell for 120 kV and 300 kV acceleration voltage and was found to be nearly 40 % higher [125] than what was predicted by the model used in this work. Thus there is not a complete agreement on the error margin of this method in liquid.

### **Determination of the experimental measurement error**

In order to determine the total level of confidence of the used liquid thickness measurement via EELS log-ratio method we determined the measurement error of  $t/\lambda$  as a function of  $t$ . This was achieved by recording three spectrum images of size of 20×20 pixels at the same location but changing the inner pressure of liquid cell to 1.0, 0.5, and 0.05 bar. As the sample location was chosen to be close to the silicon edge, there was also a thickness gradient present along the vertical axis of spectrum images. As the images were acquired against the thickness gradient, each row containing 20 pixels was estimated to have liquid thickness. Therefore, the standard deviation (SD) present in each row should be mainly due to the measurement itself. The combination of the window bulging and pressure controller resulted in a range of liquid thickness between 230-720 nm. The thickness for each pixel using EELS log-ratio method was calculated, and the SD for each row (N=20) was determined. In all liquid thicknesses, the relative SD was found to be < 5%. (Fig. II.2 A) The relative SD of the measurement increased towards larger liquid thicknesses, which is expected due to the increased multiple scattering. It was also

observed that the relative SD increased towards the edge of the window, which could be due to the edge of one window being not fully aligned with the edge of the other one.

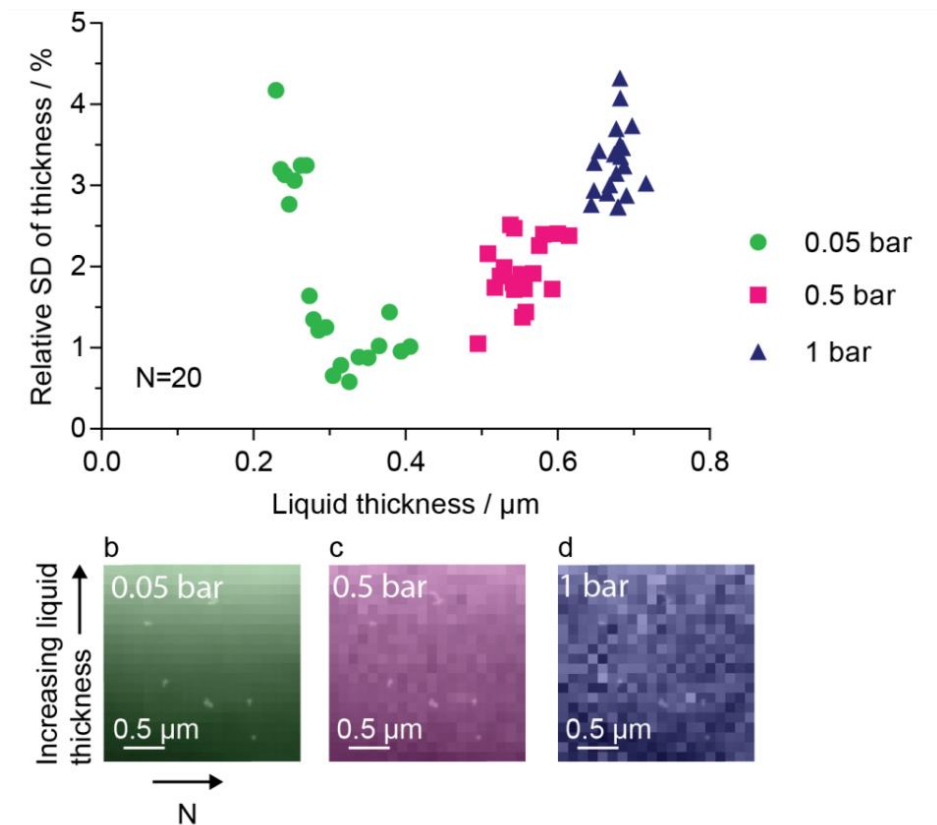


**Figure II.2 Determining the measurement error for EELS Log-ratio method in liquid thickness measurement using the pressure controller setup [5].** A) The experimental standard deviation (SD) of the measurements plotted as a function of the measured liquid thickness. Each data point represents the SD of 20×EEL spectra acquired on the same row in the thickness map shown in B)-D). EELS thickness maps of a region near the window edge using internal pressures of 0.05 B), 0.5 C), and 1.0 bar D).

## Conclusions

EELS can be used to measure the absolute liquid thickness in applications of LPEM. When using 50 nm thick windows, liquid thicknesses up to 750 nm can be measured. The total

relative error of the method was estimated to be 20% in liquid thicknesses between 230 - 720 nm. However, the error might be as high as 50 %, as was proposed in [125].

## **Appendix III: Image analysis script to measure the shrinking of PMS**

### **Introduction**

This appendix describes in detail how the low-SNR images of PMS were analyzed. The steps of the method are described below, including a graphical schematics. The script is available in the Supplementary information

### **Results and Discussion**

The goal of this image processing task was to segment PMS particles in the field of view and report their average radius. Due to the low SNR of PMS in liquid, the direct segmentation sequence in Step 1 registered random background fluctuation as objects. To circumvent the problem, the analysis was focused on features of which location remained constant within at least  $2/3$  (or 66%) during the sequence; Hence, these segmented features were characterized as having “temporal persistence. In order to first quantify the temporal persistence used for the selection of the features of interest, All objects in the image sequence were segmented then the whole stack was averaged. This effectively transformed the temporal persistence into  $n$  levels of gray (Step 2), where  $0 \geq n \leq$  number of frames in the sequence. After this, we binarized the image by setting the threshold value to 66% resulting in a binary image, including only features fulfilling the above-stated criteria for temporal persistence. We performed a further analysis in the area around these persistent features by centering a 200 \*200 nm rectangular regions of interest (ROI) in the center of every feature. In Step 4. features within each of these ROIs were analyzed as individual images so that only features fully fitting the square were included. (Step 4) This approach effectively removed false positives from the analysis and made it easy to visualize the success of the image processing pipeline for a given dataset. (Step 6.) After analyzing the rectangular regions of interest, the script listed segmented features with total areas and their center-of mass-coordinates. The latter is defined in the ImageJ documentation as the brightness-weighted average of x- and y-coordinates within the object [168]. The obtained list contained some duplicates with identical area and location,

and these were removed manually using Microsoft Excel-software. Next, the data was imported to the Prism v. 7.03 (GraphPad, San Diego, US ) to statistically evaluate the size distribution of PMS as a function of the  $D_e$ . In brief, we used the one-way analysis of variances (ANOVA) to show that there is a statistically significant decrease in the average diameter in subsequent frames of the dataset.

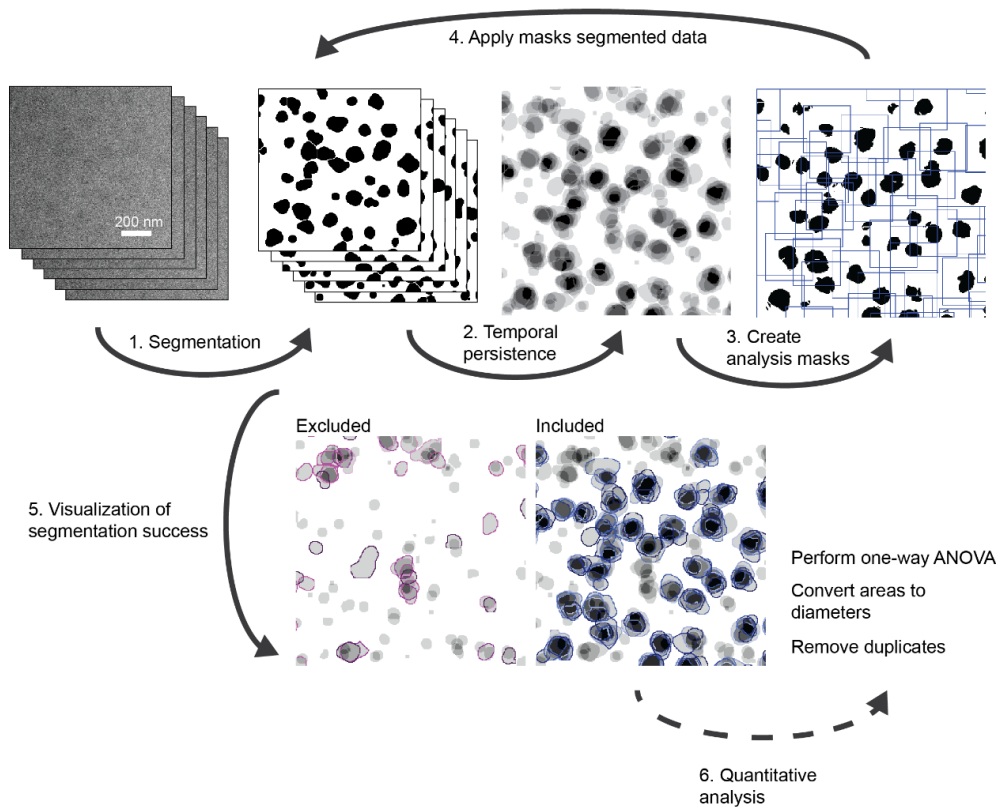


**Figure III.1 . The image processing pipeline used to analyze the size distribution of hydrated polystyrene microspheres (PMS) in a sequence of images.** In steps 1-3, separate regions of interest were defined that were quantitatively analyzed in steps 4-6. In 5, the visualization of segmentation success shows objects that were excluded (pink) and included (blue) to the quantitative analysis done in Prism-software.

The following steps were applied to analyze an image series:

### **Step 1. Processing and segmentation**

- Conversion to an *8-bit* image
- $2 \times$  *Bandpass filtering* of structures larger than 100 pixels and smaller than 4 pixels
- Binarization of the image by *Auto thresholding* using the Li-method [169]
- *Open*- a procedure to remove small specks: 8 Iterations, 3 Counts
- *Dilate*- a procedure to restore the average size of PMS to 110 nm in the first frame of the sequence: 2 Iterations, 1 Count.
- *Watershed*-operation to separate connected particles.

### **Step 2. Temporal Persistence of features**

- All the binarized images in the stack are averaged by intensity.
- Average image *threshold* is set to 66% (2/3)
- Temporally persistent features were selected by the *Analyze particles*-tool. Only features  $> 250 \text{ nm}^2$  were included.

### **Step 3. Creation of masks**

- $200 \times 200 \text{ nm}$  rectangular ROIs are created and centered at the center-of-mass of each temporally persistent feature.

### **Step 4. Application of mask to the segmented data**

- For each mask, *Analyze particles*, including only features that are not touching the edges and have size  $> 250 \text{ nm}^2$  and circularity 0.5-1.0.

### **Step 5. Visualization of segmentation success**

- Included and excluded features are drawn to help the evaluation of segmentation success.

### **Step 6. Quantitative analysis of size distributions**

- Data including Center-of-masses and areas are exported to Microsoft Excel, where duplicates are removed and areas  $A$  are transformed to diameters  $d$  using the formula:

$$d = 2 \sqrt{\frac{A}{\pi}}$$

- Data is exported to Prism GraphPad software where the one-way ANOVA is applied to determine the statistically significant changes in the size distribution.